Journal of Unconventional Oil and Gas Resources 12 (2015) 87–122

Contents lists available at ScienceDirect

Journal of Unconventional Oil and Gas Resources

journal homepage: www.elsevier.com/locate/juogr

Review

Gas transport and storage capacity in shale gas reservoirs – A review. Part A: Transport processes

Yves Gensterblum [a,*], Amin Ghanizadeh [b], Robert J. Cuss [c], Alexandra Amann-Hildenbrand [d], Bernhard M. Krooss [d], Christopher R. Clarkson [b], John F. Harrington [c], Mark D. Zoback [a]

[a] Department of Geophysics, Stanford University, 397 Panama Mall, Stanford, CA 94305-2215, USA
[b] Department of Geoscience, University of Calgary, Calgary, Canada
[c] Transport Properties Research Laboratory, British Geological Survey, Keyworth, Nottingham NG12 5GG, UK
[d] Institute of Geology and Geochemistry of Petroleum and Coal, RWTH Aachen University, Lochnerstrasse 4-20, 52056 Aachen, Germany

ARTICLE INFO

Article history:
Received 2 December 2014
Revised 31 July 2015
Accepted 3 August 2015
Available online 13 September 2015

Keywords:
Shale gas
Transport in unconventional reservoirs
Slip flow
Pore elasticity
Effective stress law
Permeability

ABSTRACT

For decades, scientists and engineers have been investigating and describing storage and transport mechanisms in geological porous media such as reservoir rocks. This effort has resulted in the development of concepts such as single-phase and multi-phase flow, which describe the storage and transport of fluids in conventional reservoir rock types such as sandstones and carbonates. However, many of these concepts are not directly applicable to unconventional reservoirs. For example, shale gas reservoirs consist of organic-rich lithotypes, which have high compressibility, very small pore throats, low porosities and extremely low and anisotropic permeabilities, and relatively low gas storage capacities. The models developed to describe conventional reservoirs do not accurately describe the hydrocarbon transport processes involved in these rocks.

In this part A of the review paper, we aim to provide a concise and complete review on characterizing the fluid transport processes in unconventional reservoirs. We will examine processes occurring at various spatial scales, ranging from fracture flow on the centimeter scale down to slip-flow on the nanometer scale. Due to the softer nature of tight shales, many processes, such as slip-flow and the pore-throat compressibility, will have to be considered as coupled. We also develop a detailed description of the coupling between slip-flow, which is a fluid dynamic effect, and the pore-throat compressibility, which is a poroelastic effect, in unconventional reservoirs, and interpret experimental observations in light of this description.

Furthermore, we discuss in detail how these transport properties depend on organic content, clay content and type, amount of pre-adsorbed water and pore compressibility.

Contents

* Corresponding author.

http://dx.doi.org/10.1016/j.juogr.2015.08.001
2213-3976/

Nomenclature

Terms and symbols	Definition (unit)
A	cross-sectional area of the sample fracture (m^2)
βC	volume concentration (mol m^{-3})
c	constant dimensionless
γ	effective stress coefficient for friction law dimensionless
D	diffusion coefficient (m^2 s^{-1})
ρ_{eff}	effective stress (Pa)
ρ_n	normal stress on a fault or fracture (Pa)
J	diffusive flux (mol m^2 s^{-1})
Apparent gas permeability coefficient, k_{gas}	Gas permeability coefficient from single-phase gas flow tests corresponding to a given mean pore pressure – value is not corrected for the Klinkenberg effect. Darcy, m^2 1 Darcy = 9.87×10^{-13} m^2
L	length of sample (m)
λ	mean free path length (m)
μ	coefficient of friction (−)
μ_{kin}	gas/water kinematic viscosity (Pa s)
$P_{up,down}$	upstream/downstream pressure (Pa)
$P_{conf.}$	confining pressure (Pa)
P_m	Mean pore pressure (Pa)
P_e	Effective pressure (Pa)
ϕ	Porosity (−)
Q	volumetric gas flow rate (m^3)
$\sigma_{1,2,3}$	stress in direction 1,2,3 or h = horizontal, minimum stress orientation or H = horizontal, maximum stress orientation
$V_{1,2}$	upstream/downstream volumes (m^3)
τ	shear stress (Pa)
χ	effective stress coefficient ('Biot coefficient' when the effective stress law is applied to bulk volume changes) (−)
Z	compressibility factor of gas dimensionless
k_n	Knudsen number dimensionless

Introduction

Many geoengineering efforts such as mining, tunneling, waste water disposal, nuclear waste disposal, carbon dioxide sequestration, hydraulic fracturing and conventional as well as unconventional reservoir exploitation are affected by the hydraulic and mechanical properties of rocks. A strong understanding of these properties is critical to the effective pursuit of these activities. In this paper we focus on the relationship between the material properties of shales and the flow of hydrocarbons in unconventional reservoirs.

Content overview

A short historical background of the unconventional oil/gas industry in North America is provided at the beginning of the review, followed by the socioeconomic aspects such as induced seismicity during the exploitation of unconventional reservoirs like coalbeds, tight sandstones and organic-rich shales. Organic-rich shales are heterogeneous geological systems with variations in composition and fabric occurring on a wide range of scales (chapter "Pore network attributes of organic-rich shales"). The micro-structure of organic-rich shales can differ significantly between different shale layers and causes significant anisotropy in rock properties (chapter "Matrix permeability"). The matrix permeability of organic-rich shales and its relationship with lithological factors including maturity, TOC (total organic carbon) content, porosity, pore size distribution and mineralogy is discussed in this review briefly, and is covered in detail in a second review paper (Ghanizadeh et al., 2015, in preparation). Although it is estimated that shale gas plays have significant gas-in-place (GIP) (In part B of the review "Gas storage capacity"), economically exploring and producing from these complex, heterogeneous reservoirs requires a strong understanding of the fluid transport processes operating within them. It is technically difficult to achieve economic production rates in these reservoirs (chapter "Fracture flow"), which commonly have matrix permeability coefficients down to the nDarcy-range (chapter "Matrix Permeability"). This difficulty is partially due to our poor understanding of the fluid transport processes within the fracture and matrix systems (chapter "Matrix permeability") prevalent in these lithotypes. Furthermore, fracture and matrix transport show a significant sensitivity to effective stress variations (chapter "stress sensitivity") during reservoir depletion. In the chapters related to transport process the relevant transport processes and their time/length scales will be discussed.

A brief history of unconventional oil/gas industry

The recent development of unconventional reservoirs such as coalbed methane, tight gas, and shale oil/gas has revolutionized the oil and gas industry. Although the focus on these types of reservoirs have increased in recent years, they have a long history in the oil/gas industry.

The first commercial natural gas well producing from a shale reservoir rock was an 8 m deep well drilled in 1825 in Fredonia, New York. Williams Aaron Hart, the tinsmith who drilled the well, piped gas to the nearby village, metering and selling it to local businesses for lighting, according to newspaper accounts of the day (Lash, 2013). For chronological comparison, Edwin Drake drilled his first oil-well more than 30 years later.

Natural gas for local consumption, including that from shallow fractured shales in the Appalachian and Illinois basins, has been produced on a broader scale since the 1860's. Large-scale production began with the Big Sandy gas field, which was developed in the fractured Devonian shales of Floyd County, Kentucky starting in 1915 (Nuttall, 2003).

A series of technological breakthroughs allowed unconventional gas to become more widespread as the 20th century progressed. The development of large diameter pipelines allowed for the transport of large volumes of gas from the oil and gas fields of the mid-continent and the southeast to the northeastern cities. Hydraulic fracturing, first performed in 1947 on a gas well operated by Pan American Petroleum Corporation in Grant County, Kansas, allowed for increased production of shale gas. Finally, the development of downhole motors, a key component of directional drilling technology, progressed rapidly in the early 1970s.

Today, the US and Canada have the lowest gas prices in the world (Birol, 2012; Economides et al., 2012). These countries no longer need to import gas, and are looking for opportunities to increase their export capacities. Although the economic importance of low energy prices has long been discovered, the overall socioeconomic consequences of the recent gas boom are still poorly understood.

Social, economic, and environmental context

Unconventional gases, including shale gas, offer attractive low-carbon solutions for the transition period to a future power by renewable energy. The ability of industrial instruments to make the transition efficient, effective and economical is however still a question of debate (Benson, 2014; Bloomberg and Krupp, 2014; Kerr, 2010; Kinnaman, 2011; McElroy and Lu, 2013). During the transition, global reduction in carbon dioxide (CO_2) emissions must be pursued. The recent reduction in mercury, SO_2, CO_2, NO_x and particulate matter emissions in North America was caused largely by the recent and ongoing shift from coal and oil to natural gas (eia, 2013). However, similar to other natural resources, exploitation of natural gas cannot be done without taking into account risks and environmental concerns such as induced seismicity, contamination of groundwater by additives, and high water consumption (Howarth et al., 2011). Many of these issues are likely to have technical solutions, including the use of liquid CO_2 as a fracturing fluid. A pilot test of the use of CO_2 as a fracturing fluid in the early nineties showed encouraging results, including an improvement in the production rate, reducing the likelihood of formation damage, and more effective cleanup (Mazza, 2001; Yost et al., 1993). Theoretically, this method should also enhance the recovery factor and drainage area, prevent capillary trapping, and allow for better shale matrix drainage efficiency and gas release kinetics (Wang et al., 2012). Additional benefits include a reduction in flowback water and reinjected water (the latter of which probably results in a reduced likelihood of induced seismicity), and a reduction in the needed amount of chemical additives. Disadvantages include potential CO_2 shortages, high costs, the possibility of trace metal mobilization, higher well head pressure, and lower proppant transport capacity (Gensterblum and Zoback, 2014). Despite its many advantages, the use of CO_2 as a fracturing fluid is not a common practice, mostly due to the high costs of obtaining and transporting CO_2 (Gensterblum and Zoback, 2014).

Induced and triggered seismicity

A major public concern related to the development of unconventional reservoirs is the likelihood of triggered and induced seismicity. In the recent years, the frequency of earthquakes in areas that have historically considered largely inactive has increased significantly. An earthquake swarm in Oklahoma in November 2011, which had a maximum magnitude of 5.6 Richter, was unexpected and has received a great deal of public attention.

In general it is very difficult to identify the ultimate cause of an induced earthquake – typically there is no direct chronological relationship between the occurrences of an earthquake and surface

or reservoir activities. Earthquakes releases stored elastic strain energy when a fault starts to slip. A fault will remain locked as long as the applied shear stress τ is less than the strength of the contact (King Hubbert and Rubey, 1959).

$$\tau = \mu \cdot \sigma_{\text{eff}} \tag{1}$$

The failure condition required to initiate rupture is usually expressed in terms of the effective stress, where the critical shear stress τ_{crit} equals the product of the coefficient of friction μ and the effective stress.

$$\tau_{\text{crit}} \begin{cases} < \mu(\sigma_n - \gamma P_{\text{pore}}) + \tau_0 \rightarrow \varepsilon > 0 \\ \geq \mu(\sigma_n - \gamma P_{\text{pore}}) + \tau_0 \rightarrow \varepsilon = 0 \end{cases} \tag{2}$$

The effective stress is defined by the difference between the applied normal stress σ_n and the pore pressure P_{pore} multiplied with the effective stress coefficient γ. Increasing the shear stress by elevating the pore pressure can bring the fault to failure, triggering an earthquake (King Hubbert and Rubey, 1959).

We are considering only two possible causes of this type of induced seismicity – hydraulic fracturing operations and disposal of the associated wastewater (Ellsworth, 2013; Walsh and Zoback, 2015). In both cases, the injection of pressurized fluids cause changes to in-situ stress conditions. However, the duration of this stress change is different. In contrast to hydraulic fracturing, where injection takes place over a period of hours to, at most, a few days, waste water disposal takes place over a period of months to years at any given injection site. As a result, waste water disposal wells are able to change the stress regime and the friction properties to a greater degree. Walsh and Zoback (2015) argue that the Oklahoma earthquakes are related to waste water disposal, which has triggered a critical stressed fault system.

Comparison of conventional and unconventional reservoirs

For the past 80 years scientists have investigated the fluid transport properties of a wide range of porous rocks, including sandstones and carbonates, which make up the reservoir rocks in most conventional reservoirs. The main purpose was to describe and understand the migration of hydrocarbons from source rocks to reservoir rocks (at this time, shales were considered to be only hydrocarbon source rocks or caprocks). Later, questions about caprock integrity led to the first studies on fluid migration in shales. Many recent studies of fluid transport in shales have been conducted to better understand how caprock integrity might affect carbon storage efficiency.

Many concepts applied to reservoirs today are developed considering only sandstones or carbonates as reservoir rocks. For unconventional reservoirs the petroleum source rock often is a part of the reservoir. In order to further develop our understanding of fluid transport in shales, it is useful to compare the properties of conventional and unconventional reservoir rocks (Table 1) – this allows us to better understand which existing concepts are adequate and which will need to be modified. The biggest difference between a conventional reservoir rock and a shale is that the magnitude of certain properties is much smaller in a shale. These properties include permeability, porosity, and micro to meso pore size distribution. Given the fine-grained nature of the shale matrix, low values for these attributes might be expected. What might be less obvious is that mechanical properties such as compressive strength, tensile strength, and the elastic modulus (Table 1) are also much lower in shales than in sandstones or carbonates. The unique material properties of shales result in much more pronounced coupling of mechanisms, which results in fluid dynamic and poro-elasticity effects which are not detectable at carbonate or sandstone reservoirs. Some of the physical concepts that explain the experimental observations of such coupled processes are listed in Table 2.

Background

Pore network attributes of organic-rich shales

Porosity–permeability relationship

Researchers have investigated the correlation between porosity and permeability for many decades. Archie (1950) established a first "poro-perm" relationship for sandstones. Since pores are the primary mechanism by which fluids enter a permeable rock, the existence of a porosity/permeability relationship is not surprising. The relationship breaks down when porosity decreases below a certain point – a small amount of pore volume might be distributed throughout the shale matrix without many of the pore networks overlapping. This would result in a shale, which is not permeable but contains porosity. We can conclude that in fine-grained rocks like shales a certain minimum porosity is required to create connectivity and consequently permeability. Furthermore, shales are more anisotropic and heterogeneous than sandstones. Heterogeneities in these geological systems comprise variations in composition and fabric on different scales (Chalmers et al., 2012b; Clarkson et al.,

Table 1
Comparison of reservoir properties between conventional and unconventional reservoir rocks.

Property	Conventional (sandstones/carbonates)	Unconventional (considering only shales with TOC up to 20%, clay up to 70%)	Sources
Porosity	10–40%	0.1–20%	
Permeability (unfractured)	10^{-13} m^2 up to 10^{-11} m^2	10^{-23} m^2 up to 10^{-19} m^2	(Tables 6,7 and 9)
Sorption capacity (mol of CH_4/kg of rock)	Negligible $\ll$ 0.01	0.01–0.4	Gasparik et al. (2013, 2014)
Compressive strength (MPa)[a]	650	200–300	Jizba (1991)
Shear strength (MPa)[b]	85	60	Jizba (1991)
Static bulk modulus (GPa)[c]	30	15	Jizba (1991)
Poison ratio[d]	Carbonates: ~0.3 sandstones: ~0.2	>0.3	
Effective stress coefficient χ	1.00 Pottsville Sandstone, Bernabe (1987): 2.2; Berea Sandstone with clay content: up to 4, Zoback and Byerlee (1975b)	0.15–0.8 0.99	Heller et al. (2014) Kwon et al. (2001)

[a] Compressive strength is a function of clay content and depends strongly on the confining pressure (Jizba, 1991). These values were determined at a constant confining pressure of 50 MPa.
[b] Shear strength is a function of clay content and porosity. Furthermore, shear strength depends strongly on the confining pressure (Jizba, 1991). These values were determined at a constant confining pressure of 50 MPa.
[c] The dynamic and static bulk modulus values show an agreement within ±5% for conventional reservoirs, whereas for shales the dynamic bulk modulus are usually approximately 25% higher (Jizba, 1991).
[d] Single values are valid simplification, however in general the poison ratio depend on several rock properties such as porosity and water saturation.

Table 2
Summary of major contributions to the mathematical and physical descriptions of flow in micro-porous media.

Model	Description
Klinkenberg (1941)	The empirical slip flow concept
Jamialahmadi and Javadpour (2000)	Artificial neural network used identify relationships between permeability, porosity, and depth
Rutqvist and Stephansson (2003)	A review of hydromechanical concepts and couplings in fractured rock
Javadpour (2009)	Model developed based on slip-flow, represented by Maxwell theory. Accounts for Knudsen diffusion. Modeled only for straight capillary tubes
Civan (2010)	Model developed based on slip-flow, represented by simplified second-order slip model. Contains several empirical parameters
Civan et al. (2011)	Model based on a Hagen–Poiseuille-type equation; can represent the various essential flow mechanisms in a single equation by varying the value of the Knudson number. These mechanisms include continuum, slip, transition, and free molecular flow
Darabi et al. (2012)	Model based on slip-flow, represented by Maxwell theory. Accounts for surface roughness and Knudsen diffusion in a porous medium
Azom and Javad-pour (2012)	Derived from the Javadpour (2009) model. Accounts for the flow of real gases in porous media
Singh et al. (2014)	Model developed using Navier–Stokes equation and kinetic theory (no slip-flow assumption). Accounts for Knudsen diffusion in a porous medium

2012b; Ghanizadeh et al., 2013, 2014a,b; Handwerger et al., 2011; Kim and Lee, 2012; Luffel et al., 1993; Soeder, 1988). Due to the heterogeneous and anisotropic distribution of porosity in shales, permeability can be very anisotropic. The composition and microstructure characteristics of organic-rich shales can differ significantly between different shale plays and even within the same shale play (Curtis et al., 2012). Due to the high degree of heterogeneity no unique porosity–permeability relationship exists for shales. This is because shales are highly heterogeneous in their porosity and level of tortuosity (Fig. 1). The high permeability anisotropy of shales also suggests that connectivity between pores depends on pore orientation (Houben et al., 2013). These two facts explain why a fundamental correlation between porosity and permeability for shales is, in general, not attainable.

Nevertheless, a few empirical correlations have been published, which have been observed for geological samples taken from particular basins (e.g. Wang and Reed, 2009). For a more detailed discussion, we recommend the data review and discussion by Neuzil (1994) and Spinelli et al. (2004). Yang and Aplin (2010) construct a permeability–porosity relationship based mainly on measurements of marine mudstones. They show that the permeability–porosity relationship is often a function of clay content. In shales with very high clay contents, the interlayer cation also begins to affect the correlation (Mishra et al., 2005).

For the selected data sets shown in Fig. 1, a weak power law correlation between porosity ϕ and permeability k can be derived:

$$k(\phi) = 1.64 \times 10^{-08}\ \phi^{4.1} \tag{3}$$

As discussed above this correlation intends to show only a generally increasing trend and has strong limitation in terms of applicability.

Porosity, pore size distribution and permeability

As early as 1950, Archie argued that the porosity–permeability correlation could be improved by taking the pore size distribution into account (Archie, 1950). This is because a micro-pore network and a macro-pore will have different permeabilities given a constant porosity.

A capillary bundle model is the simplest way to establish a correlation between porosity, permeability and pore throat radius

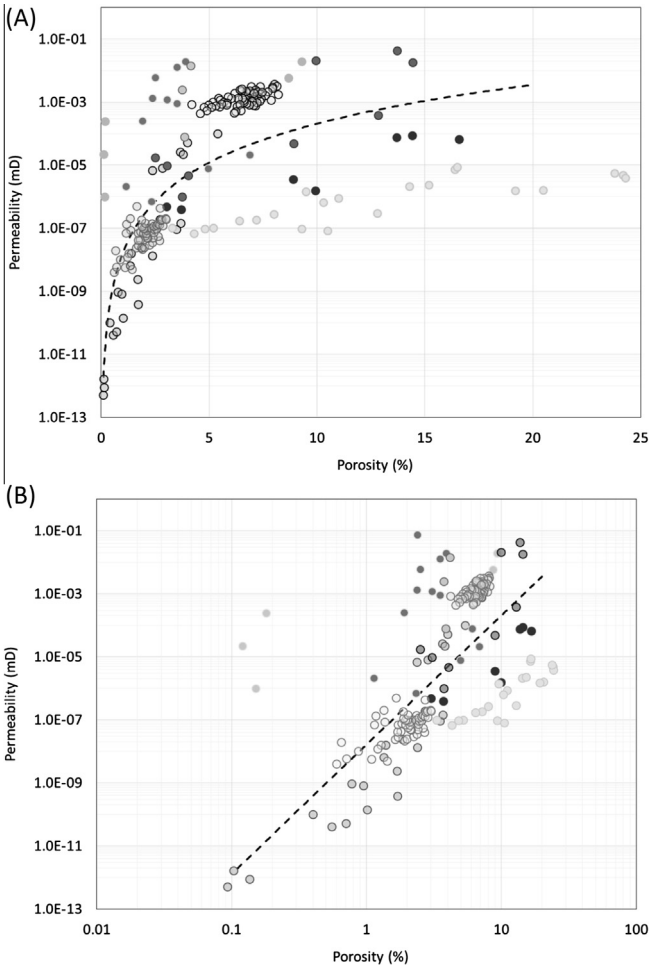

Fig. 1. Permeability as a function of porosity (Chalmers et al., 2012b; Clarkson et al., 2012b; Ghanizadeh et al., 2013, 2014a,b; Handwerger et al., 2011; Kim and Lee, 2012; Luffel et al., 1993; Soeder, 1988). In general, only a very weak correlation can be observed for fine-grained and layered sediments such as shales. Slightly stronger correlations have been reported for claystones and mudstones (Yang and Aplin, 1998, 2010).

(Fig. 2A). By combining it with the Hagen–Poiseuille law, we can establish a correlation between the Klinkenberg, or slip flow corrected, permeability and the pore size distribution:

$$k_{\infty}(d) = \frac{nd^4}{32D^2} \tag{4}$$

where n is the number of pore throats with a diameter d, and D represents the diameter of an experimental specimen.

Aguilera (2002) has proposed an empirical correlation based on mercury intrusion data and resistivity data. Permeability and porosity values were compared against the relationship for r_{p35} (pore-throat aperture [in μm] at 35% Hg saturation during a mercury injection test) using the equation proposed by Aguilera (2002):

$$r_{p35} = A\left[\frac{k}{100\emptyset}\right]^{B} = 2.665\left[\frac{k}{100\emptyset}\right]^{0.45} \tag{5}$$

where k represents the permeability of the rock (in millidarcy, mD) and ϕ is the decimal porosity. It is important to note that this approach is semi-empirical and should be interpreted and applied only where appropriate.

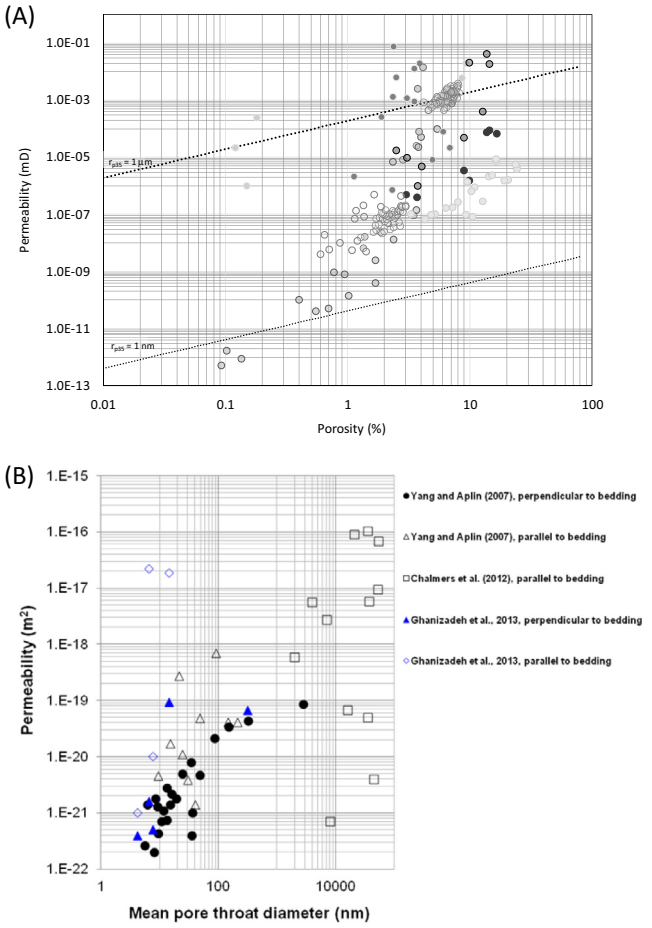

Fig. 2. Permeability as a function of porosity and mean pore throat diameter shown on a log–log plot (data taken from Chalmers et al., 2012b; Ghanizadeh et al., 2013; Handwerger et al., 2011; Kim and Lee, 2012; Luffel et al., 1993; Soeder, 1988). The dotted lines indicate pore throat radii estimated using the approach of Aguilera (2002).

Fig. 2B shows the effect of mean pore throat diameter on permeability of organic-lean and organic-rich shales measured perpendicular and parallel to bedding. For organic-lean shales (Yang and Aplin, 2007) the permeability coefficients were measured using water while for organic-rich shales the permeability coefficients were measured using methane (Chalmers et al., 2012a,b) or helium (Ghanizadeh et al., 2013). The mean pore throat diameters were calculated incrementally from the cumulative Hg-intrusion curve. As Fig. 2B indicates there is a fair to modest log-linear relationship between mean pore throat diameter and permeability coefficients measured perpendicular to bedding. There is, however, no simple straightforward relationship between mean pore throat diameter and permeability coefficients measured parallel to bedding.

Transport processes

The most efficient fluid transport mechanism in the matrix system of sedimentary rocks is pressure-driven volumetric flow (Darcy law) through interconnected pores. The pore system of sedimentary rocks, however, is not static – it is subject to substantial changes during burial and compaction. Apart from compaction-related porosity and permeability reduction, diagenetic alterations of the pore system and the resulting effects on permeability, pore pressure, poro-elasticity and storage capacity are major factors in unconventional reservoirs. The effects of digenetic alterations related to the geological history of unconventional reservoirs are outside the scope of this review paper. Instead, we will focus on interactions among the present day transport properties of shale rocks.

This transport discussion begins by discussing high-flux fluid movement (bulk reservoir, fracture flow), and proceeds to processes that occur at intermediate (Darcy, slip flow) and low to very low flow rates (fluxes) (diffusion). For topics that we cannot cover in detail, we will make recommendations for further reading.

Organic-rich shales have historically been thought of almost exclusively as either source rocks or cap rocks. As a result, most studies of fluid transport processes in shales have focused on aspects of the processes relevant to these roles (Hildenbrand et al., 2002, 2004; Krooss, 1986, 1987, 1988, 1992; Krooss et al., 1986, 1988, 1991; Krooss and Schaefer, 1987; Krooss and Leythaeuser, 1988, 1997; Schowalter, 1979; Wollenweber et al., 2010).

Fig. 3 illustrates transport processes in shales on a wide range of spatial scales. These processes occur in a variety of conduits including the pre-existing fault (secondary) network, the micro-fracture network (within the shale matrix) and finally, at the nanometer scale, meso- and micro-porosity.

Increasing exploration activities for unconventional gas reservoirs during recent years have revealed significant disparities between classical predictions of fluid flow and observations in the reservoir and the laboratory. This disparity has stimulated fundamental research into the transport properties of low-permeability lithotypes, including tight sandstones, shales and coals.

In contrast to conventional reservoirs, unconventional reservoirs often do not behave according to classical predictions. Common differences in unconventional reservoirs include the following:

- Unexpectedly long tail-off of gas production curves in shale gas reservoirs (e.g. Clarkson, 2013a; Valko and Lee, 2010).
- Very low recovery factors (<30%) (e.g. Crafton and Noe, 2013).
- Low flowback recoveries during hydraulic fracturing (30–50%) (e.g. Parmar et al., 2012).
- Micro- and meso-pore throat distribution (e.g. Clarkson et al., 2012a; Wang and Reed, 2009).
- Low to extremely low intrinsic matrix permeability (e.g. Ghanizadeh et al., 2013; Heller et al., 2014).
- Non-negligible slip flow effects occurring at low gas pressures (e.g. Ghanizadeh et al., 2013; Heller et al., 2014).
- High capillary entry and displacement pressures for the shale matrix (e.g. Hildenbrand et al., 2002).
- Different types of fracture surfaces, resulting in different gas and multiphase transport properties (e.g. Bennion and Bachu, 2006; Kim et al., 2011).

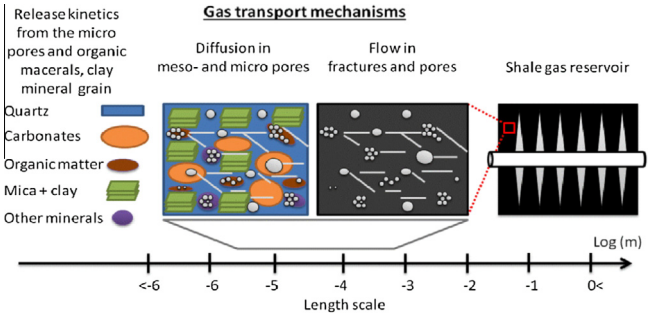

Fig. 3. Illustration of the length scales that need to be considered when describing transport processes in shales.

- Non-adherence to conventional multiphase-flow and relative permeability predictions, caused by extremely small and virtually undetectable gas saturations and saturation changes during and after imbibition (Clarkson et al., 2012b).
- Interactions among gas uptake and release rates (desorption kinetics), solution/exsolution, and transport processes.
- Increased importance of molecular diffusion (in pore fluids, organic matter and along mineral surfaces) relative to pressure-driven volume flow (Darcy flow).
- Deviations in the thermodynamics of phase behavior of alkanes in microporous organic pore network.

Overview – flow mechanisms

To accurately predict the movement of gas through shale (Askarieh et al., 2000; Ekeroth et al., 2006), it is first necessary to define the correct conceptual model that best represents the empirical data. In clay-rich rocks four primary phenomenological models can be defined to describe gas flow as proposed by Marschall (2005) (Fig. 4):

(i) Gas movement by solution and/or diffusion governed by Henry's and Fick's Laws respectively within interstitial fluids along prevailing hydraulic gradients.
(ii) Gas flow in the original porosity of the fabric governed by a generalized form of Darcy's Law, commonly referred to visco-capillary (or 2-phase) flow.
(iii) Gas flow along localized dilatant pathways (micro-fissuring), which may or may not interact with the continuum stress field, the permeability of which is dependent on an interplay between local gas pressure and the effective stress state; and,
(iv) Gas flow along macro-fractures similar in form to those observed in hydrofracture activities during reservoir stimulation, where fracture initiation occurs when the gas pressure exceeds the sum of the minor principle stress and tensile strength.

In unconventional hydrocarbon reservoirs diffusion/solution (i) is a process that will occur, but will be a slow back-ground process. Fluid flow through hydraulic fractures (iv) will be the dominant flow mechanism initially. Extraction of hydrocarbons will require additional flow along tight fractures and through the bulk matrix of the shale. This will occur through advection in the form of mechanisms (ii) or (iii). There is now a growing body of evidence (Angeli et al., 2009; Harrington et al., 2009; Harrington and Horseman, 1999; Harrington et al., 2012; Horseman et al., 1997) that in the case of visco-plastic clays and in particular bentonite, classic concepts of porous medium two-phase flow (ii) are inappropriate. Flow through dilatant pathways (iii) has been shown in a number of argillaceous materials (Angeli et al., 2009; Autio et al., 2006; Boulin et al., 2013; Galle and Tanai, 1998; Harrington and Horseman, 1999; Horseman et al., 1999; Ortiz et al., 2002). The pathways are pressure-induced, probably creep controlled and their aperture is a function of their internal gas pressure and structural constraints within the clay. However, the exact mechanisms controlling gas entry, flow and pathway sealing in clay-rich media are not fully understood and the "memory" of such pathways could impair barrier performance.

Single-phase flow system

Laminar viscous flow of one or more phases within the pore system of a rock can be described by Darcy's law. For an incompressible fluid, the flux Q ($m\,s^{-1}$) can be linearly related to the pressure gradient across the rock specimen:

$$Q = \frac{dV}{A \cdot dt} = -\frac{k_{abs}}{\eta}\frac{dp}{dx} \tag{6}$$

Here η is the dynamic viscosity of the fluid (Pa s), dp/dx the pressure gradient ($Pa\,m^{-1}$), A (m^2) the cross section area, and k_{abs} the absolute or intrinsic permeability (rock property).

For gaseous fluid phases, Darcy's law for compressible media must be applied:

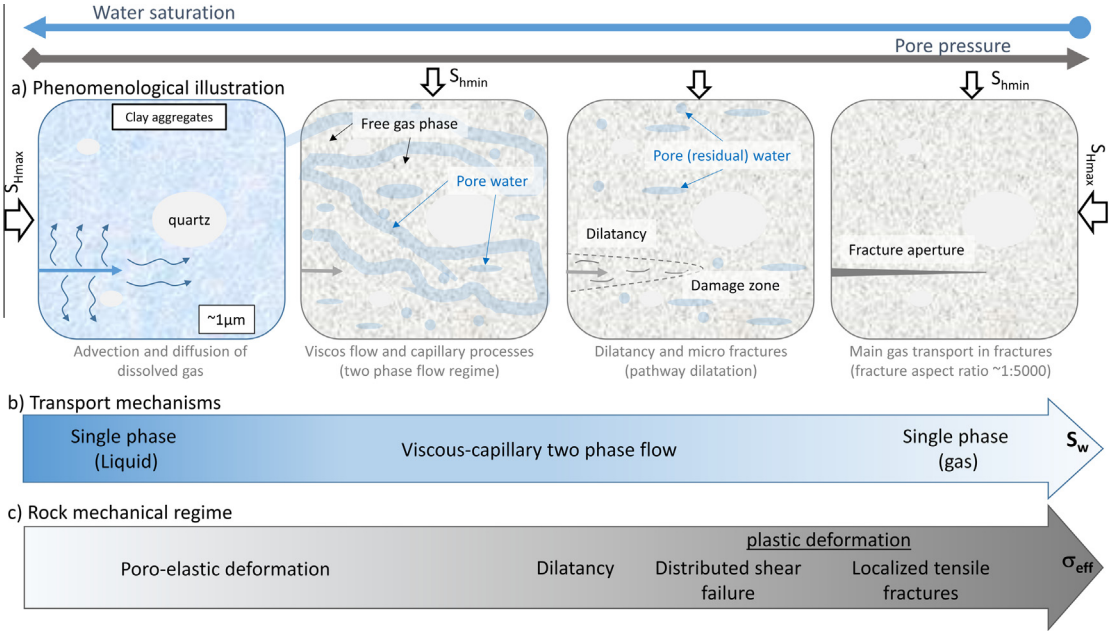

Fig. 4. Description of the four main processes of gas transport in clays (modified after Marschall (2005)). (A) Shows a phenomenological description based on the common microstructural concept considering the microporous pore structure and the viscoplastic mechanical behavior of clay-rich shales. (B) Shows the basic transport processes as a function of water saturation. (C) Illustrates the geomechanical regimes as a function of effective stress. It should be noted that the aspect ratio of a hydraulic fracture is typically around 1:5000, based on consideration that fracture length and aperture do not change independent of each other. The aspect ratio depends on geomechanical shale properties and the difference between the least principle stress and pore pressure (see Appendix for details, E = 3GPa, ν = 0.3 and $\Delta\sigma$ = 0.3 MPa, Zoback (2007)).

$$Q_2(p_2) = \frac{dV_2}{A \cdot dt} = \frac{k_{gas}(p_1^2 - p_2^2)}{2 \cdot dx \cdot \eta \cdot p_2} \quad (7)$$

Here $Q_2(p_2)$ in (m s^{-1}) is the volume flux of the gas on the low-pressure side, p_1 and p_2 (Pa) are the absolute pressures on the up- and downstream side, respectively, η (Pa s) is the dynamic viscosity of the gas, dx (m) the sample length and A (m^2) the cross section area. This approach assumes laminar gas flow and ideal gas behavior ("ideal gas law", eg. Tiab and Donaldson (2004a)). The non-ideal type of flow is considered by the theory of slip-flow.

Slip flow (Klinkenberg effect)

Slip flow (Klinkenberg phenomenon) is a non-Darcy effect that occurs when the mean free path length of the gas molecules is close to the average size of pores in a porous medium. This condition results in the acceleration of individual gas molecules along the flow path (Klinkenberg, 1941; McPhee and Arthur, 1991; Tanikawa and Shimamoto, 2006; Wu et al., 1998). Slip flow can also be interpreted as a viscosity reduction because the interactions between gas molecules and pore walls start to prevail over molecule–molecule interactions which is the definition of internal fluid friction and the basis of viscosity. Slip flow is particularly dominant in narrow fractures as well as the matrix systems of most coals, which are typically characterized by micro- and meso-scale pore throats. Because the real local pressure gradient within the porous media is unknown, an auxiliary parameter called the mean pore pressure must be introduced:

$$p_{mean} = \frac{p_{inlet} + p_{outlet}}{2} \quad (8)$$

In a comprehensive study on the permeability of porous media to liquids and gases Klinkenberg (1941) documented that the measured gas permeability coefficient is a linear function of the reciprocal of the mean pore pressure and approaches a limiting value at infinite mean pore pressure. This limiting permeability value, k_∞, which is commonly referred to as the Klinkenberg-corrected or "intrinsic" permeability, is calculated from the y-axis intercept of a plot ("Klinkenberg plot") of measured gas permeability coefficients versus the reciprocal mean pore pressure.

$$k_{app} = k_\infty \left(1 + \frac{b}{p_{mean}}\right) \quad (9)$$

In Eq. (9), b (Pa) is the gas slippage factor. The ratio of the slip factor to the mean pore pressure is proportional to the ratio of the mean free path length λ (m) to the pore-throat radius r (m).

$$\frac{b}{p_{mean}} = 4c\frac{\lambda}{r} \quad (10)$$

with c $\approx$ 1.

In the kinetic theory of gases, the mean free path of a molecule is the average distance the molecule travels between two successive collisions with another moving molecule. The mean free path length λ is a function of pressure and temperature:

$$\lambda(p) = \frac{k_B T}{\sqrt[2]{2}\pi d^2 p} \quad (11)$$

Here k_B (J K^{-1}) is the Boltzmann constant, T (K) is the temperature, p (Pa) is pressure, and d (m) is the collision diameter of the gas atoms or molecules. It should be noted that using the mean free path length is a simplification and that the Boltzmann distribution should be used in detailed considerations.

Two-phase flow systems

In a two-phase flow system the pore space is occupied by two immiscible fluids according to the wetting characteristics of the mineralogical compounds (wettability, contact angle, interfacial tension). The prevailing fluid saturation depends on capillary forces, and the effective permeability to the gas/water phase will change accordingly. The effective permeability is normalized to the intrinsic permeability to compute the "relative permeability", which is a function of fluid saturation (e.g. Tiab and Donaldson (2004b,c)).

Diffusion

Diffusion is the result of random thermal (Brownian) motion of small molecules in gases, liquids and solids. The probability of finding a molecule at a distance l from its position at time $t = 0$ can be described by a statistical distribution function which is parameterized by the factor Dt/l^2. In all practical applications this factor is of the order of 10^{-1} to 10^{1}.

While diffusion occurs permanently and ubiquitously, it only results in a net transport of molecules of a certain species when a concentration gradient is applied.

Free diffusion (bulk phases) can be readily described in terms of concentration gradients (grad C; dc/dx) according to Fick's 1st law of diffusion:

$$J = -D \operatorname{grad} C$$

Here C is the volume concentration of the diffusing species (mol m^{-3}), J is the diffusive flux (mol m^{-2} s^{-1}) and D (m^2 s^{-1}) is the diffusion coefficient. This relationship constitutes a limiting law that is strictly valid only for small concentration gradients. It may be noted here that from a thermodynamic point of view, diffusion is an entropy-driven transport process and chemical potential gradients rather than concentration gradients are considered as the driving force.

While the description of diffusive transport in homogeneous bulk phases (gases, liquids, solids) is straightforward, diffusion processes in porous media are more complex. Here particular attention has to be paid to the definition of concentrations and fluxes. For the following discussion we assume that the porous medium is filled with one homogeneous fluid phase (gas or liquid). Two-phase (gas/liquid) fluid systems are not considered here.

Inert porous media. In inert porous media the diffusing substance does not interact with the pore surfaces or the solid phase. Thus the pore system constitutes a maze of irregular interconnected flow-paths and dead-end structures. The effective distance a molecule has to travel through this system to achieve a certain absolute displacement from its original starting point is controlled by the *tortuosity* of the transport pore system. Furthermore, the *constrictivity* of the pore system denotes the degree of narrowing of pores along the interconnected transport pathways. It is evident that a high degree of tortuosity will increase the effective pathway a molecule has to travel and therefore reduce the effective diffusion coefficient. A high degree of constrictivity will reduce the effective transport cross-section area and thus the diffusive flux (at steady state).

There are different ways of describing diffusive flux in (inert) porous media, all of which are essentially equivalent.

$$J = -D_{\text{eff}} \operatorname{grad} C_{\text{bulk}}$$

$$J = -D_{\text{eff}} \cdot \phi \cdot \operatorname{grad} C$$

These relationships hold for a homogeneous porous medium with constant porosity.

Adjacent porous layers or volumes with different porosity values have to be considered separately and the dividing boundary has to be treated as a phase boundary with corresponding boundary conditions ("partition coefficients" or "equilibrium coefficients").

Ad- and absorbing porous media. An additional level of complexity is introduced when the diffusing substances (liquids or gases) interact with the surfaces and the matrix of the porous medium. This interaction may be weak and essentially negligible; it may, however, be strong enough to cause changes in the porous medium (e.g. swelling) with substantial feedback on the transport properties (moving boundary effects etc.)

For gas diffusion in coals and shales the sorptive interaction of the diffusing gases with the pore surfaces or the matrix of the porous medium is the common issue. Assuming local equilibrium in a representative element of volume of these porous media, the diffusing species will partition between the free pore fluid, the surface of the sorbent ("sorbed phase") and (for the case of organic matter) the solid matrix.

It is evident that this complexity cannot be easily resolved or described deterministically on the level of individual pores. Therefore a pragmatic approach is to treat the entire porous medium as a homogeneous bulk phase and attribute to it an apparent diffusion coefficient (D_{app}).

$$J = -D_{app}\ \text{grad}\ C_{bulk}$$

Rather than defining concentrations in the pore space or the pore-filling fluid, a bulk concentration C_{bulk} is used, that also comprises contributions by adsorbed or absorbed species. In many instances C_{bulk} cannot be readily measured or adjusted directly. Diffusion measurements in porous media are therefore mainly performed by maintaining fixed concentrations (C_{fluid}) of the diffusing substance in a fluid phase adjacent to the porous medium and measuring the resulting diffusive flux.

$$J = -P_{app}\ \text{grad}\ C_{fluid}$$

Permeation and (diffusion) permeability coefficient. The bulk rock concentration of the diffusing substance will depend on the concentration in the fluid phase. Taking a linear relationship as a first approximation an equilibrium constant ("partition coefficient") k can be defined:

$$C_{bulk} = k \cdot C_{fluid} \quad \text{or} \quad k = \frac{C_{bulk}}{C_{fluid}}$$

By means of this equilibrium coefficient the apparent diffusion coefficient can be related to the apparent (diffusion) permeability coefficient.

$$J = -\frac{P_{app}}{k}\ \text{grad}\ C_{bulk}$$

$$\frac{P_{app}}{k} = D_{app}$$

Non-steady state diffusion experiments (e.g. Antonov 1954, 1964, 1968, 1970; Krooss and Leythaeuser, 1996; Krooss and Leythaeuser, 1997; Krooss and Schaefer, 1987; Krooss et al., 1986; Krooss, 1987) provide information on the diffusion coefficient and the bulk rock concentration in equilibrium with the fluid phase concentration.

Other concentration parameters such as partial pressure may also be used for the definition of the partition coefficient.

The mobility of molecules in gases and thus their (free) diffusion coefficient depends on pressure and temperature and the molar masses, collision diameters and interaction potentials (Lennard-Jones) of the gas species. The Chapman–Enskog method (Cussler, 2009, Chapter 5.1.1) is commonly used to estimate the gaseous diffusion coefficients.

$$D = \frac{1.86 \cdot 10^{-3} T^{3/2}}{p \cdot \sigma_{12}^2 \cdot \Omega} \left(\frac{1}{M_1} + \frac{1}{M_2}\right)^{1/2} \left[\frac{\text{cm}^2}{\text{s}}\right]$$

with D in cm^2/s, p in bar, T in K and M molar mass in g/mol. Further parameters are the mean collision diameter σ_{12}^2 and the collision integral, Ω. Parameters for different gases are listed in Hirschfelder and Curtiss (1954).

Diffusion coefficients in liquids are lower by about four orders of magnitude than in dilute gases. They are mostly in the order of 10^{-9} m^2 s^{-1} and depend only weakly on solute size. The Stokes–Einstein equation (Cussler, 2009, Chapter 5.2.1) is used for their estimation. It assumes a rigid solute sphere diffusing in a continuum of solvent. The diffusion coefficient varies inversely with viscosity when the ratio of solute to solvent radius exceeds five.

$$D = \frac{k_B T}{6\pi\eta r}$$

Here η is the dynamic viscosity, r is the radius of the spherical particle, k_B the Boltzmann constant and T the absolute temperature. Diffusion rates of gases in coals are usually estimated from pressure transients during adsorption or desorption tests.

These uptake or release curves are interpreted in terms of unimodal or bimodal pore structure models. In the latter case two intrinsic diffusion coefficients (Da and Di) are defined for the macropore and micropore system, respectively.

The procedures for evaluation and interpretation of these experiments have been discussed by Busch et al. (2004), Clarkson and Bustin (1999); Nandi and Walker (1975) and Pillalamarry et al. (2011).

Knudsen "diffusion" observed during transport of gases through coals (Thimons and Kissell, 1973) is not a diffusion process in the strict sense because it occurs under the influence of a pressure gradient. It is a transitional flow regime occurring as a result of "slip flow" (see Chapter "Slip flow (Klinkenberg effect)") in the gas phase of small pores where the molecule/pore-wall interaction, in particular at low gas pressures, is becoming more important than the molecule/molecule interactions within the gas phase.

Stress conditions

Effective stress laws

Many physical properties of porous rocks, such as permeability, volumetric strain, and porosity, vary as a function of confining pressure and pore pressure according to an effective pressure law. The earliest laws of effective stress p_{eff} for soil and rock properties [e.g., Terzaghi (1923)] defined the effective stress σ_{eff} as the difference between the confining pressure and the pore pressure (Eq. (12), left illustration in Fig. 5). This is based on the observation that changes to either confining pressure or pore pressure result in identical changes in permeability. This concept is known as Terzaghi's principle. The Terzaghi effective pressure (sometimes called the simple or nominal effective stress or effective pressure law) is defined as follows:

$$p_{eff} = p_{conf} - p_{pore} \tag{12}$$

where p_{conf} is the confining pressure and p_{pore} is the pore pressure which is in pressure equilibrium equivalent to the mean pore pressure p_{mean}.

Unfortunately, this law is very simplified and has seldom been verified experimentally (Kwon et al., 2001).

In general, the effective stress law takes on the following form:

$$\sigma_{eff} = p_{conf} - \chi \cdot p_{pore} \tag{13}$$

where σ_{eff} is effective stress and χ is the effective stress coefficient for permeability (Fig. 5). When describing how volumetric strain varies with effective stress, we use the Biot coefficient, α (Biot and Willis, 1957; Nur and Byerlee, 1971). A typical observation is that the transport properties for a variety of rock types exhibit more

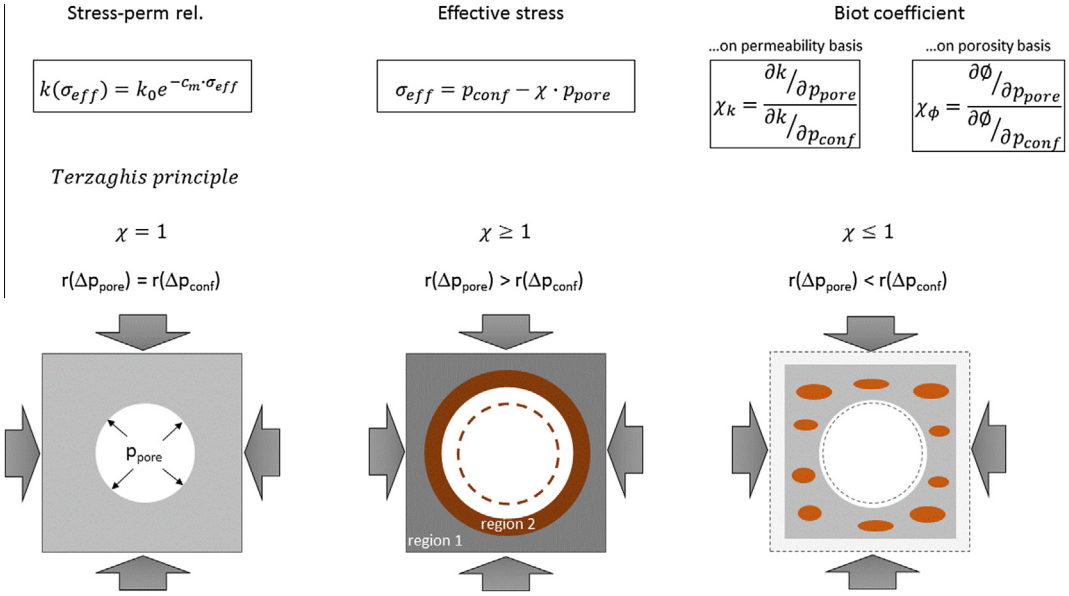

Fig. 5. Schematic illustration of a porous medium containing at least two different solids with differences in compressibility; in this case, we show calcite or quartz (gray) and clay or organic matter (brown). Soft single-phase aggregates (light gray), such as clay-rich shales, mudstones, and calcite are similarly affected by p_{conf} and p_{pore}, which results in $X \leqslant 1$. If the pores of a porous medium with high compressive strength, such as pure quartz, sandstone, or carbonates, are lined with clay, equations (X)–(Z) predict $X \geqslant 1$ (Berryman, 1992, 1993; Biot, 1941; Zoback and Byerlee, 1975b). (For interpretation of the references to color in this figure legend, the reader is referred to the web version of this article.)

sensitivity to changes in pore pressure than to changes in confining pressure (Fig. 5 and Table 3).

The effective pressure law coefficient χ may differ for different material properties of the same rock, but χ generally takes on values ($\chi \leqslant 1$) consistent with those predicted by models of porous media with fluid-filled pores and homogeneous elastic properties, which describe materials such as sandstones (Berryman, 1992, 1993; Garg and Nur, 1973; Nur and Byerlee, 1971; Robin, 1973; Walsh, 1981). Despite this generality rule of thumb, a handful of studies of clay-bearing sandstones have found χ to be greater than 1, implying that changes in pore pressure have a larger impact on permeability than changes in confining pressure (e.g. Zoback and Byerlee (1975a)). In this case (illustration in the middle of Fig. 5), the confining pressure induces only a small strain on the pore frame (region 1), owing to its low compressibility. The small strain in region 1 produces only a small stress on the highly compressible inlay (region 2), resulting in only a small strain at the pore boundary. Consequently, confining pressure has relatively little effect on the aperture of the pore throat, whereas pore pressure can produce considerable pore strain as it acts directly on the highly compressible matrix material (region 2 indicated in the middle illustration of Fig. 5).

Finally, we would like to note that in the above discussion the effective stress coefficient χ is taken to be constant, yielding a linear expression for effective pressure (Bernabe, 1987; Li et al., 2009, 2014; Gangi, 1978; Warpinski and Teufel, 1992, 1993). All the studies which report observations related to a non-linear effective stress law performed their permeability-stress experiments by pressure cycling. However, it is possible that χ may itself be a function of pore or confining pressure, or microstructural changes in the pores (Bernabe, 1987; Gangi, 1978; Li et al., 2009, 2014; Robin, 1973). Due to the large number of interacting effects, a reliable experimental deconvolution of the contributing processes would be very challenging.

Hydrofracture

During hydraulic stimulation of unconventional hydrocarbons shale is subjected to elevated pore pressures in order to create a network of induced fractures in order to link isolated porosity and disconnected natural fractures within the shale. Hydrofactures may be large features, or a linked, permeable, dilatant fracture network. These changes may be induced by the development of disequilibria pore pressure conditions or by changes in the tectonic load. Hydrofractures occur under conditions of low differential stress when pore fluid pressure reduces the minimum effective horizontal stress below zero to the tensile strength of the rock.

In extensional basins, where the minimum compressive stress (σ_3) is significantly less than the maximum compressive stress (σ_1), hydrofractures are invariably vertical to semi-vertical in orientation and form perpendicular to σ_3. For hydrofractures to develop in preference to shear fractures, the following conditions must be satisfied:

$$u_f = \sigma_3 + T_0 \quad \text{and} \quad \sigma_1 - \sigma_3 < 4T_0$$

where u_f is pore fluid pressure required to initiate hydrofracture, σ_1 and σ_3 are maximum and minimum horizontal stresses respectively and T_0 is the tensile strength of the cap-rock (King Hubbert and Rubey, 1959; Sibson, 1995). These conditions can occur naturally, however, in unconventional hydrocarbon reservoirs are created by drilling engineers.

Brittle shale will increase its permeability by developing dilatant fractures, whereas ductile shale is able to undergo plastic deformation without increasing permeability (it will contain non-dilatant, sealing fractures). The tendency to dilate will be a function of the mechanical properties of the rock, effective pressure and shear zone geometry. At a given effective pressure, a stronger (overconsolidated or cemented) rock is more likely to dilate than a weaker clay-rich one.

Considerable research has been conducted in connection with the engineering of wells to investigate the generation of artificial hydraulic fractures, in particular hydrofracs. The hydrofrac (HF) test measures in-situ stress down a borehole by increasing the pore fluid pressure in an isolated segment until tensile hydraulic fracturing is initiated, identified by a drop in pore fluid pressure. Breakdown pressure, u_c, is defined as the borehole pressure necessary to initiate hydraulic fracturing. There are two classical HF

criteria to establish equations between u_c and in-situ horizontal principal stresses (Song et al., 2001); one is based upon elastic theory for impermeable rocks (Hubbert and Willis (1957); the other upon poroelastic theory and considers the poroelastic stress induced by fluid permeation into rocks (Haimson and Fairhurst, 1967). This has been extended to include the characteristics of the bore during pressurisation (Garagash and Detournay, 1997).

Hubbert and Willis (1957):

$$u_c - u_0 = T_{hf} - 3\sigma_h + \sigma_H - 2u_0$$

Haimson and Fairhurst (1967):

$$u_c - u_0 = \frac{T_{hf} + 3\sigma_h - \sigma_H - 2u_0}{2 - 2\eta}$$

Garagash and Detournay (1997):

$$u_c - u_0 = \frac{T_{hf} + 3\sigma_h - \sigma_H - 2u_0}{1 + (2 - 2\eta)h(\gamma)}$$

where σ_h and σ_H are the minimum and maximum horizontal principal stresses, respectively, u_0 is initial pore pressure in the rock formation, T_{hf} is the hydraulic fracturing tensile strength, and η and γ are the poroelastic parameter and dimensionless pressurisation rate respectively, given by:

$$\eta = \frac{\alpha(1-2\nu)}{2(1-\nu)} \quad 0 \le \eta \le 0.5 \quad \gamma = \frac{A\lambda^2}{4cS} \quad 0 \le \lambda \le \infty$$

where α is the Biot parameter (Biot and Willis, 1957), ν is the Poisson ratio, A is borehole pressurization rate, λ is the microcrack length scale, c is the diffusivity coefficient, and S is stress.

Experimental methods

Fluid flow (permeability, capillary pressure)

In-situ measurements on sealed core plugs

Several methodologies exist that have been designed to investigate specific aspects of multi-phase flow in low-permeability argillaceous rocks; of importance to the understanding of unconventional hydrocarbons is baseline permeability, storage (i.e. effective porosity), fracture transmissivity, gas entry pressure, gas breakthrough pressure, capilliary threshold pressure, and the influence of effective stress on flow and deformation. These parameters allow an understanding of the flow and release of gas from a shale. The experimental methodologies generally fall within three broad classifications; steady-state, pulse-decay, and oscillation techniques. Within these classifications there are also methods such as step-by-step, racking, dynamic and residual methods. Reviews of different laboratory methods have been made by Egermann et al. (2006) and Boulin et al. (2013). Each method has pros and cons and generally there is a trade-off to be made between accuracy of measurement and duration of experimentation. All tests are performed on jacketed cylindrical samples of shale, with a confining pressure creating a hydrostatic stress on the outside of the jacket. Some experimental groups also include axial loading to create a heterogeneous stress state, more akin to downhole conditions. Permeability is measured using increased/decreased pore pressure at either end of the test sample. The differences between the experimental procedures derive from how the upstream and downstream pore pressure systems are operated.

The steady-state (or standard) permeability test maintains a constant back pressure (in most cases atmospheric) at the downstream-end, while increasing pore pressure at the upstream-end of the sample. This can either be done using a step-by-step increase in pressure, or by using constant injection-rate pressure ramps (or a combination of the two). As gas starts to migrate through the sample an outflow is detected from the downstream-end of the sample. Flow is continued until the steady-state condition of outflow equal to inflow is established. Permeability can then be determined at steady-state conditions. Due to the low permeability of shale the attainment of steady-state can take prolonged amounts of time.

Many authors investigating very low permeability measurements use a transient upstream gas pressure, following the pulse decay method first proposed by Brace et al. (1968). Gas pressure is suddenly increased on the upstream end of the sample. Pore pressure is monitored at both ends of the sample. As flow occurs the upstream pressure decreases and the downstream pore pressure increases until the pressure at both ends of the sample equilibrates. The pressure response can be used to determine the permeability of the sample. In order to perform this test an idea of the gas entry pressure is required as the initial gas pressure generally needs to be twice this. In water permeability tests the pressure either side of the sample will be equivalent. However, in gas testing when the downstream pressure is high enough an imbibition process starts and gas migration stops. The pressure difference, or Residual (Hildenbrand et al., 2002), between the upstream and downstream ends is assumed to equal the gas entry pressure.

With the dynamic approach (Egermann et al., 2006), gas is injected at a pressure at the upstream end of the sample at a constant pressure sufficient to initiate gas flow. Water is displaced until gas is in contact with the sample. Back pressure is maintained constant at the downstream end of the sample. Two flow rates are observed; before and after gas entry and from these data it is possible to determine gas entry pressure and permeability.

The racking method (Meyn, 1999) is similar to the dynamic, however, a pump is placed at the downstream end to extract water at a constant flow rate. Three stages are observed (1) water moves into the sample at the upstream end, with pressure equalising with the downstream end; (2) gas becomes in contact with the sample at a pressure insufficient for gas entry and as a result of continued pore water extraction the pressure in the downstream end starts to decrease; (3) pore pressure within the sample decreases as a result of downstream pressure decay until effective pressure is sufficient to cause gas entry. The pressure in the downstream end decreases by an amount equal to the gas entry pressure.

The pore pressure oscillation method (Kranz et al., 1990) applies a sinusoidally varying pressure in the upstream reservoir of the sample. This pressure wave is transmitted to the downstream end of the sample. Permeability is determined from the phase offset and amplitude reduction of the downstream pore pressure response.

Each of the experimental procedures has clear pros and cons; for instance the steady-state method can be viewed as representing down-hole conditions closely, but experimental duration as a result is long. Conversely the dynamic method is quick, but its representativeness is poor to medium (Boulin et al., 2013). Several methodologies require known parameters, such as gas entry pressure, in order to create conditions required for gas flow, whereas the standard method aims to quantify all parameters at in-situ conditions without bias from pre-selection of boundary conditions.

GRI method

Tinni et al. (2012) have investigated the GRI-method and its limitations. They found that as particle area increased, the permeability increased up to 30 mm^2, after which permeability measurements stabilized despite further increase in particle size. They also found that permeability decreased with increasing pore pressure.

Heller et al. (2014) compared permeability measurements for shale plugs made using the GRI-method on particles between 1 and 2 mm with those derived using the steady-state method. The

permeability values obtained by the GRI method were two to four orders of magnitude lower than the plug permeability coefficient.

Mercury intrusion method

In industry, mercury injection is often used as a fast and cheap method to make estimates about the critical capillary threshold pressure. However, the validity of MIP is often discussed in literature as is has several shortcomings, like (a) the application of extremely high fluid/injection pressures up to 400 MPa, which could cause the sample to be compressed or hydro-fracked, (b) likely fabric changes during drying and sample preparation, (c) and the necessity of data conversion assuming interfacial tension values and wettability (Busch and Amann-Hildenbrand, 2013; Dewhurst et al., 2002; Houben et al., 2013; Klaver et al., 2015).

Comparison of laboratory-based techniques for characterizing matrix permeability

Steady-state permeability techniques. In recent years, various laboratory-based measurement techniques have been utilized and assessed for measurement of fluid permeability under confining pressure in low-permeability sedimentary rocks. These methods are based on either steady-state or non-steady-state measurement principles. Previous studies compared gas/water permeability coefficients derived from steady-state and non-steady-state techniques for low-permeability sedimentary rocks. Table 4 presents an overview of the experimental conditions and outcomes of these studies.

Rushing et al. (2004) and Carles et al. (2007) observed that the slip-corrected gas permeability values measured by non-steady-state technique were consistently (up to two times) higher than those measured by steady-state technique. In contrast, Freeman and Bush (1983) indicated that the difference between steady-state and non-steady-state permeability values could be less than ±5%. Rushing et al. (2004) observed that differences were more significant for lower permeability samples, in contrast to the observations made by Carles et al. (2007). Investigating chalk samples from Central North Sea (UK, Norway and Denmark), Mallon and Swarbrick (2008) observed a difference of up to three orders of magnitude between steady-state and non-steady-state permeability values. The permeating fluids used in this study were, however, not identical for steady-state and non-steady-state measurements (air, He, N_2 and brine; 30,000 ppm NaCl solution) (Mallon, 2008). In agreement with the results of Freeman and Bush (1983), Ghanizadeh et al. (2015, in preparation) observed that gas permeability coefficients obtained from the steady-state and non-steady state techniques for dry plugs were similar, differing by less than ±10%. They further observed that, for dry samples, the initial pressure difference had no effect on gas permeability coefficients measured by non-steady-state technique. For samples in the "as-received" moisture condition, however, they indicated that the non-steady-state gas permeability coefficients increased up to 50% with increasing initial pressure difference (0.6–7.5 MPa). Boulin et al. (2010) compared liquid (water) permeability coefficients measured by steady-state and non-steady-state techniques in extremely low-permeability clay-rich samples and indicated that similar results could be obtained from these two techniques when the appropriate experimental configuration is used. The experiments conducted by Amann-Hildenbrand et al. (2013), however, showed that liquid (water) permeability coefficients determined with the non-steady-state method were lower (up to one order of magnitude) than those obtained from steady-state tests, particularly for low-permeability samples (k_{abs} < 10 nD).

Samples from unconventional oil/gas reservoirs have low to extremely-low permeability coefficients, which are difficult to measure in the laboratory on a routine basis. The routine steady-state gas flow technique, which is sufficient for high-permeability rocks, may not reach the steady-state condition in a reasonable testing time for low-permeability rocks, particularly when simple experimental configurations are used (Boulin et al., 2010). Therefore, non-steady-state gas flow techniques are commonly preferred in the laboratory for measuring fluid permeability in unconventional oil/gas reservoirs.

Non-steady-state permeability techniques. Pressure-decay profile (probe) permeability, pulsed-decay permeability, pressure-decay crushed-rock permeability and oscillating pore pressure (flow) methods are the primary non-steady-state gas flow techniques for determination of permeability in the laboratory. Profile (probe) permeability coefficients are measured by forcing/flowing gas through a small injection tip pressed and sealed against the surface of an unconfined slab/plug surface (Goggin, 1993; Halvorsen and Hurst, 1990; Jones, 1994; Sutherland et al., 1993). An overview of profile (probe) permeability technique is provided by Halvorsen and Hurst (1990). Profile (probe) permeability measurements are conducted by either steady-state or non-steady-state (pressure-decay) gas flow techniques (Halvorsen and Hurst, 1990; Jones, 1994; Sutherland et al., 1993). The profile (probe) permeability technique is generally considered to be a cost-efficient method to gather large quantities of data, differentiating and quantifying the permeability of small-scale heterogeneities in rocks with permeabilities down to the microdarcy range (Halvorsen and Hurst, 1990; Jones, 1994; Sutherland et al., 1993). However, this method has some disadvantages, such as sampling a much reduced rock volume relative to plugs/cuttings; further, the tests are conducted on samples that are not subject to confining pressure. Pulse-decay permeability measurements under "in-situ" effective stress conditions can be conducted to correct profile (probe) permeability values for the "in-situ" stress conditions as demonstrated recently (Clarkson et al., 2012b; Ghanizadeh et al., 2015a,b). With the pulse-decay permeability technique the decay of a small incremental change of pressure (pressure-pulse) over a plug length is recorded to measure permeability. Discussions of the pulse-decay permeability technique are provided by Cui et al. (2009) and Metwally and Sondergeld (2011). The general solution of the pressure difference as a function of time in this method was presented by Dicker and Smits (1988) following the original work by Brace et al. (1968), the error-function solution of Bourbie and Walls (1982), the general analytical solution of Hsieh et al. (1981), Chen and Stagg (1984) and Haskett et al. (1988). With the crushed-rock technique (GRI method), the decay of a pressure-pulse subsequent to injection of gas into unconfined crushed-rock particles (20/35 US mesh size; 0.5–0.84 mm) is recorded to obtain permeability (Cui et al., 2009; Handwerger et al., 2011; Luffel et al., 1993; Sinha et al., 2012; Tinni et al., 2012). Because shale samples are likely to part along micro-fractures and bedding planes during crushing, it is generally assumed that individual cuttings contain few to no micro-fractures compared to plugs. Therefore, it has been suggested that the crushed-rock technique (GRI method) might be capable of providing a better estimation of matrix permeability compared to other techniques. This method has, however, the disadvantage of ignoring the effect of confining pressure on measured permeability coefficients (Cui et al., 2009; Handwerger et al., 2011; Luffel et al., 1993; Sinha et al., 2012; Suarez-Rivera et al., 2012; Tinni et al., 2012). With the oscillating pore pressure (flow) method, a pressure-pulse with constant amplitude and frequency is generated at the upstream side of the plug and the resulting pressure variations in the downstream reservoir are recorded to obtain the permeability. The theory and experimental details of the oscillating pore pressure method are described in previous studies (Faulkner and Sciences, 1997; Kranz et al., 1990). Fig. 6 shows the range of permeability values which could be measured by conventional steady-state, profile

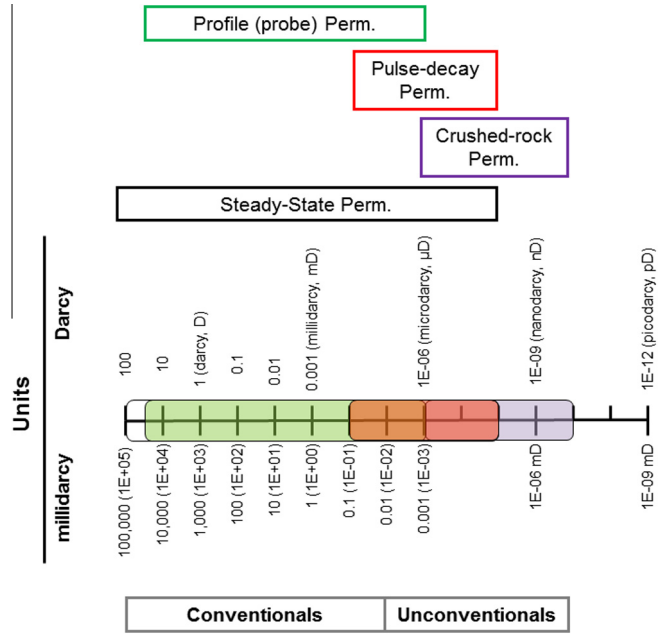

Fig. 6. This figure illustrates the typical ranges of permeability for different reservoir classification and the permeability characterization methods which are used at specific rock permeability ranges.

Table 3
The three regions of effective stress coefficients. (Nur and Byerlee, 1971). Values for $X < 1$ are taken from Bernabe (1987, 1992), Berryman (1992, 1993), Garg and Nur (1973), Heller et al. (2014), Kranzz et al. (1979), Nur and Byerlee (1971), Paterson (1983), Robin (1973), Walsh (1981). The values for $X > 1$ are taken from Warpinski and Teufel (1993), Zoback and Byerlee (1975a).

Effective stress coefficient	Principle	Mechanism	Geological rock types
$\chi = 1$	Terzaghi (1923) (isotropic medium)	Pore pressure and confining pressure changes result in the similar changes in porosity and permeability	Porous media with fluid-filled pore and homogeneous elastic properties of the solid such as Illite-rich Wilcox shale (Kwon et al., 2001)
$\chi \geqslant 1$	Load-carrying frame around the pore (low compressibility) with a high compressible inlay	Porosity and permeability show increased sensitivity to changes in pore pressure; slip-flow contribution need to be excluded	1 and 7.0 for sandstones with clay contents up to 20% (e.g. Berea Sandstone) (Zoback and Byerlee, 1975a)
$\chi \leqslant 1$	Highly compressible rock matrix	Porosity and permeability become more sensitive to changes in confining pressure	0.15–0.4 for clay-rich shales 0.6–0.85 for carbonates and quartz-rich shales 0.5–1.0 for granites and crystalline rocks 0.6–0.75 for quartz or sandstones

(probe), pulse-decay, crushed-rock and oscillating pore pressure permeability techniques for typical conventional and unconventional reservoirs.

Despite the extensive use of these techniques by different commercial/research laboratories, only a few studies have compared the outcomes of these different measurement techniques as applied to low-permeability rocks. Table 5 presents an overview

Table 4
Experimental conditions and outcomes of the previous studies comparing steady state and non-steady-state techniques for measurements of gas/water permeability on low-permeable shales (modified after Ghanizadeh et al., 2015, in preparation).

Type(s) of rock	Porosity (%)	Permeability (m^2)	Methods/permeate(s)	Main conclusion(s)	Authors
Sandstones	n.a.	4×10^{-19} m^2–3.5×10^{-16} m^2 (0.4 µD–350 µD)	Steady state gas flow/Air Non-steady state gas flow/Air	$k_{\infty,non\text{-}steady\ state} \approx k_{\infty,\ steady\ state}$ (by less than ±5%)	Freeman and Bush (1983)
Sandstones	4–12	7×10^{-19} m^2–1×10^{-16} m^2 (0.7 µD–100 µD)	Steady state gas flow/He, N_2 Non-steady state gas flow/He	$k_{\infty,\ steady\ state} \ll k_{\infty,\ non\text{-}steady\ state}$ (up to 2 times; higher differences for ***lower*** permeable samples)	Rushing et al. (2004)
Sandstones Carbonates	2–22	2×10^{-19} m^2–3×10^{-17} m^2 (0.2 µD–30 µD)	Steady state gas flow /N_2 Non-steady state gas flow/N_2	$k_{\infty,\ steady\ state} \ll k_{\infty,\ non\text{-}steady\ state}$ (up to 2 times; higher differences for ***higher*** permeable samples)	Carles et al. (2007)
Chalks	3.5–32.2	1×10^{-21} m^2–1.25×10^{-15} m^2 (1 nD–1250 µD)	Steady state gas flow /Air,He,N_2 Non-steady state liquid flow/(30 g/l NaCl solution)	$k_{abs,\ non\text{-}steady\ state} \ll k_{\infty,\ steady\ state}$ (up to 3 orders of magnitude)	Mallon and Swarbrick (2008)
Clays	n.a.	8×10^{-22} m^2–2.75×10^{-19} m^2 (0.8 nD–275 nD)	Steady state liquid flow/water Non-steady state liquid flow/water	$k_{abs,\ non\text{-}steady\ state} \approx k_{abs,\ steady\ state}$ (by less than ±10%)	Boulin et al. (2010)
Clays	3.3–23	3×10^{-22} m^2–3.8×10^{-18} m^2 (0.3 nD–3.8 µD)	Steady state liquid flow/(10 g/l NaCl solution) Non-steady state liquid flow/(10 g/l NaCl solution)	$k_{abs,\ non\text{-}steady\ state} \ll k_{abs,\ steady\ state}$ (up to one order of magnitude; higher differences for ***lower*** permeable samples)	Amann-Hildenbrand et al. (2013)
Organic-rich shales	13.7–16.6	4×10^{-20} m^2–3.7×10^{-19} m^2 (40 nD–370 nD)	Steady state gas flow /He Non-steady state gas flow /He	$k_{\infty,\ non\text{-}steady\ state} \approx k_{\infty,\ steady\ state}$ (by less than ±10% for dry samples)	Ghanizadeh et al. (2015, in preparation)

Table 5
Experimental conditions and outcomes of the previous studies comparing different non-steady-state techniques for measurements of gas permeability on low-permeability shales (modified after Ghanizadeh et al., 2015a).

Rock type	Locality	Porosity (%)	Permeability (mD)	Methods/permeate(s)	Main conclusion(s)	Authors
Organic-lean Shales	Lower Triassic, Montney Formation (Alberta, Canada)	2–9	1.3×10^{-4}–3×10^{-2}	Profile (probe) permeability/ N_2 Pulse-decay permeability/ N_2	$k_{Profile} \geqslant k_{Pulse\text{-}decay}$ (profile permeability values were corrected for in-situ stress conditions; higher differences for higher permeability samples)	Clarkson et al. (2012a)
Organic-rich Shales; Silty-laminated Shales	n.a.	2–8	3×10^{-5}–1×10^{-1}	Crushed-rock permeability/ He Pulse-decay permeability/N_2	$k_{Pulse\text{-}decay} \geqslant k_{Crushed\text{-}rock}$ (depending on lithology and axial/confining pressure used in pulse-decay tests)	Handwerger et al. (2011) and Suarez-Rivera et al. (2012)
Organic-rich Shales	Ordovician, unknown formation	n.a.	1×10^{-6}–1×10^{-1}	Crushed-rock permeability/ He, N_2 Pulse-decay permeability/N_2	$k_{Pulse\text{-}decay} \geqslant k_{Crushed\text{-}rock}$	Tinni et al. (2012)
Organic-lean and Organic-rich Shales (0.9–3.3% TOC)	Lower Triassic, Montney Formation (British Columbia, Canada)	1.8–9.5	2×10^{-5}–2×10^{-2}	Crushed-rock permeability/ He Pulse-decay permeability/He	$k_{Pulse\text{-}decay} \geqslant k_{Crushed\text{-}rock}$ (up to two orders of magnitude)	Cui et al. (2013)
Organic-lean and Organic-rich Shales (0.9–3.3% TOC)	Lower Triassic, Montney Formation (British Columbia, Canada)	1.8–9.5	2×10^{-5}–2×10^{-2}	Crushed-rock permeability/ He Pulse-decay permeability/He	$k_{Pulse\text{-}decay} \geqslant k_{Crushed\text{-}rock}$ (up to two orders of magnitude)	Cui and Brezovski (2013)
Organic-rich Shales (1% < TOC)	Late Devonian, Duvernay Formation (Alberta, Canada)	1.0–6.5	3.7×10^{-7}–1.2	Profile (probe) permeability/ N_2 Pulse-decay permeability/N_2 Crushed-rock permeability/ He	$k_{Profile} \geqslant k_{Pulse\text{-}decay} \geqslant k_{Crushed\text{-}rock}$ (depending on sample conditions; profile permeability values were corrected for in-situ stress conditions)	Ghanizadeh et al. (2015a)
Organic-lean Silty Shales (TOC < 1%)	Lower Triassic, Montney Formation (Alberta, Canada)	2.1–6.0	1×10^{-7}–1×10^{-2}	Profile (probe) permeability/ N_2 Pulse-decay permeability /N Crushed-rock permeability/ He	$k_{Profile} \geqslant k_{Pulse\text{-}decay} > k_{Crushed\text{-}rock}$ (profile permeability values were corrected for in-situ stress conditions)	Ghanizadeh et al. (2015b)

of the experimental conditions and outcomes of these studies. Comparing profile (probe) and pulse-decay permeability techniques, Clarkson et al. (2012b) indicated that, for Montney Formation samples, uncorrected profile (probe) permeability values for "in-situ" stress were consistently (up to one order of magnitude) higher than corresponding pulse-decay permeability values. They indicated, however, that corrected profile (probe) permeability values for "in-situ" effective stress were comparable with pulse-decay permeability values. For Duvernay Formation samples, Ghanizadeh et al. (2015a) showed recently that, in the cleaned/dried state, profile (probe) permeability values, both uncorrected (1.9×10^{-2}–1.2 mD) and corrected (5.8×10^{-5}–1.4×10^{-2} mD) for "in-situ" stress, are consistently higher than pulse-decay (8.4×10^{-5}–7.6×10^{-4} mD) permeability values. Comparing profile (probe) and crushed-rock permeability techniques, Ghanizadeh et al. (2015a), indicated that, in the "as-received" state, profile (probe) permeability values, both uncorrected (3.7×10^{-4}–2.7×10^{-2} mD) and corrected (1.5×10^{-5}–5.7×10^{-4} mD) for "in-situ" stress, are consistently higher than crushed-rock (3.7×10^{-7}–5.9×10^{-6} mD) permeability values. Similarly, in the cleaned/dried state, they showed profile (probe) permeability values, both uncorrected (1.9×10^{-2}–1.2 mD) and corrected (5.8×10^{-5}–1.4×10^{-2} mD) for "in-situ" stress, are consistently higher than crushed-rock (3.8×10^{-5}–1.1×10^{-3} mD) permeability values. Comparing pulse-decay and crushed-rock permeability techniques, previous studies (Brezovski and Cui, 2013; Cui et al., 2013; Handwerger et al., 2011; Suarez-Rivera et al., 2012; Tinni et al., 2012) show that the pulse-decay permeability values can be higher or equal to crush-rock permeability values, depending on lithology and effective stress used in pulse-decay permeability tests. In the cleaned/dried state, (Ghanizadeh et al., 2015a) indicated that pulse-decay permeability values (8.4×10^{-5}–7.6×10^{-4} mD) determined for Duvernay Formation samples are comparable with crushed-rock (3.8×10^{-5}–1.1×10^{-3} mD) permeability values. For organic-rich and silty-laminated shales with permeability values ranging between 3×10^{-5} and 1×10^{-1} mD, Handwerger et al. (2011) compared pulse-decay permeability coefficients, measured over an axial/confining pressure range of 1.5–40.5 MPa to those obtained from crushed-rock permeability analysis. They showed that pulse-decay permeability coefficients were higher than or equal to crushed-rock permeability coefficients, depending on lithology and effective stress. For organic-rich shales, in particular, the pulse-decay permeability coefficients, measured at high axial/confining pressures (>27 MPa) were well comparable with crushed-rock permeability coefficients. However, for silty-laminated shale, the pulse-decay permeability coefficients at high axial/confining pressures (>27 MPa) were consistently higher than or equal to crushed-rock permeability coefficients, depending on sample-to-sample variations. For Ordovician shales with permeability coefficients ranging between 1×10^{-6} and 1×10^{-1} mD, Tinni et al. (2012) showed that pulse-decay permeability coefficients were generally higher than crushed-rock permeability coefficients. For samples from Montney Formation (Canada) with permeability coefficients ranging between 2×10^{-5}–2×10^{-2} mD, Cui et al. (2013) and Brezovski and Cui (2013) indicated further that pulse-decay permeability coefficients were consistently higher (up to three orders of magnitude) than crushed-rock permeability coefficients. For samples from Montney Formation ("as-received"), Ghanizadeh et al. (2015b) indicated that profile (probe) permeability values (9.2×10^{-4}–7.3×10^{-2} mD) were consistently higher than pulse-decay (1.6×10^{-5}–3.9×10^{-2} mD) and crushed-rock (3.3×10^{-6}–4.6×10^{-5} mD) permeability values.

Ghanizadeh et al. (2015b) indicated, however, that corrected profile (probe) permeability values for "in-situ" effective stress (5.3×10^{-5} – 2.5×10^{-2} mD) were comparable with the pulse-decay (1.6×10^{-5}–3.9×10^{-2} mD) permeability values.

The observed difference between pulse-decay permeability and crushed-rock permeability coefficients, according to Cui et al. (2013) and Brezovski and Cui (2013), could be due to the (partial) absence (or limited number) of micro-fractures present in individual grains compared to plugs and/or the orientation-dependence of pulse-decay permeability tests. Permeability, is a tensor quantity with magnitude and orientation within the porous solid. The pulse-decay permeability method is capable of measuring permeability in a particular direction with respect to the core plug; parallel to the axis of the core plug (an arithmetical average of permeability). However, crushed-rock permeability method is capable of measuring permeability in multiple directions within the rock grains, and therefore, provides a geometrical average of permeability. The observed difference between these two methods could be, therefore, partly due to the orientation-dependency of the pulse-decay permeability method. The tests performed by (Handwerger et al., 2011) indicated that, regardless of lithology, the discrepancy between the permeability coefficients obtained from crushed-rock and pulse-decay permeability method decreases with increasing axial/confining pressures (>27 MPa). At higher axial/confining pressures, Handwerger et al. (2011) associate the observed smaller difference between these two methods to the closure of micro-fractures (either naturally-induced or artifacts) in the plugs.

The observed difference between profile (probe) permeability (uncorrected for "in-situ" stress) and pulse-decay permeability values are expected since these two methods differ in the volume of the rock sampled during the tests and the experimental conditions (absence/presence of axial/confining pressure) (Clarkson et al., 2012b; Ghanizadeh et al., 2015a,b). Because the lower limit of profile permeability technique is 1 microdarcy, in an absolute sense, it is of limited value for low-permeability shales which commonly have permeabilities down to the nanodarcy range (Ghanizadeh et al., 2015a,b). The permeability coefficients obtained from this technique are not representative of the "in-situ" values primarily due to two reasons: (1) measurements are not performed under "in-situ" confining stress, and, (2) a reduced rock volume is sampled during the tests compared to pulse-decay and crushed-rock tests. As demonstrated in previous studies for low-permeability rocks (Clarkson et al., 2012b; Ghanizadeh et al., 2015a,b, Solano et al., 2012), however, the only reasonable (but still not perfect) approach that can be used to partly overcome the shortcomings of this method, and make it meaningful for quantitative permeability evaluation in low-permeability shales, is to combine it with pulse-decay permeability tests. Pulse-decay permeability tests can be conducted under "in-situ" effective stress conditions on plugs sampled at the same location as profile permeability tests conducted on the core slab. These tests can then be used to correct profile permeability values for the "in-situ" stress conditions. This approach is, however, only an approximation because (1) the derived correlation between profile (probe) and pulse-decay permeability is often only of fair quality, and, (2) the pulse-decay and profile tools sample a different rock volume.

Experimental challenges

Although laboratory tests are the only way to obtain information on fluid transport properties of coals/shales under controlled and adjustable conditions they carry some inherent limitations. As an example, sample sizes are significantly smaller than representative elements of volume (REV) for micro-fracture distribution or alternating sequence of quartz-clay in shale seams. Furthermore, highly permeable (fractured or brittle) shale samples are mechanically not very stable and tend to fail during plug drilling. This results in a "natural selection" of the drilled plugs during the sample preparation procedure. Nevertheless, laboratory observations based on differential permeability evaluation, like stress sensitivity or pore throat compressibility and slip flow, are still reliable and meaningful and provide valuable insight into mechanisms and processes.

Sakhaee-Pour and Bryant (2012) analyzed the effects of adsorbed layers of methane (CH_4) and gas slippage at pore walls on gas flow behavior. Reduction of the micro-pore throats of shales by adsorption can be significant because both occur on the same spatial scale. The combined effects of adsorption and slip depend strongly on pore pressure and on pore throat diameter (Niu et al., 2014). Niu et al. (2014) found that laboratory measurements performed using non-sorbing gas as a permeating fluid overestimates the apparent gas permeability at early stages of production by a factor of four.

To entirely characterize the transport properties of compressible porous or fractured media, the apparent permeability has to be determined at various pore and confining pressures ideally using the gas composition of the reservoir or methane as a first approximation.

The entire characterization considering the coupling of slip flow and poroelasticity, includes the following parameters and experimental conditions:

- The effective stress coefficient χ, using at least 3 different confining stress conditions, the pore pressure should be high (10 MPa or higher) to avoid a slip flow contributions, the confining stress should be ideally around in-situ stress conditions to avoid contribution by artificial micro-fractures.
- The effective stress sensitivity coefficients c_m and the intrinsic zero-stress permeability k_0, the pore pressure should be high to avoid contribution from slip flow or using the "true" permeability values k_∞ (Eq. (9)), note the stress sensitivity is not effected by the choice of the effective stress coefficient however the intrinsic zero-stress permeability coefficient k_0 is affected by this choice. Further, we discuss later in this review the dependence of cm on moisture in pore network of shales.
- The slippage factor $b(\sigma)$, for the experimental determination low pore pressure should be used (0–2 MPa) for at least three different confining stress conditions.

All four parameter are required to calculate the permeability in reservoirs under varying stress situations. Furthermore stress equilibration in shales is a slow viscoelastic dominated process. This has to be taken into account during the experimental determination. Initial equilibration times up to 2 weeks and even longer have been reported (Vermylen, 2011).

Finally, diffusion and advection (Darcy) flows cannot be differentiated experimentally within matrix permeability analyzes in the nanodarcy range ($\sim 10^{-21}$ m^2) (Cui et al., 2009). The contributions of concentration driven transport processes have to be determined separately.

Transport in shale reservoirs (large and small scale)

Evidence from production sites – large scales

Records of gas and water production volumes made during gas production contain valuable information about reservoir transport processes. They allow for analysis of the transport characteristics of the reservoir as a whole because they reveal the results of the

complex interplay between all superimposed and coupled transport and poro-elastic processes.

In addition, by recording compositional changes during production, we obtain valuable information on micro-scale processes such as gas release kinetics, diffusion, slip flow, and affinity to sorption sites.

In the following chapter we focus on the analysis of gas production data to improve our understanding of the physical transport processes which occur during reservoir exploitation and depletion. We are only able to provide a brief introduction into this topic here - more detailed summaries can be found in the review papers of Clarkson (2013a,b).

Production curve

One of the primary tasks of a petroleum reservoir engineer is to use historical production data to (1) estimate reservoir properties (permeability and contacted-gas-in-place volume) and (2) forecast production performance as a means of estimating reserves and evaluating economic viability.

Production data provides useful, though limited, information about flow processes occurring within the reservoir. One of the limitations of production data is that it describes the overall effect of a variety of superimposed transport processes. For example, records of gas and water production rates over longer time periods provide some information on the sensitivity of the relative permeability of the reservoir to changes in effective stress. However, this effect is superimposed on changes in liquid saturation, which also change the relative permeability.

In this chapter we will briefly discuss production curves and their interpretation in terms of transport processes in unconventional reservoirs.

Methods

There are analytical, numerical and empirical methods for analyzing production data. In this section, however, only the empirical approaches are discussed. The empirical approaches cannot be used to extract reservoir information – this can only be done using analytical or numerical models that use an actual physical model of the reservoir. Detailed overview of the methods for analyzing production data in shales are provided in Clarkson (2013a,b). Arps (1945, 1956) and Fetkovich (1980) formulated a comprehensive set of equations defining exponential, hyperbolic and harmonic production decline curves. Arps' equations are strictly valid for boundary-dominated flow. Fetkovich combined Arps' curves with transient flow solution in dimensionless form to create production type-curves. They are only valid for boundary-dominated flow conditions. For conventional reservoirs, the decline curve parameter, b, lies between 0 and 1. However, for transient flow in unconventional reservoirs, a much higher value for b is required. This value is typically around 2.5 (Fig. 7).

$$q(t) = q_0 \frac{1}{[1 + bD_i t]^{1-\frac{1}{b}}} \tag{14}$$

Eq. (14) is showing the gas production rate following an approach of Arps (1945, 1956). However, Valko and Lee (2010) propose the use of stretched exponential functions instead of the Arps equations, because the mathematical properties of a stretched exponential function are more favorable especially for extrapolations (Can and Kabir, 2012). In addition, as highlighted before, Arps' curves are strictly valid for boundary-dominated flow where the b value is less than 1 and usually constant. For transient flow, the b value changes with time and newer techniques like the stretched exponential time approach are attempts to model the transient flow period.

$$q(t) = q_0 e^{-(t/\tau)^n} \tag{15}$$

Eq. (15) shows the rate relation expressed in a stretched-exponential decline model.

Fig. 7 shows a typical production curve for an unconventional reservoir. The indicated very long tailing is one of the main characteristics of production curves of shale gas reservoirs. Two different dominant production phases can be identified:

(1) Transient flow, open reservoir, drainage area expands around each stimulated reservoir volume, no overlap between different drainage areas.
(2) Fracture interference, 'boundary' dominated flow, closed reservoir, constant drainage area, reservoir approaches depletion. Discussion of flow regime sequences in shales is provided by Clarkson (2013a).

Production curve analysis. As mentioned at the beginning of this chapter, gas production rates measure the bulk result of a variety of concurrent transport processes occurring within the reservoir during depletion. In an unconventional reservoir, bulk production

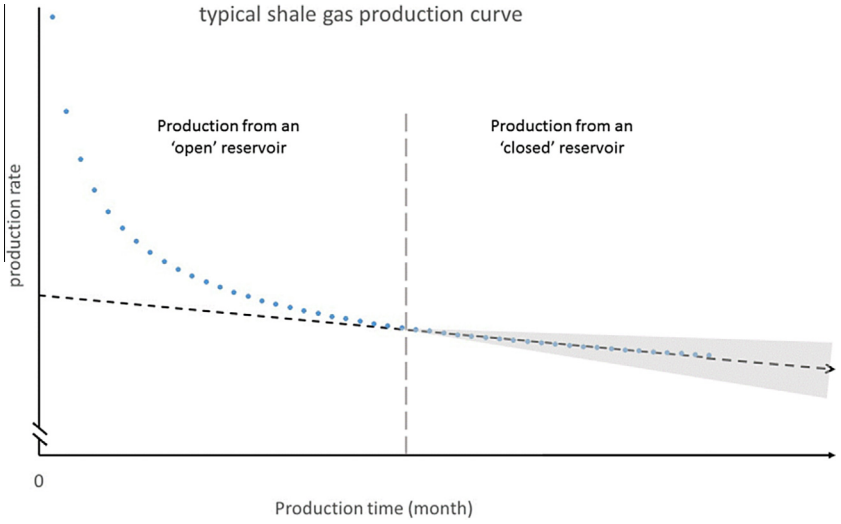

Fig. 7. A typical production decline curve. Two different production phases have been identified. In the first phase, open reservoir depletion, the production rate decays hyperbolically. The second phase, depletion of a nearly closed reservoir, is characterized by an almost linear decline (Valko and Lee, 2010).

rate data result from the interplay of all superimposed and coupled transport and poro-elastic processes. In coalbed methane or shale gas reservoirs, the rocks are much softer and changes in effective stress significantly affect transport processes.

Methods for analyzing production data in unconventional reservoirs continue to evolve as our understanding of the underlying physics of fluid storage and flow improves. For example, analytical methods, which include type-curves, flow-regime analysis and analytical simulation, have recently been modified to account for desorption of gas, multi-phase flow, non-Darcy flow (slip flow and diffusion), and non-static (stress-dependent) permeability (Song and Ehlig-Economides, 2011; Ozkan et al., 2011). A detailed discussion of these methods is beyond of the scope of this review paper. For further reading, we recommend to read the review of Clarkson and his co-workers (Clarkson, 2013a,b).

The analysis of production data is often the only practical way to evaluate tight gas and shale gas reservoirs (Mattar, 2008; Valko and Lee, 2010). However only in combination with reliable laboratory experiments this records enables us to improve understand of the physical processes and mechanisms.

Production phases and attributed transport mechanism

The gas flow in shale reservoirs is a combination of desorption and diffusion within the micro-pores. In the micro- and meso-pore throats the gas transport is dominated by slip flow process. The micro- and meso-pore throats feed the macro-pores of the matrix where Darcy flow is the dominating transport mechanism within fractures networks. During reservoir depletion the pore pressure changes which causes shifts in the dominating transport processes (Table 6). Production curves are typically divided into four to six different transport phases, which are differentiated by changes in flow mechanisms and flow rates. Two clear phases can be easily identified in the production curve shown in Fig. 7. Detailed overview of flow regime sequences in shales is provided by Clarkson (2013a).

In general, certain key reservoir processes and attributes have to be considered in order to formulate an accurate physical description of flow behavior in an unconventional reservoir. These key reservoir processes/attributes include:

- Gas release kinetics related to organic matter and clays (desorption, diffusion).
- Dual or ternary porosity and permeability behavior caused by pre-existing natural fractures and induced hydraulic fractures.
- Nano-Darcy scale matrix permeability.
- Highly anisotropic permeability.
- Stress-dependent porosity and permeability changes related to highly compressible fractures and matrix pore volumes.
- Non-Darcy flow, including slip-flow and diffusion within the shale matrix.
- Multi-phase flow of gas, water, and/or condensate.
- Reservoir geometry.
- Reservoir heterogeneities, including multi-layers (ex. anisotropic permeability) and lateral heterogeneity.
- Stress dependence of slip flow and multi-phase flow (contribution to bulk production behavior unclear).

Gas composition changes during production

Changes in gas composition during production has been reported for decades (Schettler and Pamley, 1989). These changes can provide useful information about the micro-scale characteristic behavior of the reservoir system. However, these compositional changes are partially induced by production operations. In order to make use of the information, we must first deconvolute basic reservoir response from changes in boundary conditions induced by production operations, a task that can be extremely difficult (Freeman et al., 2012). Despite these challenges, even if deconvolution is not possible, systematic operationally induced condition changes and the related shifts in produced gas composition may provide useful diagnostic information about micro-scale reservoir production processes.

Only a few studies have attempted to understand the compositional changes occurring during production from coal and shale gas (Blasingame et al., 2013; Freeman et al., 2012) reservoirs. Multiple distinct physical phenomena influence the behavior of fluids in shale gas reservoirs and cause measurable compositional changes in produced gas over time. Many compositional changes over the course of production are due to differences in desorption and diffusion coefficients and thermodynamic phases between different produced gases (Blasingame et al., 2013). In addition, composi-

Table 6
Gas production phases and the attributed physical flow mechanisms.

	Reservoir	Mechanisms	Timing
1. Stage	Depletion of the primary fractures Considered an "open" reservoir depletion	Fracture flow Multi-phase flow depending on hydraulic fracturing operations Proppant embedment	Hours to first days
2. Stage	Flow from the matrix through the primary fracture network. The secondary fracture network will be depleted to a level where out-flux and in-flux from the shale matrix are equal. The depletion front is indicated with a doted red line. The pressure in the shale fracture system decreases significantly. Considered an "open" reservoir depletion	Fracture flow Matrix permeability (high pore pressure, laminar flow) Proppant embedment	First days to weeks
3. Stage	The drainage area expands deeper into the shale matrix; drainage areas of different fractures start to overlap. The pressure in the shale matrix starts to decrease significantly. At this stage the reservoir is considered nearly "closed"	Matrix flow (low pore pressure) Slip flow, diffusion, Single phase flow	Months to years
4. Stage	Boundary flow and depletion of the shale matrix. The drainage area reaches its maximum. The reservoir is considered "closed", depletion is similar to the depletion of a tank	Matrix flow Slip flow, diffusion, Single phase flow Flow contributions from neighboring formations	Years to decades

tional changes could be caused by differences in affinity to sorption sites, gas release kinetics and slip flow behaviors. In Fruitland coals, for example, it is well known that methane and carbon dioxide concentrations change in the produced gas stream primarily due to relative sorption affinity. The concentration change in this case occurs in the absence of phase changes. The impact of compositional changes can be especially significant for slip flow (slippage factor) (Ghanizadeh et al., 2013; Sinha et al., 2013) and diffusion processes (Krooss, 1986). The simplified simulation approach performed by Blasingame et al. (2013), which includes diffusion, desorption processes and flow in complex fractures with diffusion through nanopores, shows significant fractionation between methane, ethane and propane, with changes of up to 10% from the initial composition.

Fracture permeability

Discontinuities (fracture, faults, joints, interfaces, etc.) play a pivotal role in controlling the movement of water and gas in many geological settings. Depending on their orientation, shear displacement, mineral composition and stress regime, fractures are important in the flow of gas/oil/water in unconventional hydrocarbon environments (shale gas/shale oil). Fractures and faults can also be the controlling structural feature retarding the flow of hydrocarbons in conventional environments, containing super-critical CO_2 in sequestration projects, and also movement of gas and/or water in radioactive waste disposal. Fracture flow has therefore been studied for a number of applications using theoretical and field- and laboratory-based techniques.

The permeability of rocks has been widely experimentally investigated under isostatic stress conditions (e.g. Clennell et al., 1999; Dewhurst et al., 1998; Ghanizadeh et al., 2013, 2014a,b; Heller et al., 2014; Katsube et al., 1991, 1992; Katsube and Williamson, 1994; Kwon et al., 2001, 2004; Morrow et al., 1984; Walsh, 1981; Zoback and Byerlee, 1975b, etc.) in order to establish the relationship between effective stress and permeability for different rock types. The reported permeability for intact shale, mudstones, and clay aggregates subjected to hydrostatic pressures varies from $10^{-16}\,m^2$ to $10^{-23}\,m^2$ (Kwon et al., 2001). Many researchers have shown that the permeability of shale decreases with increasing externally applied stress (Dewhurst et al., 1999a, b; Katsube, 2000; Katsube et al., 1991, 1992; Katsube and Williamson, 1994; Neuzil, 1994) and decreased porosity (Dewhurst et al., 1998; Schlömer and Krooss, 1997). A number of non-linear relationships have been proposed between permeability, porosity, and effective/confining stress in shale and mudstones, including exponential and power laws (Dewhurst et al., 1999a; Katsube et al., 1991).

The permeability, or transmissivity, of discontinuities and its associated relationship with stress has not been as widely reported as matrix permeability. The following summarizes the results of the experiments conducted in underground field-based research laboratories and other laboratories.

The load plate[1] experiment at the Mont Terri Underground Research Laboratory (Buehler et al., 2003) clearly demonstrated that the transmissivity of fractures in Opalinus Clay (OPA) formed within the engineered disturbed zone (EDZ) around an underground tunnel was sensitive to the normal loading experienced. Generally, the transmissivity decreased with increasing load pressures, by up to a factor of 60. However, even the reduced transmissivity observed at the highest load was still at least one order of magnitude greater than that of intact OPA.

Gutierrez et al. (2000) investigated the hydromechanical behavior of an extensional fracture in Kimmeridge Shale under normal and shear loading experimentally. It was shown that, at the time the fracture was created, it had about nine orders of magnitude higher permeability than the permeability of the intact shale. Increasing the contact normal stress across the fracture reduced the fracture permeability following an empirical exponential law. Loading the sample to an effective normal stress twice as much as the intact rock unconfined compressive strength did not completely close the fracture, although it did reduce the permeability by an order of magnitude. Cuss et al. (2011) showed that fracture transmissivity in OPA decreased linearly with an increase in normal load. This study also showed that shearing was an effective self-sealing mechanism and reduced hydraulic fracture transmissivity to similar levels to that of the intact material. Cuss et al. (2014) reported a one order of magnitude reduction in fracture transmissivity of OPA just in response to re-hydration of the fracture as a result of swelling. A further order of magnitude reduction was observed in response to shearing along the fracture. This resulted in a transmissivity similar to that observed in intact OPA. However, prolonged testing of fracture transmissivity in OPA (Cuss et al., 2011, 2014) showed that flow is not a static parameter. Continued shear resulted in several orders of magnitude increase in flow either due to the formation of a shear zone parallel with the main fracture or due to the misalignment of asperities and the opening of new flow paths.

The ability of rough fractures to retain much of their permeability in the presence of contact stresses across the fracture plane can be attributed to the microscopic structure and roughness of the fracture surfaces. Even in the case of severe loading exceeding the strength of the sediment matrix, it appears that the microscopic asperities at the fracture surface are able to keep open some space and channels along the fracture to allow for fluid flow and to maintain a degree of enhanced permeability.

Experiments conducted on artificially clay-filled fractures also offer useful insight into the flow of gas and water along fractures in unconventional hydrocarbons. Stress memory has been shown in kaolinite gouge material during load-unloading experiments (Sathar et al. (2012), with similar behavior being noted in OPA and Callovo-Oxfordian claystone. As normal load across a fracture is increased the flow through the fracture decreases. As the normal load is reduced there is little to no change in flow, even at very low normal loads. Reloading of the fracture follows a similar flow history than observed during unloading, until the highest stress state is reached, from where increased normal load results in continued reduction in flow. This has been interpreted as a consequence of the visco-plastic behavior of clay-rich rocks (Sone and Zoback, 2014). The hysteresis characteristic of flow with normal load demonstrates the importance of stress history; pre-existing fractures and faults in unconventional hydrocarbon sequences will have a flow dependent on the maximum stress state experienced and not necessarily the current stress state.

Variations have also been noted between the flow of fluids and the orientation of fractures with respect to the stress-field (Cuss et al., 2014). These experiments confirm the field observation that fractures that are critically stressed result in greater flow than those that are not (Townend and Zoback, 2000).

Repeat experimentation performed on both fault gouge material (Cuss et al., 2014) and OPA (Cuss and Harrington, 2014) has shown that the gas entry pressure of the fault is reproducible. However, once gas has become mobile within the fracture, the permeability, as inferred from the pressure response, varies between tests. This may be due to microscopic variations in the fault plane

[1] The load plate experiment was designed to investigate the flow properties within fractures around a tunnel at the Mont Terri Underground Research Laboratory. Three 133 ton hydraulic rams were placed within the tunnel enabling normal loads of between 1 and 4.8 MPa to act on the tunnel wall. Throughout the 4.5 month test the hydraulic conductivity of the tunnel wall rock was measured within packered borehole sections.

or by the localization of flow paths. During hydraulic testing of OPA, the injection of fluorescein late in the flow experiment showed that approximately 50% of the fracture surface was conductive (Cuss et al., 2011). Flow tended to preferentially follow micro-scale fractures that formed in the fracture surface. Similar flow localization has been seen in kaolinite gouge material. Pore pressure within the gouge remained low, even when gas injection pressure was high and flow was occurring within the gouge. When gas was able to escape the fault plane it did so at isolated point sources. The visualization of gas flow in gouge material (Wiseall et al., 2014) clearly showed that gas propagated along a number of localized features, similar in appearance to fractures. Therefore it can be seen that fracture flow does not always include 100% of the fracture surface.

It is clear that the evolution of fracture transmissivity is very complex. Fracture transmissivity is a function of normal stress, pore pressure, shear stress, shear displacement, fault angle, stress history, gouge composition, and chemistry of the injected fluid. Additionally the stress equilibration process is slow and in combination with visco-elastic and visco-plastic processes can cause that the apparent transmissivity temporally evolves and is only a semi static property.

The fracking process will result in a number of discrete features. The flow along these will be localized in the case of gas flow or restricted for water flow, with only a proportion of the fracture surface conductive to flow. The sensitivity of fracture flow to normal load shows that proppants are vital in order to maintain an open pathway. However, tests conducted in OPA showed that fracture transmissivity reduced by one order of magnitude through swelling alone. If shale has swelling clays present, the material will swell in response to contact with water, resulting in draping of clay around the propant. Therefore the chemistry balance between the injected fluid and the host rock may be an important consideration in the extraction of shale gas.

The release of gas within shale is dependent on a number of factors. The pervasive fracturing of the material results in connectivity of the free gas trapped within the pore space of the rock. However, significant quantities of gas are retained in the clay-rich material between the fractures. The release of this gas requires a change in pore pressure to drive gas movement, which will occur through localized pathways. Experimental observations suggest that a pervasive lowering of pore pressure may have a limited affect away from fractures, meaning that a large proportion of gas remains trapped within pore space and sorbed onto mineral surfaces (Cuss et al., 2014).

Matrix permeability

Organic-rich shales are historically almost exclusively associated with either source rocks or cap rocks. As a result, most of past studies of fluid transport processes in shales have focused on aspects of the processes relevant to these roles (Hildenbrand et al., 2002, 2004; Krooss, 1986, 1987, 1988, 1992; Krooss et al., 1986, 1988, 1991; Krooss and Schaefer, 1987; Krooss and Leythaeuser, 1988, 1997; Schowalter, 1979; Wollenweber et al., 2010). Numerous studies have shown that the matrix permeability of shale is inherently low, sensitive to changes in pore pressure and effective stress, and highly anisotropic compared to that of a classical reservoir rock such as sandstone or carbonate (Chalmers et al., 2012b; Chenevert and Sharma, 1993; Ghanizadeh et al., 2013, 2014a,b). Pressure driven gas transport in the shale matrix is dominated by laminar (Darcy) flow and slip flow. At low pressures, slip flow dominates because the mean free path length is longer or within the similar scale in comparison to the scale of the micropores and fracture network of the shale matrix. At high pressures, where the mean free path length is smaller than pore throat sizes, Darcy flow is dominant. The Knudson number, which describes the ratio of mean free path length to pore throat size, is used to differentiate the different flow regimes (Tables 7 and 8).

Mineralogy also effects matrix permeability. The matrix permeability decrease significantly with increasing clay content (Ghanizadeh et al., 2013, 2014b; Kwon et al., 2004; Yang and Aplin, 2010). In contrast, a high quartz content can increase the permeability significantly and superimposing the effect of permeability reducing caused by clay contents up to 30% (Heller et al., 2014).

Permeability of organic-rich shales is not solely controlled by mineralogy, as high permeability coefficients are encountered equally for quartz-, carbonate- and clay-rich lithotypes. It is rather a combination of mineralogy, rock fabric and pore size distribution that appears to control the matrix permeability of these lithotypes (Chalmers et al., 2012a,b).

Matrix permeability also depends indirectly on temperature because as temperature increases, the compressibility strength of the rock decreases. Faulkner and Rutter (2000) have shown that permeability decreases slightly when temperature is increased by a factor of 2 to 3. Furthermore, they showed that this change is correlated to temperature-induced compaction of stress-confined samples (293 K < T < 423 K).

Slip flow

The degree of slip flow (as denoted by the Knudsen number) in low-permeability sedimentary rocks depends on rock pore throat size and the mean free path of the gas molecules (Javadpour et al., 2007; Javadpour, 2009). Slip flow becomes more significant as pore throat size decreases. In particular, slip flow is more dominant in shales, which are typically characterized by pore throats tens of nanometers in size (Fig. 8), than in coals. Temperature, pressure, and the "collision diameter" of the permeating gas molecules also affect the mean free path of the gases, and therefore, the degree of slip flow (Tables 7 and 8).

At pressures encountered in conventional reservoirs, relatively large pore throats ensure that the apparent permeability is very close to the absolute permeability. This results in negligible slippage effect. In contrast, in unconventional reservoirs the pore throats are in the micrometer range and below, and slippage becomes more important (Bustin et al., 2008). As discussed before in detail, the magnitude of the slip-flow effect in shale gas reser-

Table 7
Mean free path lengths of gases calculated for atmospheric pressure (0.112 MPa) and experimental temperature (308 K) using Eq. (11). The atomic/molecular diameters were taken from (a) Halpern and Glendening (1996)) and (b) Hirschfelder et al. (1954).

Gas	Atomic/molecular diameter (nm) (a)	Mean free path length (nm) (a)	Atomic/molecular diameter (nm) (b)	Mean free path length (nm) (b)
He	0.287	103.7	0.265	122.7
Ar	0.389	56.5	0.398	54.1
N_2	0.419	48.6	0.405	52.2
CH_4	0.425	47.3	0.429	46.5
CO_2	0.443	43.6	0.436	45.0

Table 8
A summary of the different flow regimes, their attributed Knudson numbers, and the related driving force. Assumes laboratory conditions (T = 300 K and 5 MPa); pore size classification according to IUPAC (micro-pores < 2 nm, 2 nm < meso-pores < 50 nm, 50 nm < macro-pores).

Flow regime	Knudson number	Driving force	Pore network
Free molecular flow	Kn > 10	Free molecular flow, where collisions between particles can be neglected and the flow is dominated by wall/particle interactions	Micro
Transition region	0.1 < Kn < 10	The transition flow regime, where the Navier–Stokes–Fourier equation is not valid; gas flow is better described by the Boltzmann equation. Molecular diffusion, molecule-wall interactions (slip flow) begin to affect flow	Micro–Meso
Slip flow	0.001 < Kn < 0.1	The slip-flow regime, where the Navier–Stokes-Fourier equation is still valid, but the boundary conditions for the mathematical solutions contains a velocity slip and temperature jumps at the gas-well interface Reduced viscosity, molecule-wall interactions dominate	Meso
Continuum/Darcy /Hagen–Poiseuille flow	Kn < 0.001	The hydrodynamic regime, where the Navier–Stokes equation Fourier equation can be applied successfully Laminar flow, driven by pressure gradient	Macro

voirs depends on pore throat size, the density of micro-fractures, and the pore pressure. Fathi et al. (2012) used Lattice Boltzmann simulations to show that a significant slip-effect can be expected for pressures up to 3 MPa for capillaries of 10 nm radius.

The typical diameter of a pore throat in a shale, particularly within the organic matrix, is so small (1 nm < d < 100 nm: Sakhaee-Pour and Bryant (2012)) that the thickness of the sorbed gas layer might become an important control on the mechanisms of fluid transport within the matrix (Akkutlu and Fathi, 2011). Sakhaee-Pour and Bryant (2012) analyzed the effects of adsorbed layers of methane (CH_4) and of gas slippage at pore walls on the flow behavior. They found that the reduction of micro-pore throat diameters by the adsorbed layer at reservoir conditions can be significant, particularly because both are almost on the same scale. Recent molecular-dynamics simulations of methane flow through nanoscale kaolinite channels have shown that the gas molecules accumulate near the kaolinite wall, reducing the size of the gas flow path in tight, porous media (Niu et al., 2014). However, other numerical simulations have shown that under laboratory conditions (P < 5 MPa, T = 30 °C) the thickness of the sorbed gas (CH_4) layer is so small that it has a negligible effect on permeability (Sakhaee-Pour and Bryant, 2012).

Many authors have investigated experimentally the slip flow or Klinkenberg effect (Gensterblum et al., 2011b,c, 2012, 2014; Ghanizadeh et al., 2013, 2014a,b; Heller et al., 2014; Sinha et al., 2013, 2012). Laboratory flow experiments are usually done at lower pressures than those present in typical gas reservoirs. This is not optimal, because the slippage effect is significant and is potentially interfering with poroelastic properties and needs to be considered when extending laboratory results to the reservoir (Ghanizadeh et al., 2013, 2014a,b; Tinni et al., 2012). We will discuss the challenges of measuring flow attributes and processes in the laboratory and extending them to the reservoir in detail later in this review.

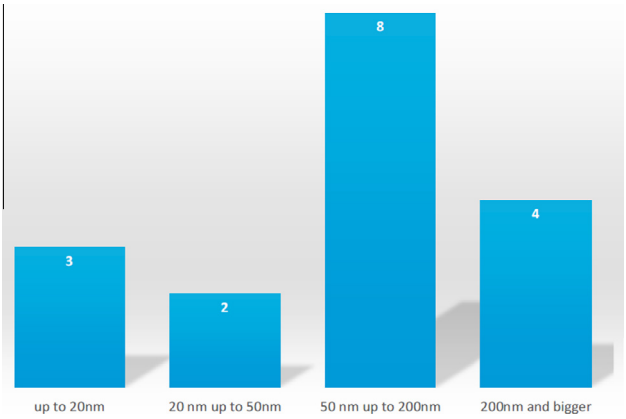

Fig. 8. The statistical distribution of pore throat size, calculated from slippage factors obtained from 17 different shales. Data compiled by Ghanizadeh et al. (2013, 2014a,b), Heller et al. (2014), Sinha et al. (2013). Following the IUPAC classification most of this shales contain an apparent meso-porous to macro-porous transport network.

Typically, slip flow (or Klinkenberg) corrected gas permeability values are higher than liquid permeability coefficients. This has been demonstrated by many researchers (Faulkner and Rutter, 2000; Ghanizadeh et al., 2013, 2014a,b; Pazos et al., 2009; Tanikawa and Shimamoto, 2009a,b). This factor between both fluids range from 20 up to 150 (Ghanizadeh et al., 2014a,b). This factor depends mainly on gas type and effective stress and type/content of clays. However the dominating influence has the gas type where methane shows much lower factors (20–50) than helium (up to 150) and the variation caused by stress sensitivity are minor.

A few authors have reported a deviation from Klinkenberg's straight-line relationship, especially in low-permeable cores (Ashrafi Moghadam and Chalaturnyk, 2014; Fathi et al., 2012; Tinni et al., 2012). Fathi et al. (2012) performed Lattice-Boltzmann simulations of fluid dynamics, illustrated a deviation from the linear trend, and proposed a more accurate empirical quadratic equation. Fathi and his coworkers concluded that the differences are related to the kinetic interactions between gas molecules that have gone through inelastic collisions with the capillary walls and those molecules that make up the bulk fluid within the capillary. Despite these findings, the majority of laboratory results didn't show significant discrepancies to the original Klinkenberg relationship.

Finally, the validity of the slip-flow concept is illustrated in Fig. 9. We are able to show that the proposed correlation of equation (9) is valid within an error band of 20%. However, this error band includes other counteracting effects – for instance, the effects of the thickness of the adsorbed layer or small effective stress variations. The latter effect occurs because the slippage factor is a function of effective stress.

Measurements made to obtain the intrinsic permeability coefficient of shales are complex because shales have higher compressibility and a meso-pore size distribution – properties that results in a complex interplay between processes such as slip flow and poro elastic effects. The comparability between different studies is limited, because many experiments completed to date have not demonstrated sufficient reproducibility. In addition, it can take up to two weeks for a shale sample to become or that the stress-equilibrated, a much longer time than is typically allowed for laboratory experiments (Gensterblum et al., 2014; McKernan et al., 2014a). These factors combined mean that additional high quality permeability experiments are necessary.

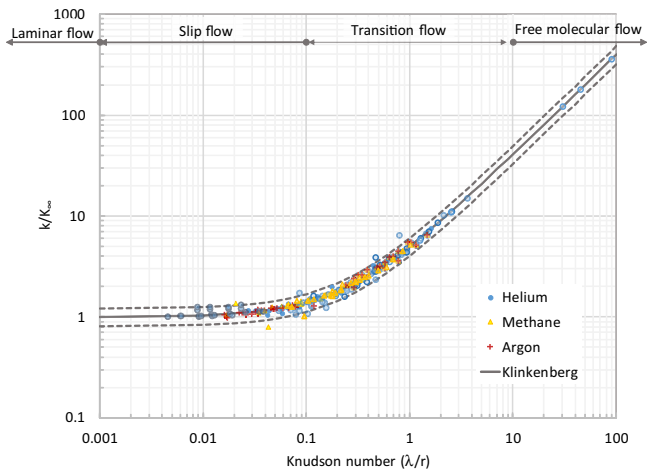

Fig. 9. The deviation of permeability from Darcy flow as a function of Knudsen number. The solid line represents the ratio predicted by the Klinkenberg model (Eq. (12)); the dashed lines represent a 20% deviation from the model. Data are taken from Ghanizadeh et al. (2013, 2014a,b), Heller et al. (2014), Sinha et al. (2013). Circles represent helium measurements and triangles indicate methane measurements. The deviation is attributed to the coupling of poroelasticity and the slip flow effect. Extrapolations to lower temperatures derived from the data set of Sinha et al. (2013) fall within the 20% deviation range.

Stress dependence of permeability

Because porous media deform under stress, permeability is a function of effective stress. Changes in the permeability of shale under isotropic stress conditions has been widely reported, and many researchers have shown that the permeability of shale decreases with externally applied stress (Chenevert and Sharma, 1993; Ghanizadeh et al., 2013, 2014a,b; Heller et al., 2014; Tinni et al., 2012) (Fig. 10).

A range of non-linear correlation functions have been used to describe these observations mathematically. Most prominent are the exponential and power laws:

$$k(\sigma_{\text{eff}}) = k_0 e^{-c_m \sigma_{\text{eff}}} \tag{16}$$

where the permeability in the absence of effective stress is k_0 and the stress sensitivity (pore throat compressibility) within the shale matrix is c_m (Fig. 11). The intrinsic permeability k_0 depends on the textural and lithological parameters that affect the extent, pore size distribution, and connectivity of pore space in the rock. The stress sensitivity coefficient can be simplified to the pore throat compressibility when the change of tortuosity and connectivity with effective stress is negligible.

$$k(\sigma_{\text{eff}}) = \mathrm{A}\sigma_{\text{eff}}^{-B} \tag{17}$$

The power law (Eq. (17)) provides a very good fit to the experimental permeability data. However, it has a serious mathematical disadvantage when the effective stress approaches zero – in that case, the permeability approaches infinity, which makes use of the equation in very low stress conditions impractical and inaccurate.

A third equation used to describe changes in permeability is a modified cubic law (Eq. (18)). It has been applied by several authors to calculate matrix permeability in organic-rich shales.

$$k(p_{\text{eff}}) = \mathrm{k}_0 \left(1 - \left(\frac{p_{\text{eff}}}{p1}\right)^m\right)^3 \tag{18}$$

The permeability in absence of effective stress is K_0. The parameters m and $p1$ are associated with the geometry of the pore throats and the effective pressure. The fitting parameter m is related to the asperity height distribution and may take values between 0 and 1 (Gangi, 1978). Thus, this equation can take into account fracture flow properties.

Effective stress law. Many efforts have been made to describe the relationship between permeability and effective stress (Kwon et al., 2001, 2004). Observations show us that the transport properties for a variety of rock types exhibit sensitivity to pore pressure and confining pressure.

Kwon et al. (2001) and Heller et al. (2014) have shown that the effective stress law can be applied to shales successfully. Kwon and

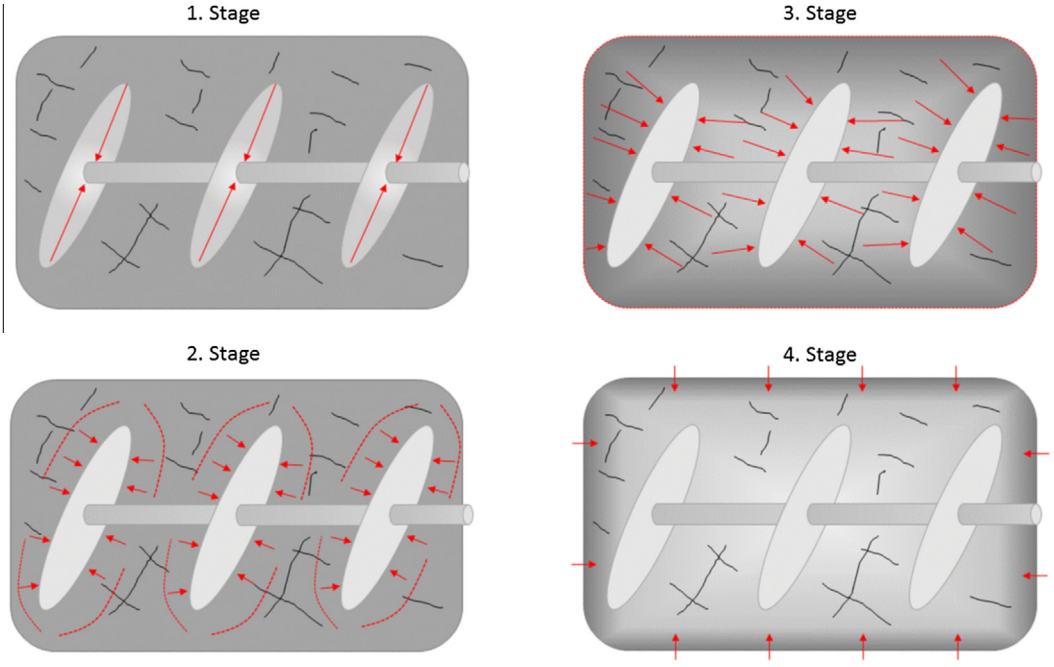

Fig. 10. A common brief interpretation of the transport processes occurring during depletion of an unconventional reservoir (modified after Clarkson and Williams-Kovacs, 2013). The stimulated rock volume is outlined in gray, hydraulic fractures are elliptic light gray area, and the horizontal well is illustrated as a gray horizontal cylinder. The pressure or concentration isolines are shown in dotted red lines. The red arrows illustrate the main flow orientation and origin. (For interpretation of the references to colour in this figure legend, the reader is referred to the web version of this article.)

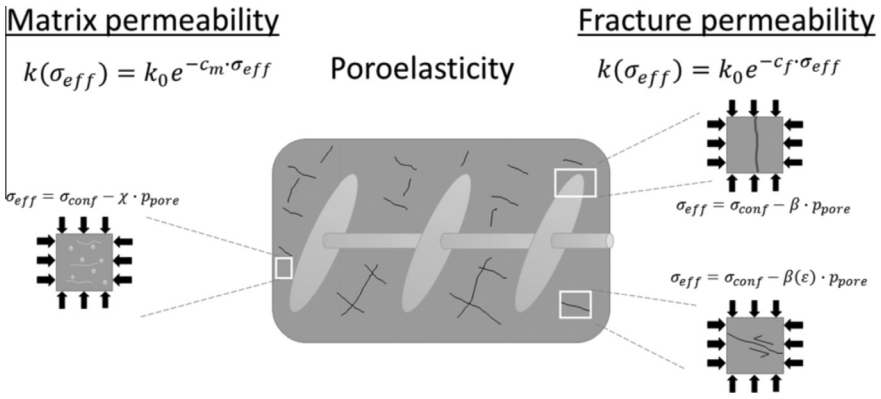

Fig. 11. Types of fractures in a hydraulic fractured shale. The stimulated rock volume is outlined in gray, hydraulic fractures are elliptic light gray area, and the horizontal well is illustrated as a gray horizontal cylinder.

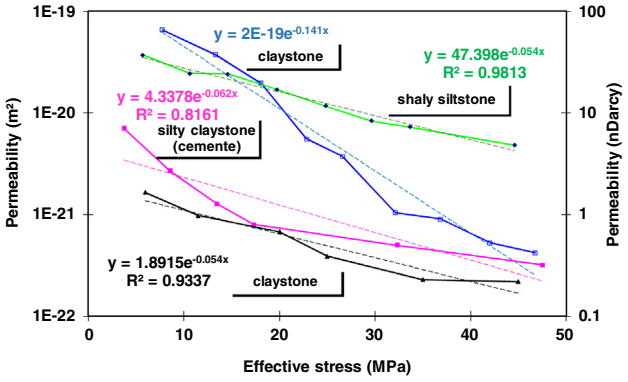

Fig. 12. Matrix permeability as a function of normal effective stress for different lithotypes (data points are taken from Schloemer and Krooss, 1998).

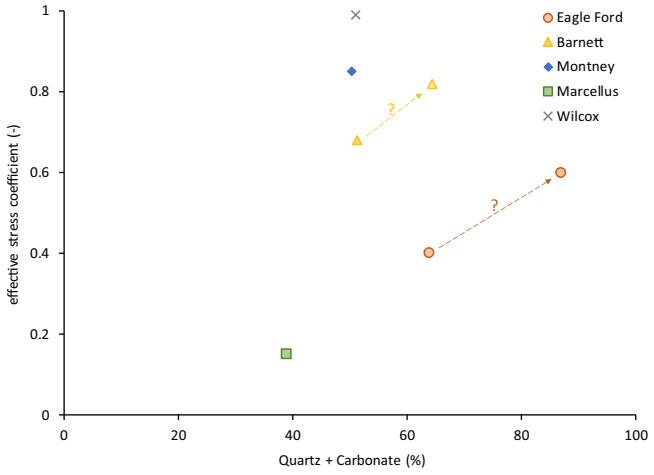

Fig. 13. The effective stress coefficient plotted as a function of percentage of relatively incompressible grains, such as quartz and carbonates (data taken from Heller et al. (2014) and (Kwon et al., 2001)). No general correlation can be observed, but possible intrabasinal correlation is weakly suggested by samples from the Barnett and Eagle Ford formation.

his co-workers found an effective stress coefficient (X) close to 1 in very weak, high-clay Wilcox shale samples from the Gulf of Mexico. In contrast, Heller et al. (2014) found X coefficients below 1 for samples from Eagle Ford, Barnett, Marcellus, and Montney shale formations (Fig. 12).

No interbasin relationship has been found between the proportion of relatively incompressible mineral components such as quartz and clay and the effective stress coefficient (Fig. 13). However, it is likely that a correlation exists within a single basin, as demonstrated by the positive trend within the Barnett and Eagle Ford sample sets (arrows in Fig. 13). More measurements are required to draw conclusions about these correlations. A summary of the results of multiple studies of the relationship between permeability and stress is given in Table 9.

Stress sensitivity of permeability. Tinni et al. (2012) have investigated the relationship between permeability and effective stress (Table 9). They found that the permeability of the Devonian shale plugs showed a high sensitivity to changes in effective stress. Over the range of confining pressured studied, permeability decreased by up to three orders of magnitude. They concluded that this sensitivity was due to cracks within the shale matrix.

Schloemer and Krooss (1995) and Ghanizadeh and his coworkers (2013, 2014a,b) performed comprehensive studies investigating the dependency of effective stress on gas composition. Unfortunately, neither study was carried out under sufficiently high pore pressure to disentangle the influences of slip-flow and poroelastic effects on the apparent permeability.

In general, under stress-free conditions, the effective stress law only affects the permeability k_0 – it does not affect the stress sensitivity coefficient.

Table 9 contains a compilation of published permeability studies, and Fig. 14 illustrates the statistical distribution of stress sensitivity coefficient. The majority of the pore throat compressibility coefficients are low (up to 0.05 MPa^{-1}). Fig. 15 shows the stress sensitivity as a function of the shale components. Fig. 15 shows no simple correlation between stress sensitivity and the prevalence of incompressible minerals (quartz and calcite), clays, or TOC content. This is probably because the transport processes operating at the pore throats are different for clay- and quartz-rich shales and those with micro-fractures (Table 10).

Many of the studies listed in Figs. 14 and 15 did not take coupling between slip flow and poroelastic processes (discussed below) into account in their experimental design, limiting their reliability for correlation work.

Porosity, permeability and effective stress relationships

Small changes in porosity caused by changes in effective stress are related to large changes in permeability. This follows from the consideration of a capillary bundle model, which uses the Hagen–

Table 9
Summary of published permeability measurements as a function of effective stress. The pore throat compressibility coefficient is not affected by the effective stress coefficient, but the zero stress permeability value is affected by the choice of the effective stress coefficient (* indicates that the effective stress coefficient is assumed to be 1). Rich = conc.>30%: p.d.p = pulse-decay permeameter.

Source	Location	Sample description	Pore pressure (MPa)	Confining pressure (MPa)	Eff. stress coef. (−)	Eff. stress (MPa)	Apparent perm. (mD)	Stress sensitivity ceff. (MPa^{-1})	Zero stress perm. (mD)	Slip factor (MPa)	Slip-flow corrected perm (mD)
Kwon et al. (2001)	Wilcox shale	Low Clay and high clay contents	10–42	13–45	1*	3–12	2×10^{-4}–3×10^{-6}	0.491–0.289	1×10^{-3}–3×10^{-4}	n.d.	n.d.
Heller et al. (2014)	Marcellus	Quartz and Clay rich	1.7–20.7	8–50	0.15	8–45	2×10^{-4}–2×10^{-5}	0.045–0.030	1×10^{-4}–8×10^{-5}	2.1–2.7	$67–33 \times 10^{-6}$
	Eagle Ford 174	Clay + TOC rich	1.7–20.7	8–50	0.4	8–45	8×10^{-5}–3×10^{-6}	0.051–0.095	1×10^{-4}–5 10^{-5}	1.8–3.4	$33–10 \times 10^{-6}$
	Eagle Ford 127	Carbonate rich	1.7–20.7	8–50	0.6	8–45	8×10^{-2}–3×10^{-3}	0.019–0.024	1.5×10^{-2}–2.1×10^{-2}	1.35–1.42	$9–6 \times 10^{-3}$
	Barnett 31	Quartz and Clay rich	1.7–20.7	8–50	0.68	8–45	1 10^{-4}–6 10^{-6}	0.031–0.034	1.9×10^{-4}–2.1×10^{-4}	n.d.	n.d.
	Barnett 27	Quartz and Carbonates rich	1.7–20.7	8–50	0.82	8–45	1×10^{-2}–6×10^{-3}	0.032–0.036	2.2×10^{-3}–2.4×10^{-3}	n.d.	n.d.
	Montney	Quartz and Carbonates rich	1.7–20.7	8–50	0.85	8–45	1×10^{-2}–6×10^{-3}	0.026–0.032	1.7×10^{-2}–1.9×10^{-2}	n.d.	n.d.
Ghanizadeh et al. 2013, 2014b	Posidonia shale (Wickensen)	Immature, Clay, Quartz Carbonate		12–30						3.1–4.2 (He)	$48 \pm 3 \times 10^{-6}$ $38 \pm 2 \times 10^{-6}$ (He)
	(Haddessen)	Over-mature		12–30				0.041–0.015	$7–3 \times 10^{-5}$	2.8–3.7	$2.3 \pm 0.2 \times 10^{-6}$ $1.6 \pm 0.1 \times 10^{-6}$
Cho et al. (2013)	Bakken		1.7	7–35	1	5–33	1.3×10^{-3}–3×10^{-4}	0.078–0.121	$1–3 \times 10^{-3}$	n.d.	n.d.
Armitage et al. (2011)	Krechba Field Algeria	Horizontal	20	31–85	1	11–65	5×10^{-3}–6×10^{-6}	0.014–0.029		n.d.	n.d.
	Krechba Field Algeria	Vertical	20	31–85	1	11–65	5×10^{-5}–6×10^{-8}	0.014–0.029		n.d.	n.d.
Mokhtari et al. (2013)	Eagle Ford	Calcite rich	n.r.	n.r.	1*	6–12		0.132–0.343	1×10^{-3}	n.d.	n.d
	Mancos	Quartz rich	n.r.	n.r.	1*	7–24		0.036–0.111	4×10^{-3}	n.d.	n.d
Tinni et al. (2012)	Unknown	Ordovician	0.69	7–35	1*	6–34	10^{-6}	0.25–0.07	$1.2–1 \times 10^{-4}$	n.d.	n.d
	Unknown	Devonian	0.69	7–35	1∗	6–34	10^{-6}	0.28–0.03	10^{-2}–10^{-4}	n.d.	n.d
McKernan et al. (2014b)	Whitby Mudstone formation	Toarcian	23–27	35–95	1∗	8–72		0.029–0.034	4.1×10^{-4}–3.6×10^{-6}	n.d.	n.d
Chalmers et al. (2012a);	Evie (Horn River basin)		p.d.p	n.r.	1∗	13–42		0.001–0.179	8×10^{-2}–7×10^{-7}	n.d.	n.d
	Muskwa (Horn River basin)		p.d.p	n.r.	1∗	14–41		0.038–0.147	6×10^{-2}–4.8×10^{-5}	n.d.	n.d
	Otter Park (Horn River basin)		p.d.p	n.r.	1∗	14–41		0.118	0.42	n.d.	n.d
	Besa River (Liard basin)		p.d.p	n.r.	1∗	14–41		0.011–0.049	9.5×10^{-5}–3×10^{-6}	n.d.	n.d
Sinha et al. (2013)								n.d.	n.d.		2.3×10^{-3}–5×10^{-6}
Clennell et al. (1999)		Kaolinite, natural clay	$P > 0.3$	n.r.	1∗	0.02–3.5	10^{-4}–10^{-7}			n.d.	n.d

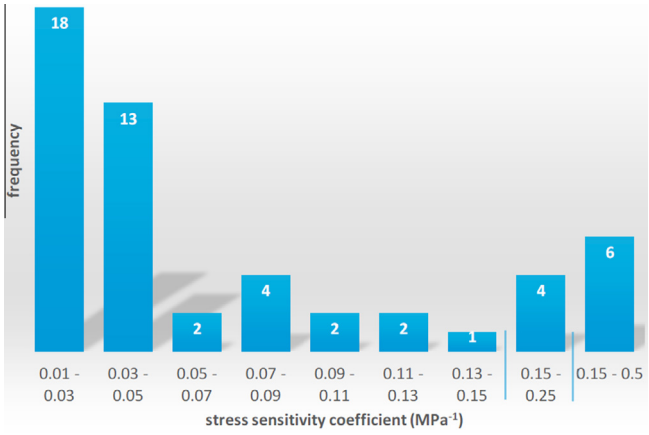

Fig. 14. The statistical distribution of the pore throat compressibility factor for 52 samples. A majority of the shale samples have a low pore throat compressibility and/or low stress sensitivity.

Poiseuille law to describe fluid flow. In this model, the radius of a pore throat is proportional to the 4th square root of pressure. From the model, it can be concluded that increases in effective stress affect permeability more than porosity. This disproportionality gets more pronounced considering a more realistic porous system containing bottle necks and cavities in the pore network. In coals and shales, a micro-fracture-based model might be more realistic.

Permeability stress hysteresis

McKernan et al. (2014b) observed a stress equilibration phase at the beginning of each experiment. After the stress equilibration period, no permeability differences were observed between the pressure loading and pressure unloading cycle.

In addition, no stress-perm hysteresis between loading and unloading cycle could be observed after the equilibration period (Ghanizadeh et al., 2014a; McKernan et al., 2014b).

Effect of moisture on the permeability. The degree of water saturation in organic-rich shales varies with lithology and organic carbon content. The most important control on water saturation, however, is the extent of past hydrocarbon generation, which leads to water expulsion. Some shale formations contain less water than the amount required to achieve equilibrium. This condition is referred to as sub-irreducible water saturation (Gupta, 2011).

The sorption capacity of water in shale is controlled by the amounts and types of organic materials and clays. Adsorbed moisture has the effect of reducing the shale matrix permeability. In addition, the presence of water in pore throats increases the stress sensitivity of matrix permeability (Ghanizadeh et al., 2013, 2014a).

Obviously, the permeability difference between methane and helium is smaller when water is adsorbed on the surface (Ghanizadeh et al., 2013, 2014a).

We propose a concept to explain the reduction in permeability and the higher stress sensitivity associated with the presence of water in the pore network. The concept, illustrated in Fig. 16, is

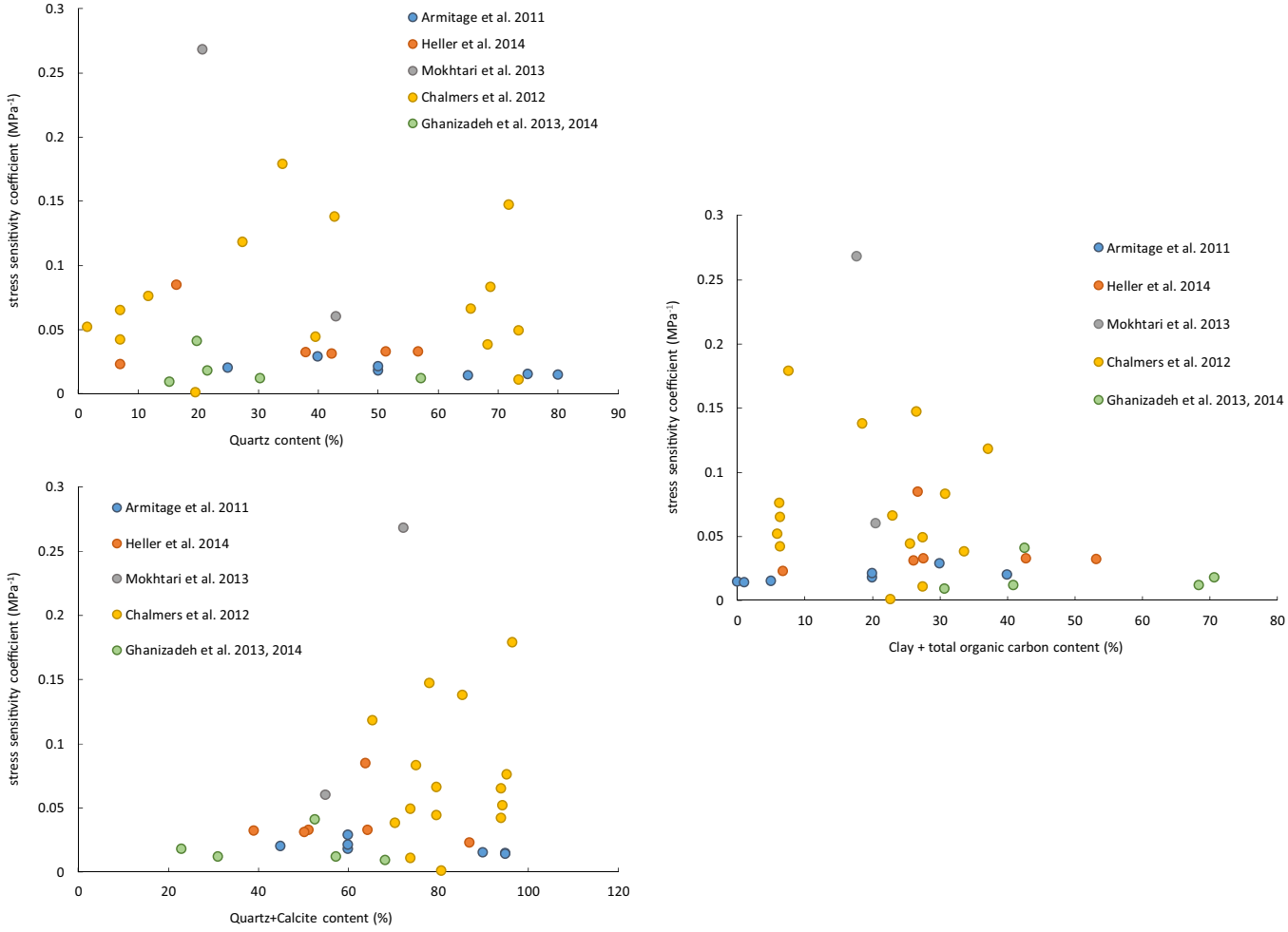

Fig. 15. Pore throat compressibility or the stress sensitivity factor as a function of shale mineralogy. We classify shale composition into two categories: (1) clays and total organic carbon, which have a higher compressibility, and (2) quartz or calcite, which have a low compressibility.

Table 10
Summary of selected published permeability measurements made on granite and sandstone as a function of effective stress. The pore throat compressibility coefficient is not affected by the effective stress coefficient, but the zero stress permeability value is affected by the choice of the effective stress coefficient.

Source	Location	Sample description	Pore pressure (MPa)	Confining pressure (MPa)	Eff. Stress coef. (−)	Eff. Stress (MPa)	Apparent perm. (mD)	Stress sensitivity ceff. (MPa^{-1})	Zero stress perm. (mD)	Slip. factor (MPa)	Slip-flow corrected perm (mD)
Gensterblum et al. (2014)	Surat basin, Taroom	Sub-bituminous Coals	0.1–0.5	7–15	1	6–14	5.8	0.165	5.8	0.04–0.6	0.8–1.5
Bernabe (1987)	Pottsville	Sandstone	10–30	20–140	0.85	10–100	10^{-4} 10^{-6}	0.014 ± 0.001	1.0×10^{-4}	n.d.	n.d.
	Pigeon Cove	Granite	10–30	20–140	0.82	10–100	10^{-4} 10^{-6}	0.016 ± 0.001	1.0×10^{-4}	n.d.	n.d.
	Westerly	Granite	10–30	20–140	0.67	10–100	10^{-4} 10^{-6}	0.038 ± 0.002	9.1×10^{-6}	n.d.	n.d.

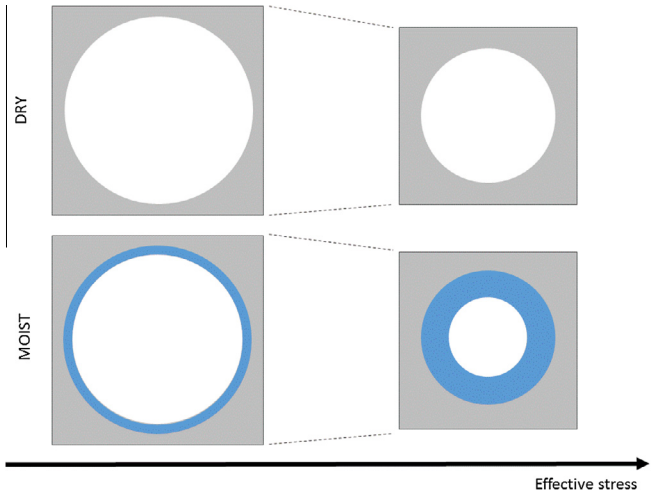

Fig. 16. Illustration of the proposed mechanism by which permeability is more sensitive to effective stress in a moisturized shale than it is in a moisture-free shale. The blue circle represents a water layer. The left side of the figure shows a dry and moist pore under conditions of low effective stress. As stress increases, the pore radius decreases, as shown on the right side of the figure. Because the volume of water lining the pores is constant, the water layer becomes thicker as the pores become smaller in diameter. The presence of a thick water layer in the pore throat decreases permeability. This mechanism requires elastic deformation and conservation of water volume in the pores. (For interpretation of the references to colour in this figure legend, the reader is referred to the web version of this article.)

based on two assumptions: (1) the deformation of the porous medium is elastic in nature, and (2) the water is located at least partly at the walls of the pore throats, is constant in volume, and is not mobile.

When the pore radius is reduced by increasing effective stress, the water layer needs to adjust as well (Fig. 16). As pore radius decreases, the water layer increases in thickness. Since the water volume is constant, this must lead to a reduction in the effective pore throat radius (Fig. 16). By this mechanism, a given increase in effective stress reduce permeability to a greater extent in a wet pore network than in a dry pore network. The mechanical strength of shales may significantly depend on water content. It has been reported that loss of 2.1% (wt) water from a clay-rich shale increased shale mechanical strength by 30% (Ibanez and Kronenberg, 1993).

Effect of permeating fluid. The intrinsic permeability coefficient is a specific material property of a porous medium. Therefore, the coefficient should be independent of the fluid (gas or liquid) used for its determination (Civan, 2010; Civan et al., 2011, 2012). However, in the published experiments reviewed here, which consider coals and organic-rich shales containing helium, argon and methane (Gensterblum et al., 2011a, 2014; Ghanizadeh et al., 2013, 2014a, b; Han et al., 2010; Pan et al., 2010; Sinha et al., 2013), measured permeability coefficients differ depending on the type of gas used, even after slip flow correction (Fig. 17 and Table 11). The permeability coefficients tend to be ordered as follows, based on the type of gas used: $k_{helium} > k_{argon} \geqslant k_{nitrogen} \geqslant k_{methane} > k_{carbon\ dioxide}$ (Gensterblum et al., 2014; Ghanizadeh et al., 2013, 2014a,b; Sinha et al., 2013).

The dependence of the "intrinsic" permeability coefficient on gas type could be the result of several factors: (i) differences in the interaction of gas molecules with the pore surface due to differences in water presence, (ii) differences in fluid-dynamic properties, such as viscosity, that are "amplified" by transport through a tortuous pore system, (iii) differences in "effective tortuosity" (size exclusion) between gases, (iv) swelling-induced micro-cleats (Hol et al., 2012), (v) the reduction of the nano scale pore throat diameter by adsorption (Fathi et al., 2012) because the expected thickness of the adsorbed layer associated with each gas would match with the sequence of experimentally observed coefficient values listed above), and (vi) changes in pore throat diameter caused by swelling of each individual organic component or clay particle. Finally, (vii) the classical Darcy equation, which is derived using the ideal gas law, may have a reduced validity for non-ideal gases like N_2, CH_4, and, especially, CO_2.

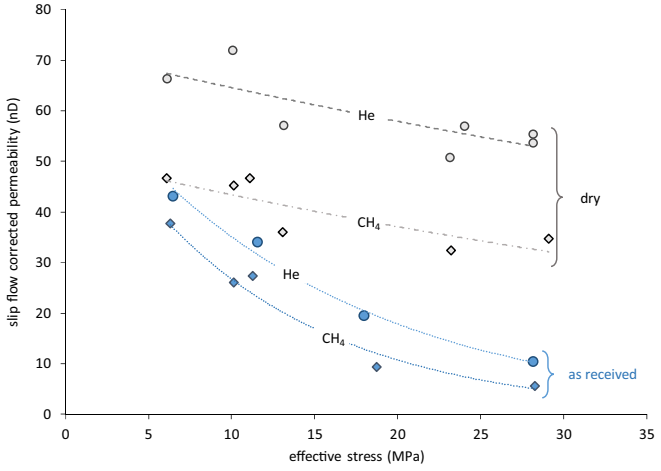

Fig. 17. Slip flow corrected Klinkenberg permeability as a function of effective stress. Permeability (He, CH_4) measured parallel to bedding on the plug Alum#2 (V_{Rr} = 2.4%, TOC = 7.1%). Note the difference in the sensitivity of permeability to effective stress between a dried sample (105C under vacuum for 14 h) and a sample 'as received' (containing moisture) (Ghanizadeh et al., 2014a).The slip flow corrected permeability k_∞ (He, CH_4) decreased by up to 20% when effective stress was increased from 5–30 MPa.

Table 11
Pore throat compressibility and the zero-stress permeability determined on a plug for different moisture contents (Ghanizadeh et al., 2014a).

	Pore throat compressibility C_m		Zero-stress permeability k_0	
	(MPa^{-1})	±	(nD)	±
Helium				
Dry	0.018	0.008	78	17
Moist (1.1 wt%)	0.068	0.004	69	11
Methane				
Dry	0.016	0.005	51	9
Moist (1.1 wt%)	0.091	0.010	67	23

Because surface area tends to increase exponentially as pore (grain) size decreases, fine-grained mudstones and shales, in which micro- and meso-scale pores dominate, contain substantial surface area for gas sorption (Cui et al., 2009). Compared to tight gas sandstones, organic-rich shales have substantially greater gas sorption capacities (Cui et al., 2009). Based on the experimental observations of Gasparik et al. (2012), clay minerals can contribute significantly to the methane sorption capacity of shales. The occupation of pore throat volume by interlayer sorbed gas could affect the surface area of the connected pore throat volume, and in consequence, the permeability. Furthermore, layers of sorbed gas molecules within the pores of organic-rich shales reduces the cross section of the pore throats and therefore reduces the fluid transport through the shale matrix (Wang et al., 2009). Experimental results suggest that, for organic-rich shales with TOC contents ranging between 1.8% and 14.2%, the ratio between helium and methane permeability coefficients (effective stress of 30 MPa, Klinkenberg-corrected) increases with increasing TOC content (Fig. 18) (Ghanizadeh et al., 2013). In contrast, increases in TOC content had no significant effect on the ratio between helium and argon permeability coefficients (effective stress of 30 MPa, Klinkenberg-corrected) (Ghanizadeh et al., 2013). Ghanizadeh et al. (2013) show that the ratio between Helium and methane permeability coefficients does not change significantly under changing effective stress conditions. This observation suggest that swelling of the total organic material (TOC) reduces the permeability by either reducing the pore throat diameter or increasing the tortuosity. However, based on the numerical simulations by Sakhaee-pour and Bryant (2012), the effect of sorbed gas layer on shale permeability could become significant under field conditions ($P > 10$ MPa, $T = 90$ °C). It was assumed in these simulations that the thickness of a sorbed layer of methane molecules is constant (0.7 nm) at a pore pressure of 28 MPa and decreases linearly with pressure (Sakhaee-Pour et al., 2011).

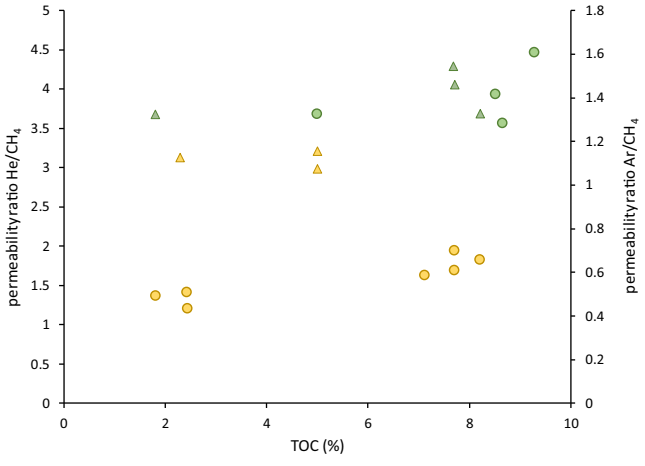

Fig. 18. The ratio of helium permeability coefficients to methane and those of argon to methane for samples differing in total organic carbon (TOC) content. Data set compiled from Ghanizadeh et al. (2013) and Sinha et al. (2013). Permeability coefficients from Ghanizadeh et al. (2013) are Klinkenberg-corrected and were measured at an effective stressof 30 MPa. It can be concluded that the observed permeability ratio is not likely controlled by the TOC content. Considering coal permeability studies (Gensterblum et al., 2014) yielding ratios around ~1 with TOC around 80%, it becomes more evident that interactions between gas and TOC are not likely the reason for the observed differences.

Effect of pore pressure on the stress sensitivity

Observations such as in Fig. 19 have shown that stress sensitivity is affected by mean pore pressure (Heller et al. (2014)). Gensterblum et al. (2014) investigated potential causes for this relationship and concluded that it is caused by the coupling of slip flow and poroelastic deformation. Slip flow is usually not explicitly considered in the evaluation and application of pore throat compressibility (c_m). This is probably due to the implicit assumption that the contribution of slip-flow to total flow can be minimized by performing the permeability tests at high mean gas pressures. However, in experiments and field tests, situations may occur where slip flow plays a role due to conditions where mean free path length and pore throat radius are in the same order of magni-

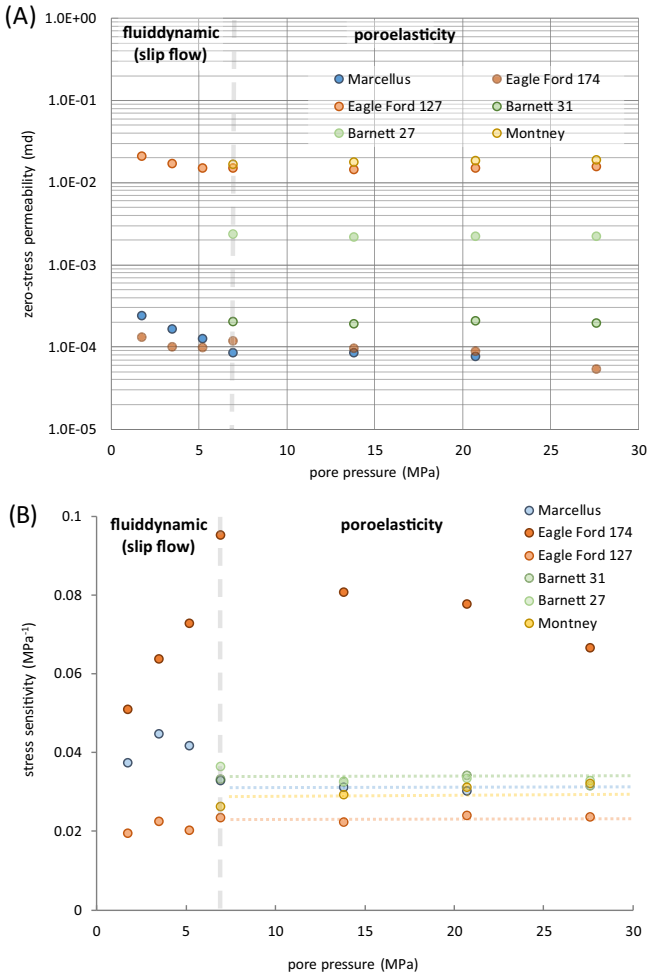

Fig. 19. Pore throat compressibility as a function of mean pore pressure measured with helium (data for this evaluation are taken from Heller et al. (2014)). The pore compressibility coefficient fluctuates up to pressure of 8 MPa. At higher pressures, the pore throat compressibility is constant and independent of pore pressure, as postulated for an intrinsic rock property. This is because the interfering contributions of the Klinkenberg effect are negligible.

tude. As illustrated in Fig. 19, for certain pore throat radius distribution small poroelastic changes in pore radius result in significant changes in the slip-flow component. This coupling of fluid-dynamic and poroelastic effects may affect permeability evolution during reservoir depletion. Fig. 20 show the mean free path length and the pore radius distributions for shales with meso- (Fig. 20, top, Case 1) and micro-pore throat distribution (Fig. 20, bottom, Case 2). The solid lines represent the distributions at reservoir pressure ($p_{reservoir}$), while the dotted lines represent the distributions at a strongly reduced pore pressure (p_1). As gas pressure decreases, the mean free path length increases and the pore throat radius decreases, due to an increase in effective stress (the reservoir formation (confining) stress is assumed to be constant during reservoir depletion). As illustrated in Fig. 20, the overlap between mean free path length and pore throat radius increases during production. For the shale sample in Case 1, which has a meso-pore throat distribution, this overlap is negligible and no positive contributions of slip flow can be observed. However, for a sample with a large number of micro-pore throats (Case 2), the increasing intensity of slip flow contributes significantly to the permeability.

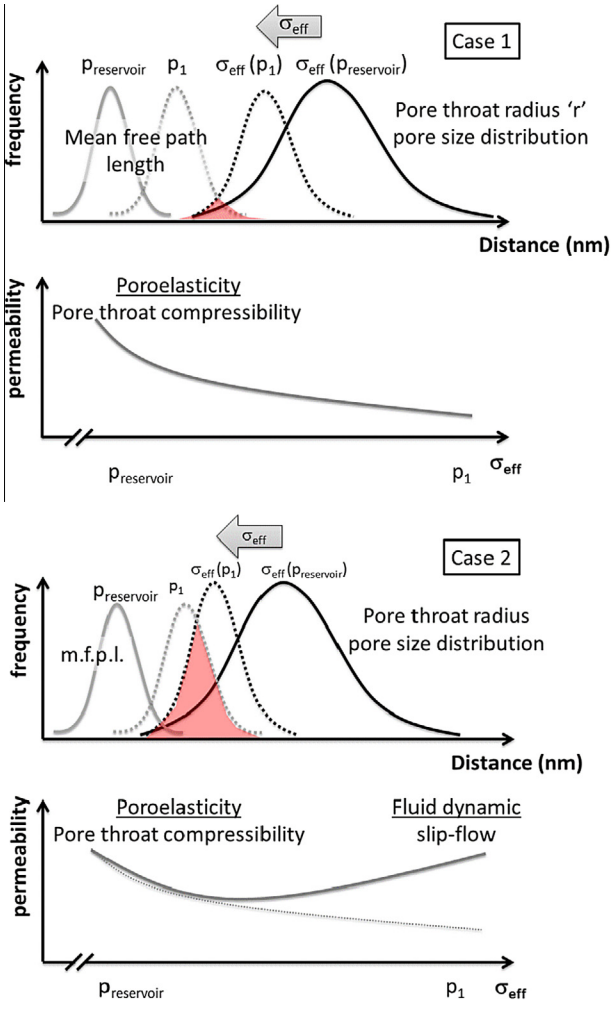

Fig. 20. Schematic illustration of coupling between poroelasticity and fluid dynamics in highly compressible porous media. The frequency distribution of the mean free path length (m.f.p.l.) is shown in gray; the pore throat radius is shown in black. The solid line illustrates the conditions at initial reservoir pressure and the dotted line represents the conditions during production (decreasing pore pressure, corresponding to increasing effective stress). Where both distributions overlap (red area), a significant slip flow contribution can be expected (cf. Case 2) (Gensterblum et al., 2014). (For interpretation of the references to colour in this figure legend, the reader is referred to the web version of this article.)

$$k_{app} = k_{0,\infty} e^{-c_m \cdot e_{eff}} \left(1 + \frac{b(\sigma_{eff})}{p_{mean}}\right) \quad (19)$$

The anisotropy of permeability

The intrinsic permeability of a porous medium is spatially anisotropic – that is, it depends on the direction of flow. For an isotropic permeability, Darcy's law is most frequently formulated as a scalar equation (Eq. 7). In contrast, an anisotropic permeability must be treated as a tensor:

$$Q_i = -\frac{k_{ij}}{\mu}\frac{\partial p}{\partial x_j} \quad (20)$$

where Q_i is the flux rate in direction I and k_{ij} represents the components of the permeability tensor. The last term $\partial p/\partial x_j$ describes the pressure gradient in direction x_j.

The anisotropy of permeability in porous media has been investigated experimentally since the 1950s (for example, Rice et al. (1970)). Numerous studies have shown that the matrix permeability of shale is highly anisotropic compared to classical reservoir rock such as a sandstone or carbonate (compare Bolton et al., 2000; Kwon et al., 2004; Neuzil, 1994). In fine-grained sedimentary rocks, including shales, permeability coefficients measured parallel to bedding are typically larger than those measured perpendicular to bedding. For example, Armitage et al. (2011) found permeability variations of up to 4 orders of magnitude between the flow parallel and perpendicular to bedding.

In recent years, research has turned to the factors controlling anisotropic permeability behavior. Heterogeneity and anisotropy are closely related rock properties (Bernabé, 1992) – a perfect homogeneous specimen would have the same flow properties in all directions. The permeability anisotropy of shales reflects sediment heterogeneity and particle alignment. Shale heterogeneity is primarily dependent on the conditions of sediment deposition and the formation of silt–clay lamination and particle alignment. It is also influenced by subsequent mechanical compaction and clay mineral recrystallization (Yang and Aplin, 2007, 2010).

In conclusion, the permeability of a typical shale is much higher parallel to bedding than perpendicular to bedding (Figs. 21 and 22). These very high permeability anisotropy ratios are related to the microstructure of the rock (bedding/lamination planes), the presence of micro-fractures, and the orientation of minerals and pores/cracks along a preferential direction as the result of sedimentation, compaction, and diagenesis (Klaver et al., 2015; Pathi, 2008; Yang and Aplin, 2010). In addition, Berg and Gangi (1999) described how micro-fractures could occur during hydrocarbon generation and expulsion from Eagle Ford and Austin chalk.

Three main reasons can be identified for an anisotropic permeability behavior of organic-rich shales:

- Porosity and connectivity differences attributed to mineralogy (Arnedo et al., 2013; Houben et al., 2013; Klaver et al., 2015), especially clay particle alignment under overburden stress (Clennell et al., 1999; Yang and Aplin, 2007).
- Heterogeneity associated with mineralogical layering of high and low permeability layers (Klaver et al., 2015; Behnsen and Faulkner, 2011; Crawford et al., 2008; Kanitpanyacharoen et al., 2012).
- Microstructural textures (Anders et al., 2014), including natural fractures (Timms et al., 2010) and artificially induced fractures.

Particle alignment describes the tendency of clay particles to rotate along an existing load. Due to particle alignment, the tortuosity is expected to be less for fluid flow parallel to bedding compared to perpendicular to bedding (Clennell et al., 1999; Dewhurst et al., 1998). Yang and Aplin (2007) attributed permeability aniso-

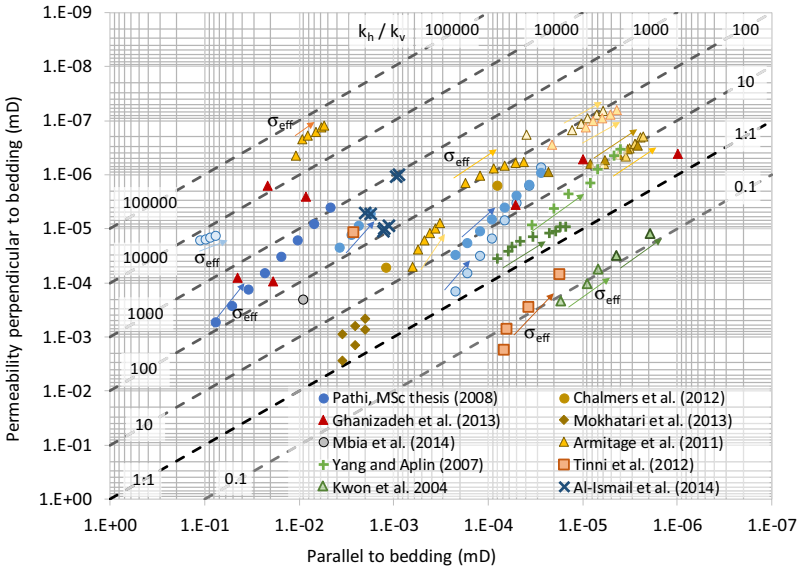

Fig. 21. The figure illustrates the permeability differences between the flow orientation parallel and perpendicular to bedding in shales (data compiled from Armitage et al. (2011), Yang and Aplin (2007), Bustin et al. (2008), Chalmers et al. (2012b), Kwon et al. (2004), Ghanizadeh et al. (2014a,b), Mbia et al. (2014), Mokhtari et al. (2013), and Pathi (2008). All permeability anisotropies measured as a function of effective stress are indicated with an arrow in direction of increasing effective stress. Tinni et al. (2012) were able to determine the anisotropy of two Ordovician age samples using the GRI technique, but they only determined permeability anisotropy as a function of effective stress for one of the samples. The data set of Mokhtari et al. (2013) (diamonds) shows the anisotropy for different samples, not as a function of effective stress.

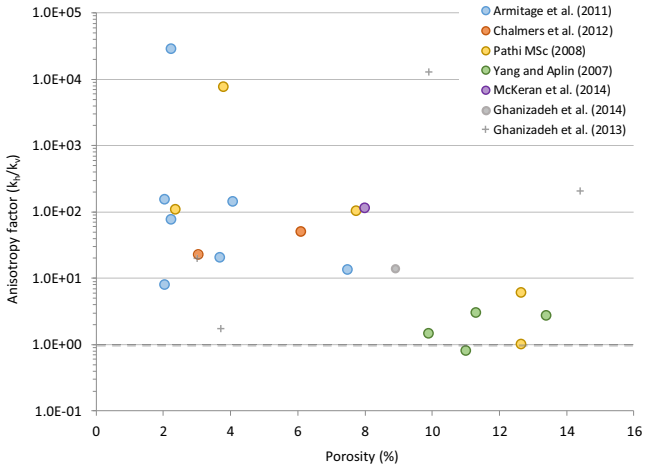

Fig. 22. The porosity–permeability anisotropy relationship is a consequence of simple pore network concepts. Increasing porosity results in a decreasing permeability anisotropy because the likelihood of anisotropic connectivity between the pores increases with increasing porosity. This data set, which contains 25 data points, is only able to provide a statistical indication of the validity of this hypothesis for shales. Data points indicated as gray crosses are considered potential outliers. Given the age (30 years) and source (3 wells) of the samples these data points are based on, we hypothesize that these outliers represent samples containing a high density of artificial micro-fractures (Ghanizadeh et al., 2013).

tropy ratios between 1.7 and 11.2 for mudstones to particle alignment and material heterogeneity. In addition to these factors, the void space (porosity) between clay particles in shales is elongated parallel to bedding (Houben et al., 2013; Klaver et al., 2012). This indicates that the best connectivity between the pores exists in this direction. However, we were not able to identify in our comprehensive data-set a general correlation between anisotropy factor and total clay content. In conclusion, the development of anisotropic permeability, where the horizontal permeability of a consolidated sediment is greater than the vertical permeability at any given porosity, is due to the combination of several mineralogical and depositional factors (Clennell et al., 1999).

Sedimentary layering can explain larger magnitudes of anisotropic permeability (Armitage et al., 2011). Alternating layers of high and low permeability shales causes high anisotropy. For example, anisotropic properties could be related to changes in clay content or the presence of larger carbonaceous shell fragments (Chalmers et al., 2012b; Clavaud et al., 2008). Armitage et al. (2011) has studied samples in which well-defined clay- and quartz-rich layers alternate with thin, chlorite-rich beds. In this case, the layering resulted in a maximum permeability anisotropy of four orders of magnitude.

A final source of anisotropy may be the presence of micro-fractures (Benson et al., 2006; Bolton et al., 2000; Fan et al., 2012a,b; Kwon et al., 2004; Lash and Engelder, 2005). Natural fractures, coring induced fractures, and hydraulic fractures are stress-sensitive and form preferentially along certain planes, resulting in high permeability along those planes (Bruno, 1994; Cho et al., 2013; Gutierrez et al., 2000; Holt et al., 2011; Kwon et al., 2004; Petunin et al., 2011). This hypothesis, however, does not explain why the orientation of micro-fractures is almost exclusively in the bedding-parallel direction, which is perpendicular to the maximum stress S_v. One explanation for the origin of bedding parallel natural microfractures in organic-rich shales is that they are related to the thermal maturation of kerogen (Vernik, 1993, 1994). Vernik (1994) found that intrinsic anisotropy can be enhanced in thermally mature shales by bedding-parallel microcracks, which could be caused by the processes of hydrocarbon generation. They attempt to explain the relationship between micro-fracture propagation and maturation by considering the possibility of a pore pressure increase generated by the conversion of kerogen to oil and gas within pore spaces (Berg and Gangi, 1999).

Artificial micro-fractures induced as a result of the stress release during coring, core transfer, and core plug preparation for laboratory studies (Anders et al., 2014), are able to cause significant permeability anisotropies as well. Because the tensile strength of layered shale formations is low, it is probable to have micro-

fractures parallel to the bedding since rocks expand after stress release mostly in the direction of highest stress.

Stress sensitivity of permeability anisotropy. Fig. 21 shows the anisotropy of permeability for a variety of shale samples. For some samples, the sensitivity of permeability anisotropy to effective stress is measured, this is indicated by arrows in Fig. 21 and further evaluated in Fig. 23. The stress sensitivity of the permeability is higher in the horizontal than the vertical direction in all cases (Fig. 23), (except for a sample from the permeability data set of Armitage et al., 2011). It is worth noting that permeability anisotropy increases with increasing effective stress for all shales (Fig. 21). This indicates that the permeability parallel to bedding is less sensitive to effective stress changes than the permeability perpendicular to bedding. This could be explained by increasing tortuosity, reduction in amount of available pore throats, clay particle alignment, or mineral layering.

Permeability anisotropy should show a higher stress sensitivity in comparison to the matrix permeability when such anisotropy is related to fractures (Table 12). Compared to natural fractures, artificial fractures should show even more sensitivity to effective stress because they have a higher asperity height distribution. Such artificial microfractures should have a high fracture compressibility compared to quartz layers. This should result in a decreasing anisotropy with increasing effective stress. Only a few samples of the data collection (Fig. 21) show this type of trend, the majority follow the opposite trend. Kwon et al. (2004) observed that horizontal shale permeability is usually one order of magnitude greater than vertical permeability for effective pressures of approximately 3 MPa. However, they reported that as effective stress increases, the permeability becomes less anisotropic (Kwon et al., 2004). This indicates that porous layers controlling horizontal permeability may collapse at higher pressures, resulting in a reduction in permeability anisotropy (Fisher et al. (2001). However, it might be assumed that the micro-fractures are already closed at the effective stresses applied in these studies (Table 9). Based on the leaking evidence of stress sensitivity in the horizontal direction, we conclude that artificial micro-fractures are of only minor importance compared to natural fractures, which have a major influence on the magnitude of permeability anisotropy.

In conclusion, enhanced stress sensitivity in the vertical direction compared to the horizontal direction is most likely related to bedding-parallel micro-fractures in the clay that are not interconnected in horizontal direction. The closure of these microfractures increases tortuosity drastically in the vertical direction, reducing the permeability in that direction significantly. Horizontal permeability is less influenced by changes in stress because it is mainly related to the layering of high (quartz-rich) and low (clay-rich) permeability layers.

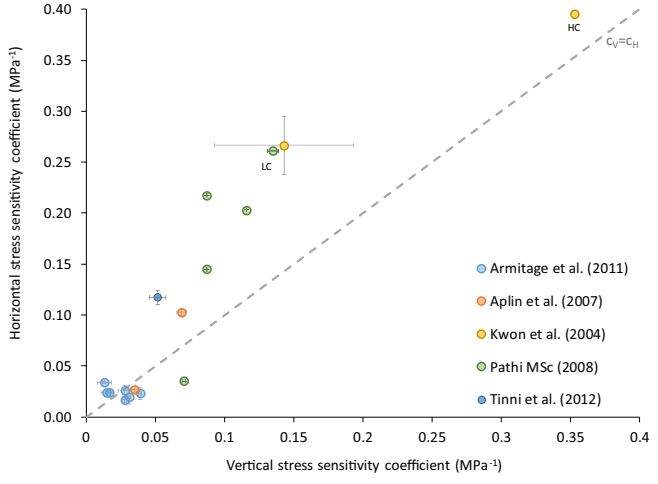

Fig. 23. The stress sensitivity of permeability for flow orientations parallel and perpendicular to bedding (data compiled from Ghanizadeh et al. (2013, 2014a,b), Kwon et al. (2001, 2004), McKernan et al. (2014b), Pathi (2008), Tinni et al. (2012), Yang and Aplin (2007)).

Capillary processes

Capillary pressure-controlled viscous flow of oil and gas has been investigated during the last decades in the context of the exploration and production of natural hydrocarbons. Primary focus was given on the characterization of flow in high-permeability reservoir rocks, where capillary processes are not as important as those for shale oil/gas reservoirs. Research covered experimental and theoretical studies with the aim to quantify transport efficiency or trapping/retention mechanisms (Bandara et al., 2011; Berg, 1975; Schowalter, 1979). Recently, focus shifted to the analysis of tight sandstone (Cluff and Byrnes, 2010; Shanley et al., 2004) and gas/oil shale formations (Ghanizadeh et al., 2013, 2014a). Another research field focusses on the gas generation and dissipation in radioactive waste sites. In this context, several studies were conducted to analyze the gas breakthrough characteristics of weak natural and synthetic clays and clay-rich host rock formations (Harrington and Horseman, 1999; Horseman et al., 1999; Marschall, 2005; Ortiz et al., 2002).

In general, tight rocks are characterized by very small pores down to the nm-range resulting in larger capillary resistance, and consequently in a low relative non-wetting phase permeability. In comparison to clean sandstones, capillary threshold pressures required for "efficient gas flow" are much higher and the percentage of immobile water increases. Researchers observed water saturation regions with virtually no-flow, i.e. where relative gas/water permeabilities are <2% (Castle and Byrnes, 2005; Cluff and Byrnes, 2010). In clay-rich rocks, gas flow rates detected after gas breakthrough can be extremely low, corresponding to relative gas permeability coefficients down to 10^{-3}% (Amann-Hildenbrand et al., 2013). A comprehensive literature review of capillary gas breakthrough pressures determined on fully water saturated sample plugs is given in Busch and Amann-Hildenbrand (2013). The study uses empirical relationships and an extended dataset of

Table 12
Summary of the causes of permeability anisotropy.

Anisotropy Kh/kv	Physical reason	Stress sensitivity	Sources
$1/\infty$ – 1	Vertical fractures	Soft-medium	Tinni et al. (2012)
1–10	Clay particle alignment	medium	Clennell et al. (1999), Yang and Aplin (2007), Mokhtari et al. (2013)
10–100	Layering of high and low permeable structures parallel to bedding	Strong	Armitage et al. (2011)
100–∞	Horizontal micro fractures of different origin	Soft-medium	Armitage et al. (2011), Tinni et al. (2012)

233 rock samples (165 mudstones, 27 sandstone, 25 carbonate, 11 anhydrite and 5 marlstone datasets) to calculate the capillary breakthrough and snap-off pressures, parameters which are required for instance to predict the capillary sealing capacity of CO_2 storage sites. Values compiled from N_2 and He gas breakthrough experiments cover gas breakthrough-values ranging from $5 \cdot 10^{-3}$ MPa for sandstones ($k \sim 10^{-13}$ m^2) to 30 MPa for mudrocks (10^{-21} m^2). This trend is visualized in Fig. 24, which plots selected critical capillary pressures and their relation to intrinsic permeability. In general, a fair correlation was obtained between values derived from mercury injection porosimetry (MIP) and the "in-situ" capillary entry/breakthrough pressure, but not with the capillary snap-off pressure (Busch and Amann-Hildenbrand, 2013).

We use the data set in Fig. 24 to calculate a semi-empirical first order approximation for a minimum capillary displacement pressure at a given intrinsic permeability.

$$p_{entry} \geqslant 3.48 \times 10^{-8} k_{matrix}^{-0.342} \quad \text{for } k_{matrix} \text{ between } 10^{-13}\,\text{m}^2 \text{ and } 10^{-21}\,\text{m}^2$$

.

$$p_{entry} \geqslant 0.5\,\text{MPa} \quad \text{for } k_{matrix} \text{ below } 10^{-21}\ \text{m}^2.$$

where k is the intrinsic (water) permeability in m^2 and p_{entry} is the minimum capillary entry pressure in MPa. This simplification does not include the poroelastic effects.

Al-Bazali and co-workers (Al-Bazali et al., 2007, 2009a,b) showed that capillary invasion of different non-wetting phases (oil based mud, crude oil, decane and nitrogen) clearly depended on rock properties (wettability, permeability, cation exchange capacity) and the non-wetting fluid properties. They observed, that the addition of emulsifiers in oil-based mud led to a reduction of capillary entry pressure as interfacial tension is reduced.

The uptake of wetting fluids within the pore matrix by spontaneous imbibition is another hot topic in the context of large fracking fluid losses, water blocking (ceasing gas production) or the initiation of counter-current degassing. In order to understand water/oil uptake or gas release mechanisms, Dehghanpour et al. (2012) conducted several water and oil imbibition experiments on strongly oil-wet samples (Fort Simpson and Muskwa formation). In contradiction to the capillary theory, they observed that all samples imbibed more water than oil, even though samples were characterized by a contact angle of zero for the oil phase. The authors attribute this to the additionally sorptive uptake of water. Mixed preferred wettability was also observed by Odusina et al. (2011) and Sulucarnain et al. (2012). While some samples took up more water than oil/dodecane (Barnett, Eagle Ford, and Floyd shales), other samples preferently imbibed oil (Woodford shale). The authors related the uptake of oil to TOC content, thermal maturity and organic pore volume, water uptake to clay minerals and fractures. Zhou et al. (2014) observed that the degree of fracking fluid uptake primarily depends on clay content. Porosity, TOC content and contact angle had only influence on the imbibition velocity, but not on the total amount of uptake.

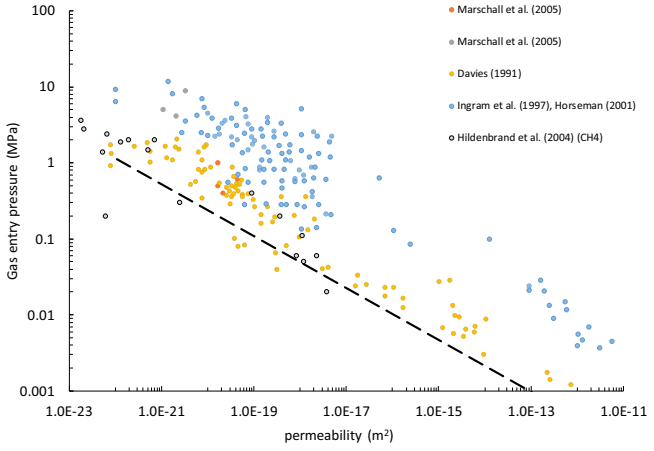

Fig. 24. The intrinsic permeability as a function of gas entry pressure on the basis of methane and water (interfacial tension $\sigma = 0.042$ Nm^{-1} and wetting angle of $\Theta = 0°$). This relationship is a consequence of simple pore network concepts which could be in the simplest form a capillary bundle model. Increasing permeability results in a decreasing gas entry pressure because the likelihood of bigger pore throat diameters increases with increasing permeability. This data set contains more than 300 data points (Hildenbrand et al., 2002; Hildenbrand et al., 2004; Ibrahim et al., 1970; Ingram et al., 1997; Marschall et al., 2005).This data set is only able to provide a statistical indication of the validity of this hypothesis for shales.

Apart from the uncertainties associated with the interpretation of the experimental capillary pressure curves, the above procedure involves several unknowns which may critically influence the hydrocarbon entry pressure prediction. While interfacial tensions (σ) of hydrocarbon/water systems in the temperature and pressure ranges of interest have been measured or can be estimated with some confidence, the wettability of the shale represents a major problem. Commonly a wetting angle (Θ) of zero is assumed. Implying a completely water-wet shale. This assumption is likely to be wrong for shale containing significant amounts of organic matter. The complexity of this problem is increased by potential wettability changes of seals due to petroleum generation or impregnation.

Molecular transport

The interaction of hydrocarbon gases, in particular methane, with the dispersed organic matter is one of the fundamental mechanisms controlling gas storage and transport in shales and remains a high-priority research issue.

Krooss et al. (1992) compared effective diffusion coefficients for methane measured at different temperatures with the corresponding diffusion coefficients of methane in water. Due to the tortuosity of the transport pore system and the interaction of methane with the sedimentary organic matter, the effective diffusion coefficients in the water-saturated rocks are consistently lower by up to more than 2 orders of magnitude than in water.

Diffusion in small pores

Pore systems in shales and sedimentary organic matter, in particular coals, extend down to molecular sizes and thus are at the limit of conventional methods for pore system characterization. As these pore sizes are of the same order of magnitude as the molecular size of both solvent and solute, the solvent can no longer be treated as a continuum. In the case of "free" gas transport, depending on pressure and temperature, molecule-pore wall interactions tend to become more important than molecule–molecule interactions. Some of the main mechanisms, which have been extensively discussed in the literature, are Knudsen diffusion, surface diffusion, capillary condensation and molecular sieving. Experience shows that in laboratory experiments investigating gas transport in shales it is often not possible to distinguish unambiguously between pressure-driven volume flow in open capillaries and diffusive transport of dissolved gas in fluid-saturated pore systems (Amann-Hildenbrand et al., 2012, 2013). In both cases the flux is proportional to gas pressure gradients and both descriptions are equally viable.

Isotopic fractionation

Diffusive transport of gas in shales can give rise to both, molecular and isotopic fractionation processes. In gas-phase diffusion

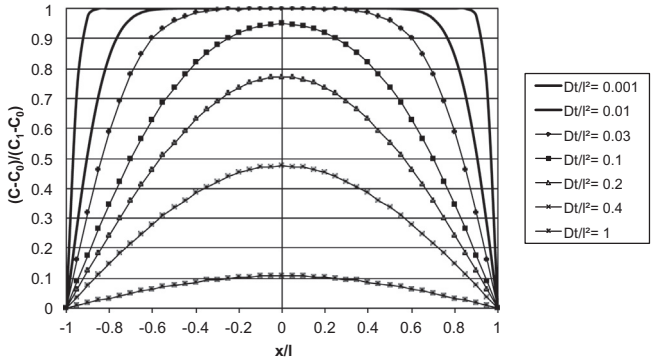

Fig. 25. Concentration profiles for diffusion out of a plane sheet of thickness 2*l* with initial concentration C0 and zero concentrations ($C = 0$) at both sides (after Crank, 1975, Eq. 4.17).

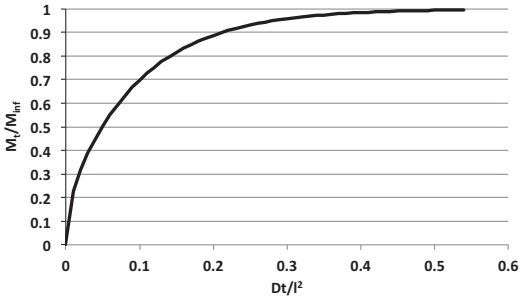

Fig. 26. The normalized mass uptake of diffusion out of a plane sheet of thickness 2*l* as a function of time with initial concentration C_0 and zero concentrations ($C = 0$) at both sides (after Crank, 1975, Eq. 4.18).

these fractionations are mainly caused by differences in molar mass ($D \sim$ square root of reciprocal molar mass). For diffusive fractionation in liquids, the collision radii and molecular interaction parameters play a predominant role. In carbonaceous shales, interaction of hydrocarbon gases with the organic matter has a noticeable and possibly dominating impact on diffusive fractionation. Fractionation effects are therefore expected to be most prominent for gases with low molar masses and significant differences in molar mass. This holds particularly for isotopic fractionation. Diffusion experiments with methane on carbonaceous shales at elevated pressures and temperatures (Zhang and Krooss, 2001) revealed that effective diffusion coefficients of $^{13}CH_4$ were consistently smaller than those of $^{12}CH_4$. Diffusion-related isotope effects expressed as:

$$\mathrm{IE}(D) = \left(\frac{D(^{13}\mathrm{CH_4})}{D(^{12}\mathrm{CH_4})} - 1\right) \times 1000 \qquad (21)$$

ranged from −1.3‰ to −3.3‰ and showed a clear dependence on organic matter content.

Although these diffusion-related isotopic fractionation effects are readily measured in the laboratory on a length-scale of several mm to cm, they are unlikely to be of relevance on significantly larger size-scales (tens to hundreds of m). The issue of diffusive transport in source rocks and caprocks on geological time-scales has been discussed in some detail and the reader is referred to the corresponding literature (e.g. Krooss and Leythaeuser, 1997).

Although the mechanisms of gas release from the matrix of gas shales after hydraulic fracturing are not understood in full detail, they may be tentatively described in terms of a diffusion process, keeping in mind that pressure-driven volume flow and molecular diffusion tend to become indistinguishable in extremely low-permeability rocks. The concentration profiles of the diffusing substance in a *plane sheet* of thickness 2*l* envisaged to represent the rock volume between two fractures are shown in Fig. 25. The rock volume is assumed to have an initial concentration C_0 of diffusant throughout. Upon opening of the fractures (time: t_0) the gas concentration at both sides of the plane sheet drops to zero instantaneously and the plane sheet starts to degas. The concentration profiles for different values of the factor Dt/l^2 can be calculated by the following formula (Crank, 1975, Eq. 4.17).

$$\frac{C - C_0}{C_1 - C_0} = 1 - \frac{4}{\pi}\sum_{n=0}^{\infty}\frac{(-1)^n}{2n+1} e^{-D(2n+1)^2\pi^2\frac{t}{4l^2}} \cos\frac{(2n+1)\pi x}{2l}$$

Profiles for selected values of Dt/l^2 are shown in Fig. 25. Evidently, the concentration in the center of the plane sheet has decreased to approximately 10% of the initial value C_0 for $Dt/l^2 = 1$. Given the average fracture distance (2*l*) and the effective gas diffusion coefficient the time required for degassing of rock volume between the fractures can be estimated.

Using the same model and argumentation, the fraction of the original gas in place that has left the plane sheet (M_t/M_∞) can be calculated as a function of time (Crank, 1975, Eq. 4.18):

$$\frac{M_t}{M_\infty} = 1 - \sum_{n=0}^{\infty}\frac{8}{(2n+1)^2\pi^2} e^{(-D(2n+1)^2\pi^2\frac{t}{4l^2}}$$

The normalized mass uptake function for diffusion into a plane sheet is plotted in Fig. 26. The normalized diffusive mass loss from a plane sheet is given by the complement ($1 - M_t/M_\infty$).

Concluding remarks

This review summarizes the present state of knowledge on the transport processes in shale gas recovery. We aimed at summarizing the various qualitative and quantitative findings related to sorption, porosity and transport data. Further, we provided insights into experimental details of determination of permeability and uncertainties related therewith.

In the following, various aspects that still need to be researched for a better understanding of gas production from shales have been defined:

- Due to the higher compressibility of shale reservoirs as compared to conventional reservoirs, some processes have to be considered as coupled such as the transition from Darcy-flow to slip-flow and the stress sensitivity of the permeability to pore throat compressibility, which is a poroelastic effect. We also develop a detailed description of the coupling between slip-flow and the stress sensitivity in shale gas reservoirs, and interpret experimental observations in light of this description.
- We characterize the transport properties of shales in a manner that includes a zero-effective-stress permeability coefficient, a stress sensitivity coefficient, an effective stress coefficient and slippage as a function of effective stress.

Acknowledgments

Yves Gensterblum has worked out the whole paper except the fracture flow chapter by Robert Cuss and John Harrington, the molecular transport chapter by Bernhard M. Krooss and the chapter on experimental determination methods of permeability which has been written by Amin Ghanizadeh and Christopher R. Clarkson. Alexandra Amann and Yves Gensterblum have worked out the chapter on capillary processes.

Yves Gensterblum and Mark Zoback gratefully acknowledge the Stanford Center for Rockphysics and Borehole Geophysics (SRB) consortium for getting the opportunity to work on this article. Amin Ghanizadeh and Christopher R. Clarkson gratefully thank University of Calgary for the "Eyes High" Postdoctoral Fellowship (offered to Amin Ghanizadeh) and the sponsors of the Tight Oil Consortium hosted at the University of Calgary.

Appendix

Calculation of the aspect ratio

The maximum aperture b of the fracture at its midpoint is given by

$$b_{\max} = \frac{2(P_{\text{pore}} - S_3)L(1 - v^2)}{E}$$

where p_{pore} is the fluid pressure in the fracture, v is the Poisson's ratio and E the Youngs modulus. Considering 0.3 MPa as a reasonable upper bound for $p_{\text{pore}} - S_3$ in one meter long micro fracture. For reasonable values of $E = 3$ GPa and $v = 0.3$ for shales, the maximum aperture would be on the order of 0.01 mm. Obviously, considering a fracture of 1 m length is arbitrary, if L increases $b_{\max}$ increases as well. However when L increases, the maximum value of $P_{\text{pore}} - S_3$ decreases thereby limiting $b_{\max}$.

Conversion of capillary entry pressure

The capillary entry pressure is given by:

$$P_c = \frac{2\sigma \cos\theta}{r}$$

where σ is the interacial tension between the hydrocarbon phase and the water, Θ is the contact angle and r is the shale pore throat radius.

For converting the air-mercury (A) measurments to the more interesting CH_4–water (B) basis the equation can be formulated in the following way:

$$\frac{\sigma_A \cos(\theta_A)}{P_c^A} = \frac{\sigma_B \cos(\theta_B)}{P_c^B}$$

consequently

$$\frac{P_c^B}{P_c^A} = \frac{\sigma_B \cos(\theta_B)}{\sigma_A \cos(\theta_A)}$$

For mercury/air/shale the interfacial tension $\sigma = 0.471\ \text{Nm}^{-1}$ and wetting angle is $\Theta = 140°$. For methane/water/shale the interfacial tension is $\sigma = 0.042\ \text{Nm}^{-1}$ and the wetting angle is $\Theta = 0°$ (Schlömer, 1997).

References

Aguilera, R., 2002. Incorporating capillary pressure, pore throat aperture radii, height above free-water table and winland r35 values on Pickett plots. AAPG Bulletin 86 (4), 605–624.

Akkutlu, I.Y., Fathi, E., 2011. Gas Transport in Shales with Local Kerogen Heterogeneities. Society of Petroleum Engineers.

Al-Bazali, T.M., Zhang, J., Chenevert, M.E., Sharma, M.M., 2007. Capillary entry pressure of oil-based muds in shales: the key to the success of oil-based muds. Energy Sources Part A 30, 297–308.

Al-Bazali, T.M., Zhang, J., Chenevert, M.E., Sharma, M.M., 2009a. Estimating the Reservoir Hydrocarbon Capacity through Measurement of the Minimum Capillary Entry Pressure of Shale Caprocks. Society of Petroleum Engineers.

Al-Bazali, T.M., Zhang, J., Chenevert, M.E., Sharma, M.M., 2009b. An Experimental Investigation on the Impact of Capillary Pressure, Diffusion Osmosis, and Chemical Osmosis on the Stability and Reservoir Hydrocarbon Capacity of Shales. Society of Petroleum Engineers.

Amann-Hildenbrand, A., Ghanizadeh, A., Krooss, B.M., 2012. Transport properties of unconventional gas systems. Mar. Pet. Geol. 31, 90–99.

Amann-Hildenbrand, A., Bertier, P., Busch, A., Krooss, B.M., 2013. Experimental investigation of the sealing capacity of generic clay-rich caprocks. Int. J. Greenhouse Gas Control 19, 620–641.

Anders, M.H., Laubach, S.E., Scholz, C.H., 2014. Microfractures: a review. J. Struct. Geol.

Angeli, M., Soldal, M., Skurtveit, E., Aker, E., 2009. Experimental percolation of supercritical CO_2 through a caprock. Energy Procedia 1, 3351–3358.

Antonov, P.L., 1954. On the diffusion of some claystones. Tr. NIIGGR. Sb. Geokhim. Met. Poisk. Neft. i Gaza 2, 39–55 (in Russian).

Antonov, P.L., 1964, On the extent of diffusive permeability of rocks, in Sb.: Direct Methods of Oil and Gas Exploration. Nedra, Moscow, pp. 5–13. (in Russian).

Antonov, P.L., 1968. Some results of the research on molecular migration of hydrocarbon gases in rocks. Tr. VNIIYaGG 4, 132–154 (in Russian).

Antonov, P.L., 1970. Results of the investigation of diffusion permeability of sedimentary rocks for hydrocarbon gases. Tr. VNIIYaGG 8, 51–59 (in Russian).

Archie, G.E., 1950. Introduction to petrophysics of reservoir rocks. Am. Assoc. Pet. Geol. Bull. 34 (5), 943–961.

Armitage, P.J., Faulkner, D.R., Worden, R.H., Aplin, A.C., Butcher, A.R., Iliffe, J., 2011. Experimental measurement of, and controls on, permeability and permeability anisotropy of caprocks from the CO_2 storage project at the Krechba Field, Algeria. J. Geophys. Res. Solid Earth 116, B12208.

Arnedo, D., Alonso, E.E., Olivella, S., 2013. Gas flow in anisotropic claystone: modelling triaxial experiments. Int. J. Numer. Anal. Meth. Geomech. 37, 2239–2256.

Ashrafi Moghadam, A., Chalaturnyk, R., 2014. Expansion of the Klinkenberg's slippage equation to low permeability porous media. Int. J. Coal Geol. 123, 2–9.

Askarieh, M.M., Chambers, A.V., Daniel, F.B.D., FitzGerald, P.L., Holtom, G.J., Pilkington, N.J., Rees, J.H., 2000. The chemical and microbial degradation of cellulose in the near field of a repository for radioactive wastes. Waste Manage. 20, 93–106.

Autio, J., Gribi, P., Johnson, L., Marschall, P., 2006. Effect of excavation damaged zone on gas migration in a KBS-3H type repository at Olkiluoto. Phys. Chem. Earth Parts A/B/C 31, 649–653.

Bandara, U.C., Tartakovsky, A.M., Palmer, B.J., 2011. Pore-scale study of capillary trapping mechanism during CO_2 injection in geological formations. Int. J. Greenhouse Gas Control 5, 1566–1577.

Bennion, B., Bachu, S., 2006. The impact of interfacial tension and pore size distribution/capillary pressure character on CO_2 relative permeability at reservoir conditions in CO_2-brine. In: Systems Symposium on Improved Oil Recovery SPE/DOE Tulsa, Oklahoma, p. 10.

Benson, S.M., 2014. Negative-emissions insurance. Science 344, 1431.

Berg, R.R., 1975. Capillary pressure in stratigraphic traps. AAPG Bull. 59, 939–956.

Berg, R.R., Gangi, A.F., 1999. Primary migration by oil-generation microfracturing in low-permeability source rocks; application to the Austin Chalk, Texas. AAPG Bull. 83, 727–756.

Bernabe, Y., 1987. The effective pressure law for permeability during pore pressure and confining pressure cycling of several crystalline rocks. J. Geophys. Res. Solid Earth 92, 649–657.

Bernabé, Y., 1992. Chapter 6 on the measurement of permeability in anisotropic rocks. In: Brian, E., Teng-fong, W. (Eds.), International Geophysics. Academic Press, pp. 147–167.

Berryman, J.G., 1992. Effective stress for transport properties of inhomogeneous porous rock. J. Geophys. Res. Solid Earth 97, 17409–17424.

Berryman, J.G., 1993. Effective-stress rules for pore-fluid transport in rocks containing two minerals. Int. J. Rock Mech. Min. Sci. Geomech. Abstr. 30, 1165–1168.

Biot, M.A., 1941. General theory of three-dimensional consolidation. J. Appl. Phys. 12, 155–164.

Biot, M.A., Willis, D.G., 1957. The elastic coefficient of the theory of consolidation. J. Appl. Mech. 24, 594–601.

Birol, F., 2012. World Energy Outlook 2012. International Energy Agency (IEA), Paris, p. 633.

Blasingame, T.A., Moridis, G.J., Freeman, C., 2013. Modeling and performance interpretation of flowing gas composition changes in shale gas wells with complex fractures. In: International Petroleum Technology Conference.

Bloomberg, M.R., Krupp, F., 2014. The right way to develop shale gas. The New York Times.

Boulin, P.F., Bretonnier, P., Gland, N., Lombard, J.M., 2010. Low water permeability measurements of clay sample. Contribution of steady state method compared to transient methods. In: International Symposium of the Society of Core Analysis, Halifax, Canada.

Boulin, P.F., Bretonnier, P., Vassil, V., Samouillet, A., Fleury, M., Lombard, J.M., 2013. Sealing efficiency of caprocks: experimental investigation of entry pressure measurement methods. Mar. Pet. Geol. 48, 20–30.

Bourbie, T., Walls, J., 1982. Pulse decay permeability: analytical solution and experimental test, 12

Brace, W.F., Walsh, J.B., Frangos, W.T., 1968. Permeability of granite under high pressure. J. Geophys. Res. 73, 2225–2236.

Brezovski, R., Cui, A., 2013. Laboratory Permeability Measurements of Unconventional Reservoirs: Useless or Full of Information? A Montney Example from the Western Canadian Sedimentary Basin. Society of Petroleum Engineers.

Bruno, M.S., 1994. Micromechanics of stress-induced permeability anisotropy and damage in sedimentary-rock. Mech. Mater. 18, 31–48.

Busch, A., Amann-Hildenbrand, A., 2013. Predicting capillarity of mudrocks. Mar. Pet. Geol. 45, 208–223.

Busch, A., Gensterblum, Y., Krooss, B.M., Littke, R., 2004. Methane and carbon dioxide adsorption–diffusion experiments on coal: upscaling and modeling. Int. J. Coal Geol. 60, 151–168.
Bustin, R.M., Bustin, A.M.M., Cui, X., Ross, D.J.K., Pathi, V.S.M., 2008. Impact of shale properties on pore structure and storage characteristics. In: Society of Petroleum Engineers – Shale Gas Production Conference 2008, pp. 32–59.
Can, B., Kabir, S., 2012. Probabilistic Production Forecasting for Unconventional Reservoirs with Stretched Exponential Production Decline Model.
Carles, P., Egermann, P., Lenormand, R., Lombard, J.M., 2007. Low permeability measurements using steady-state and transient methods. In: SCA International Symposium, p. 12.
Castle, J.W., Byrnes, A.P., 2005. Petrophysics of lower Silurian sandstones and integration with the tectonic-stratigraphic framework, appalachian basin, United States. AAPG Bull. 89, 41–60.
Chalmers, G.R., Bustin, R.M., Power, I.M., 2012a. Characterization of gas shale pore systems by porosimetry, pycnometry, surface area, and field emission scanning electron microscopy/transmission electron microscopy image analyses: examples from the Barnett, Woodford, Haynesville, Marcellus, and Doig units. AAPG Bull. 96, 1099–1119.
Chalmers, G.R.L., Ross, D.J.K., Bustin, R.M., 2012b. Geological controls on matrix permeability of Devonian Gas Shales in the Horn River and Liard basins, northeastern British Columbia, Canada. Int. J. Coal Geol.
Chen, T., Stagg, P.W., 1984. Semilog Analysis of the Pulse-Decay Technique of Permeability Measurement, SPE-11818-PA.
Chenevert, M.E., Sharma, A.K., 1993. Permeability and Effective Pore Pressure of Shales.
Cho, Y., Ozkan, E., Apaydin, O.G.C.S.P.E., 2013. Pressure-Dependent Natural-Fracture Permeability in Shale and Its Effect on Shale-Gas Well Production, SPE-159801-PA.
Civan, F., 2010. Effective correlation of apparent gas permeability in tight porous media. Transp Porous Med 82, 375–384.
Civan, F., Rai, C.S., Sondergeld, C.H., 2011. Shale-gas permeability and diffusivity inferred by improved formulation of relevant retention and transport mechanisms. Transp Porous Med 86, 925–944.
Civan, F., Rai, C.S., Sondergeld, C.H., 2012. Determining shale permeability to gas by simultaneous analysis of various pressure tests. SPE J. 17, 717–726.
Clarkson, C.R., 2013a. Production data analysis of unconventional gas wells: review of theory and best practices. Int. J. Coal Geol. 109–110, 101–146.
Clarkson, C.R., 2013b. Production data analysis of unconventional gas wells: workflow. Int. J. Coal Geol. 109–110, 147–157.
Clarkson, C.R., Bustin, R.M., 1999. The effect of pore structure and gas pressure upon the transport properties of coal: a laboratory and modeling study. 2. Adsorption rate modeling. Fuel 78, 1345–1362.
Clarkson, C.R., Williams-Kovacs, J., 2013. Modeling Two-Phase Flowback of Multifractured Horizontal Wells Completed in Shale, SPE-162596-PA.
Clarkson, C.R., Freeman, M., He, L., Agamalian, M., Melnichenko, Y.B., Mastalerz, M., Bustin, R.M., RadliÅski, A.P., Blach, T.P., 2012a. Characterization of tight gas reservoir pore structure using USANS/SANS and gas adsorption analysis. Fuel 95, 371–385.
Clarkson, C.R., Jensen, J.L., Pedersen, P.K., Freeman, M., 2012b. Innovative methods for flow-unit and pore-structure analyses in a tight siltstone and shale gas reservoir. AAPG Bull. 96, 355–374.
Clavaud, J.-B., Maineult, A., Zamora, M., Rasolofosaon, P., Schlitter, C., 2008. Permeability anisotropy and its relations with porous medium structure. J. Geophys. Res. Solid Earth 113, B01202.
Clennell, M.B., Dewhurst, D.N., Brown, K.M., Westbrook, G.K., 1999. Permeability anisotropy of consolidated clays. Geol. Soc. Lond. Spec. Publ. 158, 79–96.
Cluff, R.M., Byrnes, A.P., 2010. Relative Permeability in Tight Gas Sandstone Reservoirs – The "Permeability Jail" Model. Society of Petrophysicists and Well-Log Analysts.
Crafton, J.W., Noe, S., 2013. Factors Affecting Early Well Productivity in Six Shale Plays. Society of Petroleum Engineers.
Cui, X., Bustin, A.M.M., Bustin, R.M., 2009. Measurements of gas permeability and diffusivity of tight reservoir rocks: different approaches and their applications. Geofluids 9, 208–223.
Cui, A., Wust, R., Nassichuk, B., Glover, K., Brezovski, R., Twemlow, C., 2013. A Nearly Complete Characterization of Permeability to Hydrocarbon Gas and Liquid for Unconventional Reservoirs: A Challenge to Conventional Thinking. Society of Petroleum Engineers.
Curtis, M.E., Cardott, B.J., Sondergeld, C.H., Rai, C.S., 2012. Development of organic porosity in the Woodford Shale with increasing thermal maturity. Int. J. Coal Geol. 103, 26–31.
Cuss, R.J., Harrington, J.F., 2014. Experimental observations of the flow of water and gas along fractures in Opalinus Clay. In: Fourth EAGE Shale Workshop, Porto, Portugal.
Cuss, R.J., Milodowski, A., Harrington, J.F., 2011. Fracture transmissivity as a function of normal and shear stress: first results in Opalinus Clay. Phys. Chem. Earth Parts A/B/C 36, 1960–1971.
Cuss, R., Harrington, J., Giot, R., Auvray, C., 2014. Experimental observations of mechanical dilation at the onset of gas flow in Callovo-Oxfordian claystone. Geol. Soc. Lond. Spec. Publ. 400.
Cussler, E.L., 2009. Diffusion: Mass transfer in fluid systems, In: Cambridge Series in Chemical Engineering.
Dehghanpour, H., Zubair, H.A., Chhabra, A., Ullah, A., 2012. Liquid intake of organic shales. Energy Fuels 26, 5750–5758.
Dewhurst, D.N., Aplin, A.C., Sarda, J.-P., Yang, Y., 1998. Compaction-driven evolution of porosity and permeability in natural mudstones: an experimental study. J. Geophys. Res. Solid Earth 103, 651–661.
Dewhurst, D.N., Aplin, A.C., Sarda, J.-P., 1999a. Influence of clay fraction on pore-scale properties and hydraulic conductivity of experimentally compacted mudstones. J. Geophys. Res. Solid Earth 104, 29261–29274.
Dewhurst, D.N., Yang, Y., Aplin, A.C., 1999b. Permeability and fluid flow in natural mudstones. Geol. Soc. Lond. Spec. Publ. 158, 23–43.
Dicker, A.I., Smits, R.M., 1988. A Practical Approach for Determining Permeability from Laboratory Pressure-Pulse Decay Measurements. Society of Petroleum Engineers.
Dewhurst, D.N., Jones, R.M., Raven, M.D., 2002. Microstructural and petrophysical charaterization of Muderong Shale: application to top seal risking. Petrol. Geosci. 8 (4), 371–383.
Economides, M.J., Oligney, R.E., Lewis, P.E., 2012. U.S. natural gas in 2011 and beyond. J. Nat. Gas Sci. Eng. 8, 2–8.
Egermann, P., Lombard, J.-M., Bretonnier, P., 2006. A fast and accurate method to measure threshold capillary pressure of caprocks under representative conditions, In: SCA International Symposium, p. 14.
eia, 2013. Power Plant Emissions of Sulfur Dioxide and Nitrogen Oxides Continue to Decline in 2012, Today in Energy. U.S. Energy Information Administration.
Ekeroth, E., Roth, O., Jonsson, M., 2006. The relative impact of radiolysis products in radiation induced oxidative dissolution of UO_2. J. Nucl. Mater. 355, 38–46.
Ellsworth, W.L., 2013. Injection-induced earthquakes. Science, 341.
Fathi, E., Tinni, A., Akkutlu, I.Y., 2012. Correction to Klinkenberg slip theory for gas flow in nano-capillaries. Int. J. Coal Geol. 103, 51–59.
Faulkner, D.R., Rutter, E.H., 2000. Comparisons of water and argon permeability in natural clay-bearing fault gouge under high pressure at 20 °C. J. Geophys. Res. Solid Earth 105, 16415–16426.
Faulkner, D.R., Sciences, U.o.M.D.o.E., 1997. The Role of Clay-bearing Fault Gouges in Controlling Fluid Pressures in Fault Zones: Implications for Fault Mechanics. University of Manchester.
Fetkovich, M.J., 1980. Decline curve analysis using type curves. JPT 32, 1065–1077.
Fisher, Q.J., Harris, S.D., McAllister, E., Knipe, R.J., Bolton, A.J., 2001. Hydrocarbon flow across faults by capillary leakage revisited. Mar. Pet. Geol. 18, 251–257.
Freeman, D.L., Bush, D.C., 1983. Low-Permeability Laboratory Measurements by Nonsteady-State and Conventional Methods, SPE-10075-PA.
Freeman, C.M., Moridis, G.J., Blasingame, T.A., 2012. A numerical study of microscale flow behavior in tight gas and shale gas reservoir systems. Transp Porous Med 90, 253–268.
Galle, C., Tanai, K., 1998. Evaluation of gas transport properties of backfill materials for waste disposal: H2 migration experiments in compacted Fo-Ca Clay. Clays Clay Miner. 46, 498–508.
Gangi, A.F., 1978. Variation of whole and fractured porous rock permeability with confining pressure. Int. J. Rock Mech. Min. Sci. Geomech. Abstr. 15, 249–257.
Garagash, D., Detournay, E., 1997. An analysis of the influence of the pressurization rate on the borehole breakdown pressure. Int. J. Solids Struct. 34, 3099–3118.
Garg, S.K., Nur, A., 1973. Effective stress laws for fluid-saturated porous rocks. J. Geophys. Res. 78, 5911–5921.
Gasparik, M., Ghanizadeh, A., Bertier, P., Gensterblum, Y., Krooss, B.M., Littke, R., 2013. Geological controls on the methane storage capacity in organic-rich shales. Int. J. Coal Geol.
Gasparik, M., Gensterblum, Y., Ghanizadeh, A., Weniger, P., Krooss, B.M., 2014. High-pressure high-temperature methane sorption measurements on carbonaceous shales using manometric method: experimental and data evaluation considerations for improved accuracy. SPE J.
Gensterblum, Y., Zoback, M., 2014. Carbon dioxide a fracturing fluid in shale gas reservoirs. SRB report 2014 (submitted for publication).
Gensterblum, Y., Cumming, D., Busch, A., Krooss, B.M., 2011a. Experimental investigation of CBM-related transport processes on Surat Basin coal, In: Massarotto, P. (Ed.), The 3rd Asia Pacific Coalbed Methane Symposium (3rd APCBM) Brisbane, Australia.
Gensterblum, Y., Krooss, B.M., Massarotto, P., 2011b. Results of mechanical, sorption and transport experiments on a German high volatile bituminous coal. In: Massarotto, P. (Ed.), The 3rd Asia Pacific Coalbed Methane Symposium (3rd APCBM), Brisbane, Australia.
Gensterblum, Y., M., S., Krooss, B., D., C. and Busch, A., 2011c. Experimental investigation of CBM-related transport processes on Surat Basin coal. In: P., M. (Ed.), The 3rd Asia Pacific Coalbed Methane Symposium, Brisbane, Australia.
Gensterblum, Y., Sartorius, M., Busch, A.D.C., Krooss, B.M., 2012. CO2-ECBM related coupled physical and mechanical transport processes. In: Michael, K. (Ed.), EGU General Assembly 2012. EGU, Vienna.
Gensterblum, Y., Ghanizadeh, A., Krooss, B.M., 2014. Gas permeability measurements on Australian subbituminous coals: fluid dynamic and poroelastic aspects. J. Nat. Gas Sci. Eng. 19, 202–214.
Ghanizadeh, A., Gasparik, M., Amann-Hildenbrand, A., Gensterblum, Y., Krooss, B.M., 2013. Lithological controls on matrix permeability of organic-rich shales: an experimental study. Energy Procedia 40, 127–136.
Ghanizadeh, A., Gasparik, M., Amann-Hildenbrand, A., Gensterblum, Y., Krooss, B.M., 2014a. Experimental study of fluid transport processes in the matrix system of the European organic-rich shales: I. Scandinavian alum shale. Mar. Pet. Geol. 51, 79–99.
Ghanizadeh, A., Amann-Hildenbrand, A., Gasparik, M., Gensterblum, Y., Krooss, B.M., Littke, R., 2014b. Experimental study of fluid transport processes in the matrix system of the European organic-rich shales: II. Posidonia shale (Lower Toarcian, northern Germany). Int. J. Coal Geol. 123, 20–33.

Ghanizadeh, A., Bhowmik, S., Haeri-Ardakani, O., Sanei, H., Clarkson, C.R., 2015a. A comparison of shale permeability coefficients derived using multiple non-steady-state measurement techniques: Examples from the Duvernay Formation, Alberta (Canada). Fuel 140, 371–387.
Ghanizadeh, A., Clarkson, C.R., Aquino, S., Ardakani, O.H., Sanei, H., 2015b. Petrophysical and geomechanical characteristics of Canadian tight oil and liquid-rich gas reservoirs: I Pore network and permeability characterization. Fuel 153, 664–681.
Goggin, D.J., 1993. Probe permeametry: is it worth the effort? Mar. Pet. Geol. 10, 299–308.
Gupta, D.V.S., 2011. Unconventional fracturing fluids: what, where and why. In: Technical Workshop for Hydraulic Fracturing Study. SPE, Arlington, VA.
Gutierrez, M., Øino, L.E., Nygård, R., 2000. Stress-dependent permeability of a de-mineralised fracture in shale. Mar. Pet. Geol. 17, 895–907.
Haimson, B., Fairhurst, C., 1967. Initiation and Extension of Hydraulic Fractures in Rocks, SPE-1710-PA.
Halpern, A.M., Glendening, E.D., 1996. Estimating molecular collision diameters using computational methods. J. Mol. Struct. Thoechem 365, 9–12.
Halvorsen, C., Hurst, A., 1990. Principles, practice, and applications of laboratory minipermeametry. In: Worthington, P.F. (Ed.), Advances in Core Evaluation: Accuracy and Precision in Reserves Estimation Gordon and Breach, London, pp. 521–549.
Han, F., Busch, A., van Wageningen, N., Yang, J., Liu, Z., Krooss, B.M., 2010. Experimental study of gas and water transport processes in the inter-cleat (matrix) system of coal: anthracite from Qinshui Basin, China. Int. J. Coal Geol. 81, 128–138.
Handwerger, D.A., Keller, J., Vaughn, K., 2011. Improved Petrophysical Core Measurements on Tight Shale Reservoirs Using Retort and Crushed Samples. Society of Petroleum Engineers.
Harrington, J.F., Horseman, S.T., 1999. Gas transport properties of clays and mudrocks. Geol. Soc. Lond. Spec. Publ. 158, 107–124.
Harrington, J.F., Noy, D.J., Horseman, S.T., Birchall, D.J., Chadwick, R.A., 2009. Laboratory study of gas and water flow in the Nordland Shale, Sleipner, North Sea. In: Grobe, J.C.P., Dodge, R. L. (Ed.), Carbon Dioxide Sequestration in Geological Media—State of the Science. AAPG Studies in Geology, pp. 521–543.
Harrington, J.F., Milodowski, A.E., Graham, C.C., Rushton, J.C., Cuss, R.J., 2012. Evidence for gas-induced pathways in clay using a nanoparticle injection technique. Mineral. Mag. 76, 3327–3336.
Haskett, S.E., Narahara, G.M., Holditch, S.A., 1988. A Method for Simultaneous Determination of Permeability and Porosity in Low-Permeability Cores, SPE-15379-PA.
Heller, R., Vermylen, J., Zoback, M., 2014. Experimental investigation of matrix permeability of gas shales. AAPG Bull. 98, 975–995.
Hildenbrand, A., Schlömer, S., Krooss, B.M., 2002. Gas breakthrough experiments on fine-grained sedimentary rocks. Geofluids 2, 3–23.
Hildenbrand, A., Schlömer, S., Krooss, B.M., Littke, R., 2004. Gas breakthrough experiments on pelitic rocks: comparative study with N_2, CO_2 and CH_4. Geofluids 4, 61–80.
Hirschfelder, J.O., Curtiss, C.F., Bird, R.B., 1954. Molecular Theory of Gases and Liquids. Wiley, New York.
Holt, R.M., Bhuiyan, M.H., Kolstø, M.I., Bakk, A., Stenebraten, J.F., Fjær, E., 2011. Stress-induced versus lithological anisotropy in compacted claystones and soft shales. Lead. Edge 30, 312–317.
Horseman, S.T., Harrington, J.F., Sellin, P., 1997. Gas migration in Mx80 buffer bentonite. In: Materials Research Society Symposium – Proceedings, pp. [d] 1003–1010.
Horseman, S.T., Harrington, J.F., Sellin, P., 1999. Gas migration in clay barriers. Eng. Geol. 54, 139–149.
Houben, M.E., Desbois, G., Urai, J.L., 2013. Pore morphology and distribution in the Shaly facies of Opalinus Clay (Mont Terri, Switzerland): insights from representative 2D BIB-SEM investigations on mm to nm scale. Appl. Clay Sci. 71, 82–97.
Howarth, R.W., Ingraffea, A., Engelder, T., 2011. Natural gas: should fracking stop? Nature 477, 271–275.
Hsieh, P.A., Tracy, J.V., Neuzil, C.E., Bredehoeft, J.D., Silliman, S.E., 1981. A transient laboratory method for determining the hydraulic properties of 'tight' rocks—I. Theory. Int. J. Rock Mech. Min. Sci. Geomech. Abstr. 18, 245–252.
Hubbert, M.K., Willis, D.G., 1957. Mechanics of Hydraulic Fracturing. Society of Petroleum Engineers.
Ibanez, W.D., Kronenberg, A.K., 1993. Experimental deformation of shale: mechanical properties and microstructural indicators of mechanisms. Int. J. Rock Mech. Min. Sci. Geomech. Abstr. 30, 723–734.
Ibrahim, M.A., Tek, M.R., Katz, D.L., 1970. Threshold pressure in gas storage. In: American, P.r.c. (Ed.), Gas Association at the University of Michigan, Michigan.
Ingram, G.M., Urai, J.L., Naylor, M.A., 1997. Sealing processes and top seal assessment. In: Møller-Pedersen, P., Koestler, A.G. (Eds.), Norwegian Petroleum Society Special Publications. Elsevier, pp. 165–174.
Jamialahmadi, M., Javadpour, F.G., 2000. Relationship of permeability, porosity and depth using an artificial neural network. J. Petrol. Sci. Eng. 26, 235–239.
Jizba, D.L., 1991. Mechanical and Acoustical Properties of Sandstones and Shales. Department of Geophysics, Stanford University.
Jones, S.C., 1994. A New, Fast, Accurate Pressure-Decay Probe Permeameter, SPE-24757-PA.
Katsube, T.J., 2000. Shale Permeability and Pore-Structure Evolution Characteristics. Geological Survey of Canada, Ottawa, ON, Canada.
Katsube, T.J., Williamson, M.A., 1994. Effects of diagenesis on shale nano-pore structure and implications for sealing capacity. Clay Miner. 29, 451–461.
Katsube, T.J., Mudford, B.S., Best, M.E., 1991. Petrophysical characteristics of shales from the Scotian shelf. Geophysics 56, 1681–1689.
Katsube, T.J., Williamson, M.A., Best, M.E., 1992. Shale pore structure evolution and its effect on permeability, SCA Conference, paper No. 9214.
Kerr, R.A., 2010. Natural gas from shale bursts onto the scene. Science 328, 1624–1626.
Kim, J., Lee, J., 2012. Novel Apparatus to Measure the Low-Permeability and Porosity in Tight and Shale Gas Reservoir. International Society of Offshore and Polar Engineers, ISOPE-I-13-079.
Kim, K., Lee, Y., Hwang, S., Seo, J., Sung, W., 2011. Improved capillary pressure model considering dual-pore geometry system in carbonate reservoirs. J. Petrol. Sci. Eng. 78, 601–608.
King Hubbert, M., Rubey, W.W., 1959. Role of fluid pressure in mechanics of overthrust faulting: I. Mechanics of fluid-filled porous solids and its application to overthrust faulting. Geol. Soc. Am. Bull. 70, 115–166.
Kinnaman, T.C., 2011. The economic impact of shale gas extraction: a review of existing studies. Ecol. Econ. 70, 1243–1249.
Klaver, J., Desbois, G., Urai, J.L., Littke, R., 2012. BIB-SEM study of the pore space morphology in early mature Posidonia Shale from the Hils area, Germany. Int. J. Coal Geol. 103, 12–25.
Klaver, J., Desbois, G., Littke, R., Urai, J.L., 2015. BIB-SEM characterization of pore space morphology and distribution in postmature to overmature samples from the Haynesville and Bossier Shales. Mar. Pet. Geol. 59, 451–466.
Klinkenberg, L.J., 1941. The permeability of porous media to liquids and gases. Prod. Pract., 200–213
Kranz, R.L., Saltzman, J.S., Blacic, J.D., 1990. Hydraulic diffusivity measurements on laboratory rock samples using an oscillating pore pressure method. Int. J. Rock Mech. Min. Sci. Geomech. Abstr. 27, 345–352.
Kranzz, R.L., Frankel, A.D., Engelder, T., Scholz, C.H., 1979. The permeability of whole and jointed Barre Granite. Int. J. Rock Mech. Min. Sci. Geomech. Abstr. 16, 225–234.
Krooss, B.M., 1986. Diffusion of C1 to C5 hydrocarbons in water-saturated sedimentary rocks. Erdoel Kohle Erdgas Petrochem. 39, 399–402.
Krooss, B.M., 1987. Experimental investigation of the diffusion of low-molecular weight hydrocarbons from source rocks. In: Migration of Hydrocarbons in Sedimentary Basins, 2nd IFP Exploration Research Conference, Carcans, France, June 15–19, 1987. Technip, Paris.
Krooss, B.M., 1988. Experimental investigation of the molecular migration of C1–C6 hydrocarbons: kinetics of hydrocarbon release from source rocks. Org. Geochem. 13, 513–523.
Krooss, B.M., 1992. Diffusion losses of hydrocarbons through cap rock. Experimental studies and theoretical considerations. Erdoel Kohle Erdgas Petrochem. 45, 387–396.
Krooss, B.M., Leythaeuser, D., 1988. Experimental measurements of the diffusion parameters of light hydrocarbons in water-saturated sedimentary rocks: II. Results and geochemical significance. Org. Geochem. 12, 91–108.
Krooss, B.M., Leythaeuser, D., 1996, Molecular diffusion of light hydrocarbons in sedimentary rocks and its role in migration and dissipation of natural gas. In: Hydrocarbon Migration and its Near-Surface Expression, AAPG Hedberg research conference.
Krooss, B.M., Leythaeuser, D., 1997. Diffusion of methane and ethane through the reservoir cap rock: implications for the timing and duration of catagenesis: discussion. AAPG Bull. 81, 155–161.
Krooss, B., Schaefer, R.G., 1987. Experimental measurements of the diffusion parameters of light hydrocarbons in water-saturated sedimentary rocks: I. A new experimental procedure. Org. Geochem. 11, 193–199.
Krooss, B., Leythaeuser, D., Schaefer, R.G., 1986. Experimental determination of diffusion parameters for light hydrocarbons in water-saturated rocks: some selected results. In: Leythaeuser, D., Rullkötter, J. (Eds.), Advances in Organic Geochemistry 1985. Pergamon Press, London, pp. 291–297.
Krooss, B.M., Leythaeuser, D., Schaefer, R.G., 1988. Light hydrocarbon diffusion in a caprock. Chem. Geol. 71, 65–76.
Krooss, B.M., Brothers, L., Engel, M.H., 1991. Geochromatography in petroleum migration: a review. Geol. Soc. Lond. Spec. Publ. 59, 149–163.
Krooss, B.M., Leythaeuser, D., Schaefer, R.G., 1992. The quantification of diffusive hydrocarbon losses through cap rocks of natural gas reservoirs-a reevaluation: reply. AAPG Bull. 76, 1842–1846.
Kwon, O., Kronenberg, A.K., Gangi, A.F., Johnson, B., 2001. Permeability of Wilcox shale and its effective pressure law. J. Geophys. Res. Solid Earth 106, 19339–19353.
Kwon, O., Kronenberg, A.K., Gangi, A.F., Johnson, B., Herbert, B.E., 2004. Permeability of illite-bearing shale: 1. Anisotropy and effects of clay content and loading. J. Geophys. Res. 109, B10205-B10205.10219.
Lash, G., 2013. Name the gas industry birthplace: Fredonia, N.Y.?, In: KEN MILAM, E. C. (Ed.). Aapg.org. Retrieved.
Li, M., Bernabé, Y., Xiao, W.I., Chen, Z.Y., Liu, Z.Q., 2009. Effective pressure law for permeability of E-bei sandstones. J. Geophys. Res. Solid Earth 114, B07205.
Li, M., Xiao, W.L., Bernabé, Y., Zhao, J.Z., 2014. Nonlinear effective pressure law for permeability. J. Geophys. Res. Solid Earth 119, 2013JB010485.
Luffel, D.L., Hopkins, C.W., Schettler Jr., P.D., 1993. Matrix Permeability Measurement of Gas Productive Shales. Society of Petroleum Engineers.
Mallon, A.J., Swarbrick, R.E., 2008. How should permeability be measured in fine grained lithologies? Evidence from the chalk. Geofluids 8, 35–45.

Marschall, P., Horseman, S., Gimmi, T., 2005. Characterisation of gas transport properties of the Opalinus Clay, a potential host rock formation for radioactive waste disposal. Oil Gas Sci. Technol. – Rev. IFP 60, 121–139.
Mattar, L., 2008. Production Analysis and Forecasting of Shale Gas Reservoirs: Case History-Based Approach. Society of Petroleum Engineers.
Mazza, R.L., 2001, Liquid-free CO_2/sand stimulation: an overlooked technology – production update, SPE. SPE, p. SPE 72383.
Mbia, E.N., Frykman, P., Nielsen, C.M., Fabricius, I.L., Pickup, G.E., Bernstone, C., 2014. Caprock compressibility and permeability and the consequences for pressure development in CO_2 storage sites. Int. J. Greenhouse Gas Control 22, 139–153.
McElroy, M., Lu, X., 2013. Fracking's future – natural gas, the economy, and America's energy prospects. Havard Mag., 24–27
McKernan, R.E., Rutter, E.H., Mecklenburgh, J., Taylor, K.G., Covey-Crump, S.J., 2014a, Influence of effective pressure on mudstone matrix permeability: implications for shale gas production. In: Society of Petroleum Engineers – European Unconventional Resources Conference and Exhibition 2014: Unlocking European Potential, pp. 748–760.
McPhee, C.A., Arthur, K.G., 1991. Klinkenberg permeability measurements: problems and practical solutions. Advances in Core Evaluation II: reservoir Appraisal: Reviewed proceedings, pp. 371–392.
McKernan, R.E., Rutter, E.H., Mecklenburgh, J., Taylor, K.G., Covey-Crump, S.J., 2014b. Influence of Effective Pressure on Mudstone Matrix Permeability: Implications for Shale Gas Production. Society of Petroleum Engineers.
Metwally, Y.M., Sondergeld, C.H., 2011. Measuring low permeabilities of gas-sands and shales using a pressure transmission technique. Int. J. Rock Mech. Min. Sci. 48, 1135–1144.
Meyn, 1999, Die Bedeutung des sperrdrucks (threshold pressure) für den fuidtransport in neidrigstpermeablen Gesteinen: Experimentelle und theoretishe Aspekte, DGMK Spring Conference, 255–264.
Mishra, A.K., Masami, O., Li, L., Higahsi, T., 2005. Effect of salt concentrations on the permeability and compressibility of soil-bentonite mixtures. J. Fac. Agric. Kyushu Univ. 50, 837–849.
Mokhtari, M., Alqahtani, A.A., Tutuncu, A.N., Yin, X., 2013. Stress-Dependent Permeability Anisotropy and Wettability of Shale Resources. Society of Petroleum Engineers.
Morrow, C.A., Shi, L.Q., Byerlee, J.D., 1984. Permeability of fault gouge under confining pressure and shear stress. J. Geophys. Res. Solid Earth 89, 3193–3200.
Nandi, S.P., Walker Jr., P.L., 1975. Activated diffusion of methane from coals at elevated temperatures. Fuel 54, 81–86.
Neuzil, C.E., 1994. How permeable are clays and shales? Water Resour. Res. 30, 145–150.
Niu, C., Hao, Y.-Z., Li, D., Lu, D., 2014. Second-Order Gas-Permeability Correlation of Shale During Slip Flow, SPE-168226-PA.
Nur, A., Byerlee, J.D., 1971. An exact effective stress law for elastic deformation of rock with fluids. J. Geophys. Res. 76, 6414–6419.
Nuttall, B.C., 2003, Oil and Gas History of Kentucky, 1900 to present. Kentucky Geological Survey, University of Kentucky, <www.uky.edu>.
Odusina, E.O., Sondergeld, C.H., Rai, C.S., 2011. NMR Study of Shale Wettability. Society of Petroleum Engineers.
Ortiz, L., Volckaert, G., Mallants, D., 2002. Gas generation and migration in Boom Clay, a potential host rock formation for nuclear waste storage. Eng. Geol. 64, 287–296.
Ozkan, E., Brown, M.L., Raghavan, R., Kazemi, H., 2011. Comparison of Fractured-Horizontal-Well Performance in Tight Sand and Shale Reservoirs, SPE-121290-PA.
Pan, Z., Connell, L.D., Camilleri, M., 2010. Laboratory characterisation of coal reservoir permeability for primary and enhanced coalbed methane recovery. Int. J. Coal Geol. 82, 252–261.
Parmar, J., Dehghanpour, H., Kuru, E., 2012. Unstable Displacement: A Missing Factor in Fracturing Fluid Recovery. Society of Petroleum Engineers.
Paterson, M.S., 1983. The equivalent channel model for permeability and resistivity in fluid-saturated rock—a re-appraisal. Mech. Mater. 2, 345–352.
Pathi, V., 2008. Factors Affecting the Permeability of Gas Shales. University of British Columbia, Vancouver, British Columbia, Canada.
Pazos, F.A., Bhaya, A., Compan, A.L.M., 2009. Calculation of Klinkenberg permeability, slip factor and turbulence factor of core plugs via nonlinear regression. J. Petrol. Sci. Eng. 67, 159–167.
Petunin, V.V., Yin, X., Tutuncu, A.N., 2011. Porosity and Permeability Changes in Sandstones and Carbonates Under Stress and Their Correlation to Rock Texture. Society of Petroleum Engineers.
Pillalamarry, M., Harpalani, S., Liu, S., 2011. Gas diffusion behavior of coal and its impact on production from coalbed methane reservoirs. Int. J. Coal Geol. 86, 342–348.
Rice, P.A., Fontugne, D.J., Latini, R.G., Barduhn, A.J., 1970. Anisotropic permeability in porous media. Ind. Eng. Chem. 62, 23–31.
Robin, P.-Y.F., 1973. Note on effective pressure. J. Geophys. Res. 78, 2434–2437.
Rushing, J.A., Newsham, K.E., Lasswell, P.M., Cox, J.C., Blasingame, T.A., 2004. Klinkenberg-corrected permeability measurements in tight gas sands: steady-state versus unsteady-state techniques. In: SPE Annual Technical Conference and Exhibition, Houston, Texas, p. 11
Rutqvist, J., Stephansson, O., 2003. The role of hydromechanical coupling in fractured rock engineering. Hydrogeol. J. 11, 7–40.
Sakhaee-Pour, A., Bryant, S.C.S.P.E., 2012. Gas Permeability of Shale, http://dx.doi.org/10.2118/146977-pa.
Sathar, S., Reeves, H.J., Cuss, R.J., Harrington, J.F., 2012. The role of stress history on the flow of fluids through fractures. Mineral. Mag. 76, 3165–3177.
Schettler, P.D., Jr., Parmely, C.R., 1989. Gas Composition Shifts in Devonian Shales, SPE-17033-PA.
Schlömer, S., Krooss, B.M., 1997. Experimental characterisation of the hydrocarbon sealing efficiency of cap rocks. Mar. Pet. Geol. 14, 565–580.
Schowalter, T.T., 1979. Mechanics of secondary hydrocarbon migration and entrapment. AAPG Bull. 63, 723–760.
Shanley, K.W., Cluff, R.M., Robinson, J.W., 2004. Factors controlling prolific gas production from low-permeability sandstone reservoirs: implications for resource assessment, prospect development, and risk analysis. AAPG Bull. 88, 1083–1121.
Sibson, R.H., 1995. Selective fault reactivation during basin inversion: potential for fluid redistribution through fault-valve action. Basin Invers., 3–19
Singh, H., Javadpour, F., Ettehadtavakkol, A., Darabi, H., 2014. Nonempirical Apparent Permeability of Shale, SPE-170243-PA.
Sinha, S., Braun, E.M., Passey, Q.R., Leonardi, S.A., Wood III, A.C., Zirkle, T., Boros, J. A., Kudva, R.A., 2012. Advances in Measurement Standards and Flow Properties Measurements for Tight Rocks such as Shales. Society of Petroleum Engineers.
Sinha, S., Braun, E.M., Determan, M.D., Passey, Q.R., Leonardi, S.A., Boros, J.A., Wood Iii, A.C., Zirkle, T., Kudva, R.A., 2013. Steady-State Permeability Measurements on Intact Shale Samples at Reservoir Conditions - Effect of Stress, Temperature, Pressure, and Type of Gas. Society of Petroleum Engineers.
Soeder, D.J., 1988. Porosity and Permeability of Eastern Devonian Gas Shale, SPE-15213-PA.
Solano, N.A., Clarkson, C.R., Krause, F., 2012. Quantification of cm-Scale Heterogeneities in Tight-Oil Intervals of the Cardium Formation at Pembina, WCSB, Alberta, Canada. Society of Petroleum Engineers.
Sone, H., Zoback, M.D., 2014. Time-dependent deformation of shale gas reservoir rocks and its long-term effect on the in situ state of stress. Int. J. Rock Mech. Min. Sci. 69, 120–132.
Song, B., Ehlig-Economides, C.A., 2011. Rate-Normalized Pressure Analysis for Determination of Shale Gas Well Performance. Society of Petroleum Engineers.
Song, I., Suh, M., Won, K.S., Haimson, B., 2001. A laboratory study of hydraulic fracturing breakdown pressure in table-rock sandstone. Geosci. J. 5, 263–271.
Spinelli, G.A., Giambalvo, E.R., Fisher, A.T., 2004. Sediment permeability, distribution, and influence on fluxes in oceanic basement. In: Davis, E.E., Elderfield, H. (Eds.), Hydrogeology of the Oceanic Lithosphere. Cambridge University Press.
Suarez-Rivera, R., Chertov, M., Willberg, D.M., Green, S.J., Keller, J., 2012. Understanding Permeability Measurements in Tight Shales Promotes Enhanced Determination of Reservoir Quality. Society of Petroleum Engineers.
Sulucarnain, I.D., Sondergeld, C.H., Rai, C.S., 2012. An NMR Study of Shale Wettability and Effective Surface Relaxivity. Society of Petroleum Engineers.
Sutherland, W.J., Halvorsen, C., Hurst, A., McPhee, C.A., Robertson, G., Whattler, P.R., Worthington, P.F., 1993. Recommended practice for probe permeametry. Mar. Pet. Geol. 10, 309–317.
Tanikawa, W., Shimamoto, T., 2009a. Comparison of Klinkenberg-corrected gas permeability and water permeability in sedimentary rocks. Int. J. Rock Mech. Min. Sci. 46, 229–238.
Tanikawa, W., Shimamoto, T., 2009b. Correction to "comparison of Klinkenberg-corrected gas permeability and water permeability in sedimentary rocks". Int. J. Rock Mech. Min. Sci. 46, 1394–1395.
Terzaghi, K., 1923. Die Berechnung der Durchlässigkeitsziffer des Tones aus dem Verlauf der hydrodynamischen Spannungserscheinungen. Sitz. Akad. Wissen. Wien Math. Naturwiss. Kl., Wien, pp. 105–124.
Thimons, E.D., Kissell, F.N., 1973. Diffusion of methane through coal. Fuel 52, 274–280.
Tiab, D., Donaldson, E.C., 2004a. Chapter 3 – porosity and permeability. In: Tiab, D., Donaldson, E.C. (Eds.), Petrophysics, second ed. Gulf Professional Publishing, Burlington, pp. 87–202.
Tiab, D., Donaldson, E.C., 2004b. Chapter 5 – capillary pressure. In: Tiab, D., Donaldson, E.C. (Eds.), Petrophysics, second ed. Gulf Professional Publishing, Burlington, pp. 313–359.
Tiab, D., Donaldson, E.C., 2004c. Chapter 6 – wettability. In: Tiab, D., Donaldson, E.C. (Eds.), Petrophysics, second ed. Gulf Professional Publishing, Burlington, pp. 360–414.
Timms, N.E., Healy, D., Reyes-Montes, J.M., Collins, D.S., Prior, D.J., Young, R.P., 2010. Effects of crystallographic anisotropy on fracture development and acoustic emission in quartz. J. Geophys. Res. Solid Earth 115, B07202.
Tinni, A., Fathi, E., Agarwal, R., Sondergeld, C., Akkutlu, Y., Rai, C., 2012. Shale permeability measurements on plugs and crushed samples. In: Society of Petroleum Engineers – SPE Canadian Unconventional Resources Conference 2012, CURC 2012, pp. 342–355.
Townend, J., Zoback, M.D., 2000. How faulting keeps the crust strong. Geology 28, 399–402.
Valko, P.P., Lee, W.J., 2010. A Better Way to Forecast Production from Unconventional Gas Wells. Society of Petroleum Engineers.
Vermylen, J.P., 2011. Geomechanical Studies of the Barnett Shale, Texas, USA. Geophysics, Stanford University, Stanford.
Vernik, L., 1993. Microcrack-induced versus intrinsic elastic anisotropy in mature HC-source shales. Geophysics 58, 1703–1706.
Vernik, L., 1994. Hydrocarbon-generation-induced microcracking of source rocks. Geophysics 59, 555–563.
Wang, K., Li, G., Shen, Z., 2012. A feasibility analysis on shale gas exploitation with supercritical carbon dioxide. Energ. Sources A: Recov. Utilization, Environ. Effects 34 (15), 1426–1435.

Walsh, J.B., 1981. Effect of pore pressure and confining pressure on fracture permeability. Int. J. Rock Mech. Min. Sci. Geomech. Abstr. 18, 429–435.
Walsh, F.R., Zoback, M.D., 2015. Oklahoma's recent earthquakes and saltwater disposal. Sci. Adv. 1.
Wang, F.P., Reed, R.M., 2009. Pore Networks and Fluid Flow in Gas Shales. Society of Petroleum Engineers.
Warpinski, N.R., Teufel, L.W., 1992. Determination of the Effective-Stress Law for Permeability and Deformation in Low-Permeability Rocks, SPE-20572-PA.
Warpinski, N.R., Teufel, L.W., 1993. Laboratory measurements of the effective-stress law for carbonate rocks under deformation. Int. J. Rock Mech. Min. Sci. Geomech. Abstr. 30, 1169–1172.
Wiseall, J.B., Cuss, R.J., Harrington, J.F., Graham, C.C., 2014. The visualisation of flow-paths in experimental studies of clay-rich rocks. In: IGD-TP Geodisposal 2014, Manchester, UK.
Wollenweber, J., Alles, S., Busch, A., Krooss, B.M., Stanjek, H., Littke, R., 2010. Experimental investigation of the CO_2 sealing efficiency of caprocks. Int. J. Greenhouse Gas Control 4, 231–241.
Yang, Y., Aplin, A.C., 1998. Influence of lithology and compaction on the pore size distribution and modelled permeability of some mudstones from the Norwegian margin. Mar. Pet. Geol. 15, 163–175.
Yang, Y., Aplin, A.C., 2007. Permeability and petrophysical properties of 30 natural mudstones. J. Geophys. Res. 112.
Yang, Y., Aplin, A.C., 2010. A permeability–porosity relationship for mudstones. Mar. Pet. Geol. 27, 1692–1697.
Yost, A.B., Mazza, R.L., Gehr, J.B., 1993. CO_2/Sand Fracturing in Devonian Shales, SPE, p. SPE 26925.
Zhang, T., Krooss, B.M., 2001. Experimental investigation on the carbon isotope fractionation of methane during gas migration by diffusion through sedimentary rocks at elevated temperature and pressure. Geochim. Cosmochim. Acta 65, 2723–2742.
Zhou, Z., Hoffman, B.T., Bearinger, D., Li, X., 2014. Experimental and Numerical Study on Spontaneous Imbibition of Fracturing Fluids in Shale Gas Formation. Society of Petroleum Engineers.
Zoback, M.D., 2007. Reservoir Geomechanics. Cambridge University Press, Cambridge.
Zoback, M.D., Byerlee, J.D., 1975a. The effect of microcrack dilatancy on the permeability of westerly granite. J. Geophys. Res. 80, 752–755.
Zoback, M.D., Byerlee, J.D., 1975b. Permeability and effective stress. AAPG Bull. 59, 154–158.